Title
Key Challenges in EUV Mask Technology: Actinic Mask Inspection and Mask 3D Effects

Author
Wang, Yow-Gwo

Publication Date
2017

Peer reviewed|Thesis/dissertation

Key Challenges in EUV Mask Technology: Actinic Mask Inspection and Mask 3D Effects

by

Yow-Gwo Wang

A dissertation submitted in partial satisfaction of the

requirements for the degree of

Doctor of Philosophy

in

Engineering-Electrical Engineering and Computer Sciences

in the

Graduate Division

of the

University of California, Berkeley

Committee in charge:

Professor Andrew Neureuther, Chair
Doctor Patrick Naulleau
Associate Professor Laura Waller
Assistant Professor Hayden Taylor

Spring 2017

Key Challenges in EUV Mask Technology: Actinic Mask Inspection and Mask 3D Effects

Abstract

Key Challenges in EUV Mask Technology: Actinic Mask Inspection and Mask 3D Effects

by

Yow-Gwo Wang

Doctor of Philosophy in Engineering-Electrical Engineering and Computer Sciences

University of California, Berkeley

Professor Andrew Neureuther, Chair

This dissertation focuses on issues related to extreme ultraviolet (EUV) lithography mask technology: mask inspection and mask 3D effects on imaging performance. Actinic (at-wavelength) mask inspection (both blank and patterned mask) is of critical concern for EUV lithography. In this dissertation, systematic studies exploring the optimal optical system design to improve the defect detection sensitivity for both actinic mask blank and patterned mask inspection tools using EUV light are presented. For EUV mask blank inspection, a complete discussion is conducted to compare the conventional bright field method and the Zernike phase contrast method on their phase defect detection sensitivity by thin mask simulations and experiments using the SHARP EUV microscope at Lawrence Berkeley National Laboratory (LBNL). The study shows that higher defect detection sensitivity and in-focus inspection capability can be achieved by the Zernike phase contrast method, while the conventional bright field method needs through-focus scanning and results in lower defect detection sensitivity. Experimental results show that a programmed defect as small as 0.35 nm in height is detected at best focus with a signal-to-noise ratio (SNR) ≈ 8 by the Zernike phase contrast method. With the considerations of various noise sources and system design, the thin mask simulation results show that the dark field method has better detection efficiency in inspection mode, while the Zernike phase contrast method is better in review mode (pixel size ≤ 25 nm). Further, the impact of pixel size, EUV source type, and photon collection efficiency for a dark field based actinic blank inspection tool is discussed by thin mask simulation. The simulation results show the complex correlation between each parameter on defect inspection efficiency and also show that 10-watt EUV source power and 100 nm pixel size are needed to capture a phase defect of height 0.5 nm.

For EUV patterned mask inspection, the possibility of using the optimum phase shift in the pupil plane to improve inspection efficiency is discussed using a thin mask model. Then the nature of the EUV mask pattern defect is analyzed by its near field distribution using a thick mask model. The simulation results indicate that, as a result of 3D effects leading to phase artifacts, pattern defects cannot be simply treated as ideal absorber defects. The results can affect the choice of optimal patterned mask inspection tool design. Moreover, a

study of a bright field based EUV actinic pattern inspection tool design using a hybrid (2D + 3D) model is presented, showing that the impact of noise sources and optical design on critical pattern defects detection sensitivity. The study shows that introducing a -50 nm defocus into the inspection system can improve the SNR by 50%.

The impact of EUV sub-resolution assist feature (SRAF) on mitigation of mask 3D effects is discussed by rigorous 3D modeling. The simulation results show that introducing SRAFs in the mask design induces even stronger effective single pole aberration into the imaging system to balance the Bossung curve. Asymmetric SRAFs pattern placement can achieve a 21% improvement of the process window. Moreover, the complex interaction between the main feature and the SRAFs is analyzed by systematic position sensitivity studies. Bossung tilt sensitivity with respect to the relative positions between main feature and SRAFs is shown, which indicates that different location precision requirements are needed for SRAFs during the mask-making process.

To my family and everyone who helped me along the way.

Contents

List of Figures

List of Tables

Acknowledgments

I am deeply grateful to my advisors: Prof. Andrew Neureuther and Dr. Patrick Naulleau, for their endless support and guidance. Andy helped me in the darkest day in my Ph.D. student career and provided support and guidance to bring me back to the track. Patrick is always there to answer my questions not just about the research, but also on life experience and career choice. Their passion towards research and kindness to people inspire me, and I hope I can be just like them in the future.

I would like to thank Prof. Laura Waller and Prof. Hayden Taylor for being my dissertation committees. I also really appreciate the teaching opportunity offered by Laura to let me know how to help people learning new things. Also, I would like to thank EE graduate advisor Shirley Salanio. She is the best staff I have ever met, and her friendliness is one of the best things I have experienced in the EECS department.

I would like to thank my colleges: Rick, Rene, Aamod, Suchit, and Stuart. Without the help by Rick, I would not be able to join this lab and meet all these wonderful people. The conversation with Rene on not just research, but also on personal life colors my time at Berkeley. It is great that our research projects complement each other. It is also good to have Aamod, Suchit, and Stuart in my final days at Berkeley, to share my stress on the dissertation preparation and the challenges ahead for the new chapter of my life.

I am truly thankful to Dr. Ryan Miyakawa, who is not just a mentor providing guidance on research, but also a friend help me accustom to the lab and also the graduate student life in the US. I would like to thank everyone at Center for X-ray Optics for the great environment. In particular, I appreciate the help from Dr. Kenneth Goldberg, Dr. Antoine Wojdyla, and Dr. Markus Benk, for taking the measurement for me, and also Dr. Weilun Chao for zoneplate fabrication.

I would like to thank Dr. Robert Socha for giving me an internship opportunity at ASML. With the guidance from him and Dr. Stephen Hsu, I learn a lot and get some great results for my dissertation. I would also like to thank Dr. Ted Liang from Intel for his support of the experiment and useful suggestions to my research. Also, I appreciate the help from Dr. Tom Pistor for his support on simulation software. This research work is initially supported by IMPACT+ (Integrated Modeling Process and Computation for Technology) then currently by C-DEN (Center for Design-Enable Nanofabrication). Participating companies include Applied Materials, ARM, ASML, Cadence, Carl Zeiss Group, Global Foundries, IBM, Intel, KLA-Tencor, Mentor Graphics, Panoramic Tech, Qualcomm, Samsung, SanDisk, Photronics, Marvell Technology, and Tokyo Electron. This work is performed in part at Lawrence Berkeley National Laboratory which is operated under the auspices of the Director, Office of Science, of the U.S. Department of Energy under Contract No. DE-AC02-05CH11231.

Finally, I would like to thank all my friends I met in Berkeley. Without their companion, I would not have all these memories that complete my time at Berkeley. I would like to thank my family. Unconditional support from my parents gives me a chance to study abroad. My brother's guidance and showing me the path towards a Ph.D. degree are the reason why I am here today. Lastly, Tina. It is great to have you with me for the past few years.

Chapter 1

Introduction

1.1 Background

To extend Moore's law down to signal digit nm scale, semiconductor processing technology especially lithography needs new ways to print the desired circuit pattern, as shown in Fig. 1.1. To improve the optical resolution (R) of a lithography system as shown in Eq. 1.1, we can either increase the numerical aperture (NA) or decrease the wavelength (λ) of the light. For deep ultraviolet (DUV) lithography, immersion lithography techniques have been used to further improve the resolution by utilizing the refractive index of the water at 193 nm wavelength to create an effectively larger NA. Also, multiple patterning techniques have been used to push the resolution beyond even the immersion NA limit. However, for the 7 nm node and beyond, the complexity introduces by multiple patterning for DUV lithography increases the need for new lithography technique to reduce the burden on semiconductor processing [1].

$$R \propto \frac{\lambda}{NA} \tag{1.1}$$

Extreme ultraviolet (EUV) lithography uses 13.5 nm wavelength light, providing a 15x gain in wavelength limited resolution relative to 193 nm. However, to build the eco-system of EUV lithography, the development of stepper, photoresist, and photomask needs to be addressed simultaneously.

For the stepper, the optical elements used at EUV wavelength are completely different from the conventional projection lithography system. Multilayer reflective optics are needed instead of refractive lenses. Moreover, the source power and the tool availability determine the productivity of the tool and thus the economics metrics of EUV lithography. Higher throughput by larger source power and higher tool availability can reduce the cost per wafer for EUV lithography and makes it more attractive compared with the current DUV lithography and multiple patterning approaches. As shown in Fig. 1.2 and Fig. 1.3, the current status of the EUV source shows promising results. 125 Watt (W), which is equivalent to 85 wafers per hour, has been demonstrated in the field, and ASML has achieved 210 W

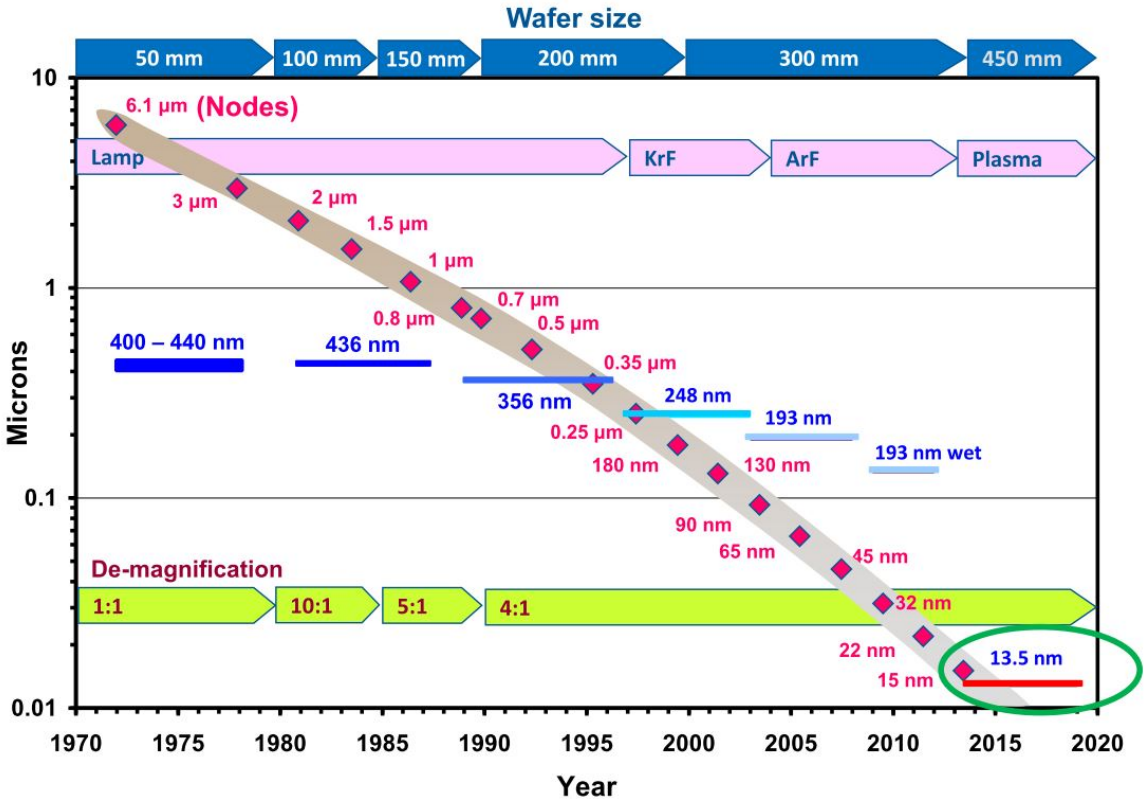

Figure 1.1: The lithography road map [5].

in their labs, which is equivalent to 125 wafers per hour [2]. For tool availability, the average lifetime improves 3x for the Tin (Sn) droplet generator and the collector mirror lifetime is also improved by a factor of 1.5 in 2016. The average availability of the stepper has reached 80% in the field in 2016. These results are close to the target performance (250 W, 90% availability) for EUV lithography to be ready for high-volume manufacturing at 7 or 5 nm node for logic device [3, 4].

For the photoresist, the polymer-based chemically amplified photoresist (CAR) has been studied for years to be used in EUV lithography. However, the RLS (resolution, line edge roughness (LER), sensitivity) tradeoff limits the CAR performance. Pattern collapse is also another challenging issue. On the other hand, the metal-oxide photoresist from Inpria provides a different solution which demonstrates high resolution and low line width roughness (LWR), but at lower sensitivity, as shown in Fig. 1.4 [6]. The metal photoresist utilizes Sn as the primary metal to have high EUV photon sensitivity and etch resistance which leads to a thinner photoresist film to avoid pattern collapse. For 7 nm block mask, the photoresist thickness can be reduced from 40 nm to 18 nm. The best exposure result from Inpria photoresist has achieved a 13 nm half-pitch at 30 mJ/cm^2. The result shows promising performance on photoresist resolution for the upcoming 5 nm logic device.

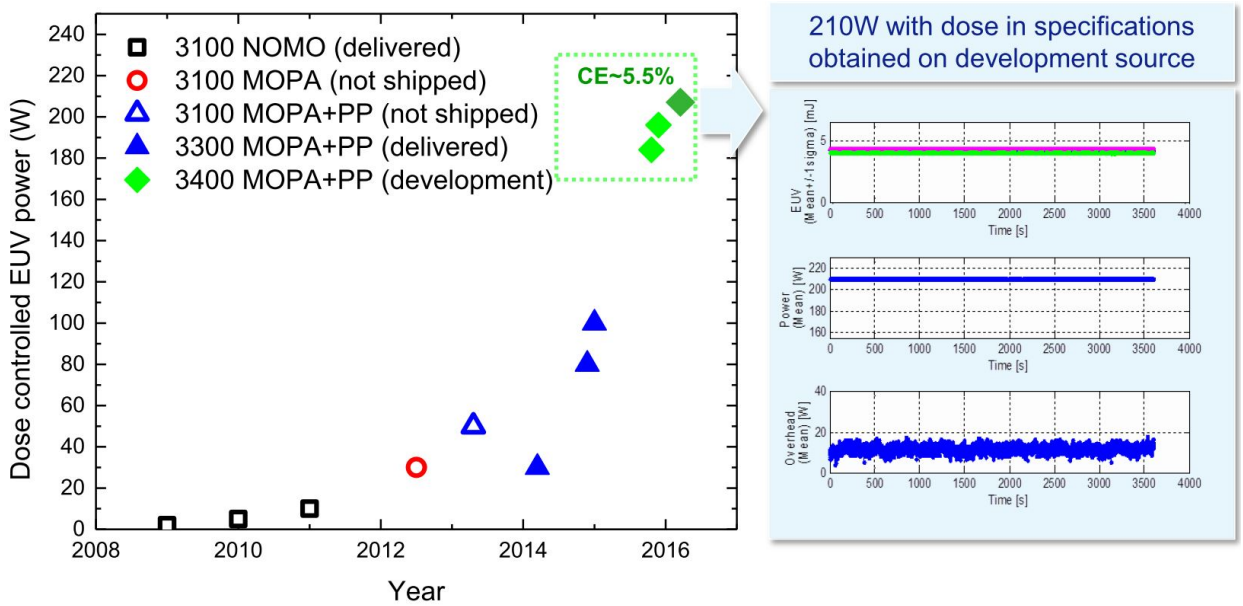

Figure 1.2: EUV source development status [2].

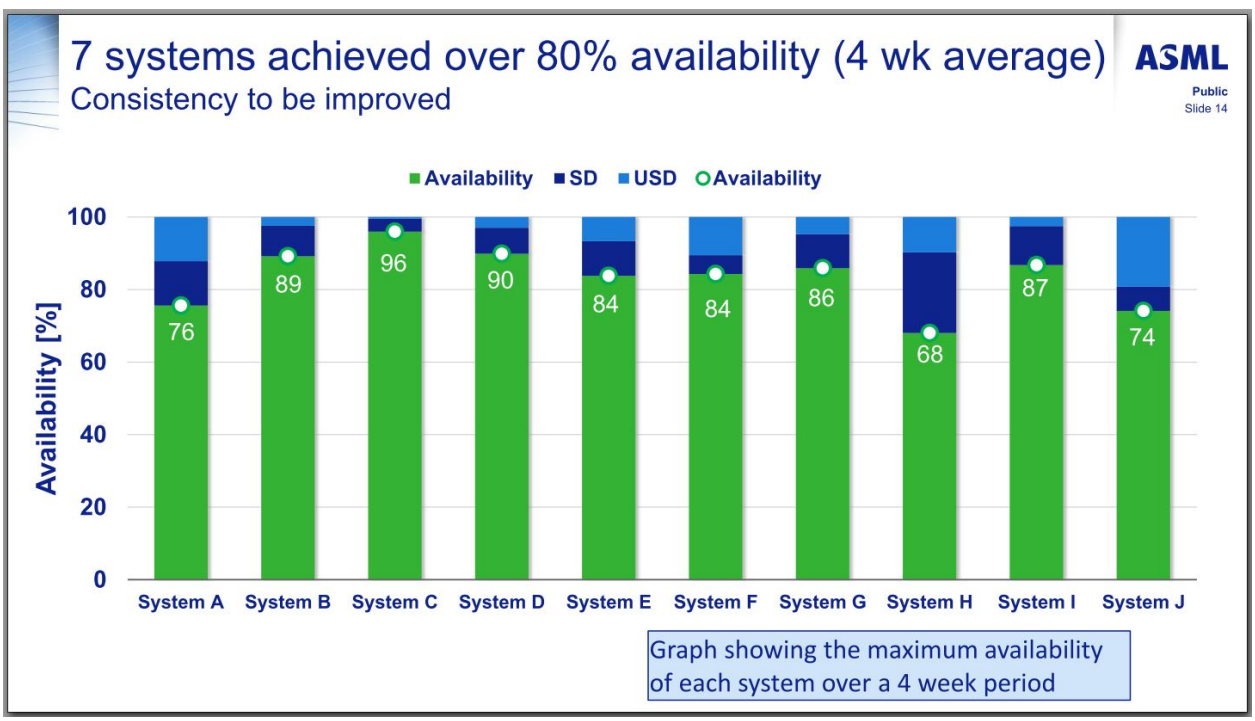

Figure 1.3: EUV stepper availability in the field [3].

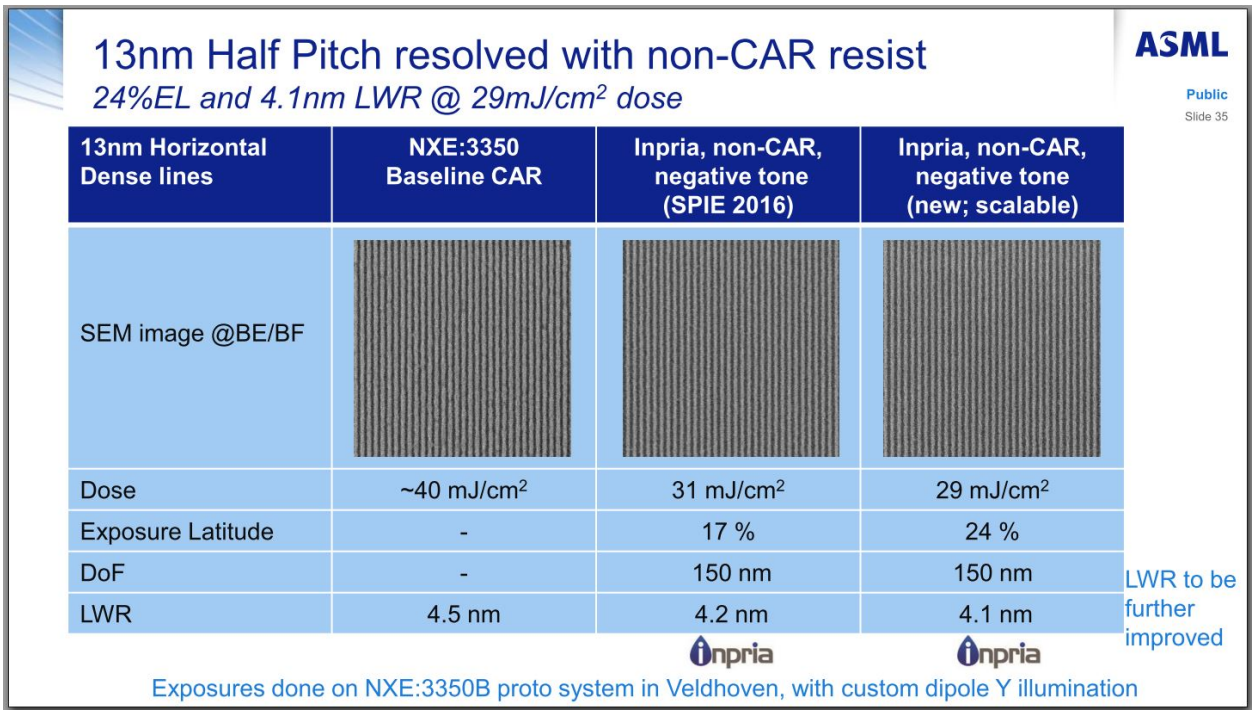

13nm Half Pitch resolved with non-CAR resist

24%EL and 4.1nm LWR @ 29mJ/cm² dose

ASML

Public

Slide 35

13nm Horizontal Dense lines	NXE:3350 Baseline CAR	Inpria, non-CAR, negative tone (SPIE 2016)	Inpria, non-CAR, negative tone (new; scalable)
SEM image @BE/BF			
Dose	~40 mJ/cm²	31 mJ/cm²	29 mJ/cm²
Exposure Latitude	-	17 %	24 %
DoF	-	150 nm	150 nm
LWR	4.5 nm	4.2 nm	4.1 nm
		Inpria	Inpria

LWR to be further improved

Exposures done on NXE:3350B proto system in Veldhoven, with custom dipole Y illumination

Figure 1.4: Latest Inpria metal photoresist performance in 2016 [3].

For the photomask, the multilayer mirror provides the required reflectivity at the EUV wavelength, and absorber materials are used to form the desired pattern on top of the mirror. Defects from the multilayer mirror or the patterned absorber can cause unexpected distortion of the layout aerial image, which can ruin the device performance on the wafer. For now, the EUV actinic (at-wavelength) mask blank inspection tool and mask qualication tool are ready for commercialization [7, 8]. Moreover, the quality of the mask blank has been approved. 7 nm defect-free test masks have been demonstrated by Intel, as shown in Fig. 1.5 [9]. However, EUV actinic patterned mask inspection still does not have a clear path for development. Beyond mask defectivity, mask 3D effects in EUV lithography can be another challenging issue for image performance and process window enhancement. Due to the comparable size of the EUV wavelength and the mask structure, and also the oblique 6° illumination of the EUV lithography system, the mask 3D effects have a profound impact on both pattern design and the choice of absorber material to get desired aerial image performance, as shown in Fig. 1.6. Currently, tantalum-based (Ta) material system is the choice for the EUV mask absorber, but other materials like Nickel (Ni) have been proposed as alternatives which can reduce mask 3D effects by virtue of their lower material-induced phase and stronger absorption [10, 11]. Also, sub-resolution assist features (SRAFs) provide another approach to mitigate the mask 3D effects [12].

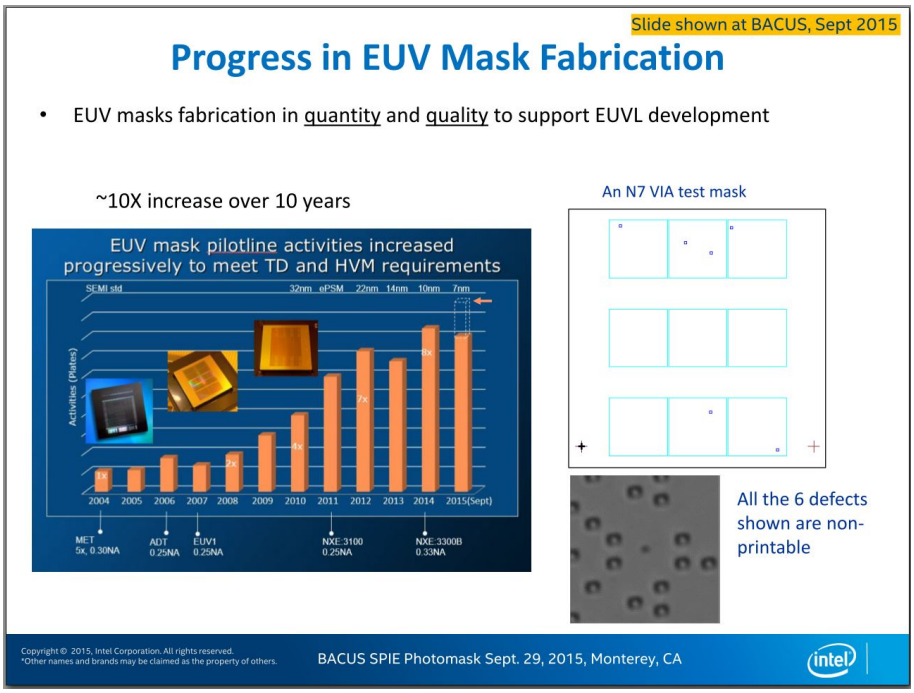

Figure 1.5: Intel demonstrates 7 nm test masks with no printing defect. [9].

1.2 Motivation

For the EUV mask blank inspection, an actinic inspection tool with high throughput is important to make EUV lithography ready for mass production, and high defect detection sensitivity is valuable to deal with tighter mask quality requirements for the future advanced node. When EUV lithography is ready for high-volume manufacturing, the actinic blank inspection tool needs to be able to efficiently identify mask blank defects with surface height < 1 nm.

For EUV patterned masks, because of the limiting resolution from the DUV inspection tool and the insertion of the EUV pellicle which significantly complicates the non-actinic inspection technique, the development of actinic pattern mask inspection tool is needed. Therefore, a detailed actinic inspection tool design option is explored in this dissertation.

For imaging performance on the wafer, the application of sub-resolution assist feature (SRAF) to mitigate the deleterious effect of mask 3D effects on the process window is explored. The industry has widely used SRAFs in DUV lithography. Unlike other proposed solutions which potentially require significant mask-making infrastructure changes, SRAFs can address mask 3D effects locally for different pattern designs and are compatible with current EUV mask fabrication process. Therefore, there is a need to provide physical insight into the optical mechanisms of EUV SRAFs at play that enable mask 3D effects mitigation.

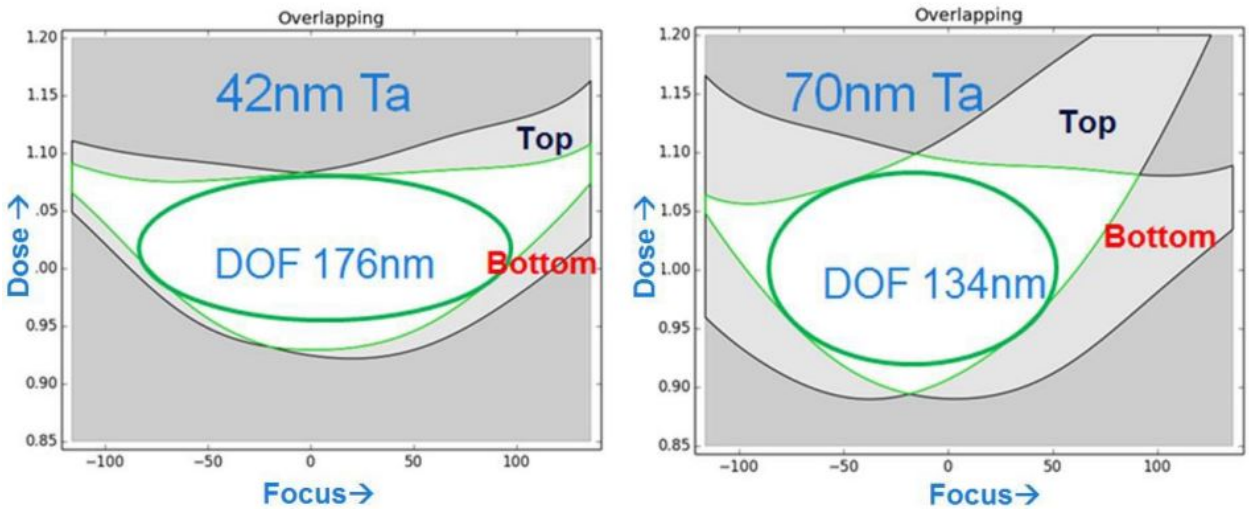

Figure 1.6: Impact of mask 3D effects on overlap process window performance. [13].

1.3 Dissertation contributions

This dissertation is focused on the development of the EUV mask technology, especially on optical inspection technique using EUV light and the study of EUV SRAFs on the mitigation of mask 3D effects for process window enhancement.

A systematic study of the optical configuration for EUV actinic blank inspection is conducted in Chapter 2, including bright field, dark field, and the Zernike phase contrast methods. Both simulation and experimental results show that for a high-resolution imaging system, the Zernike phase contrast method is a better inspection method than the conventional bright field method. Turning instead to lower resolution (scattering type systems), the results show that dark field imaging is preferred method compared to the Zernike phase contrast method. Therefore, a detailed tool design study of an actinic blank inspection tool utilizing dark field imaging is also conducted. Various parameters such as illumination condition, optical NA, source type and source power are shown to have different impacts on the SNR and the final tool design.

The possibility of using optimum phase shift in the pupil plane to improve inspection efficiency is discussed to address issues around EUV patterned mask inspection. The simulation results show that the EUV mask pattern defect is not an ideal absorber defect due to the nature of the absorber materials. By showing the defect near field distribution and defect signal through-focus behavior, the impact of the choice of the absorber materials and pupil design on defect detection sensitivity is discussed. At the end of Chapter 3, a bright field based EUV patterned mask inspection tool design study is conducted. The impact of noise sources such as speckle noise, camera noise, and photon shot noise on defect detection sensitivity are discussed step by step to show which noise source is the key factor in improving the SNR to capture the critical defects on the EUV mask. Moreover, comparison between

the bright field method and the optimum phase shift method shows that even though the optimum phase shift method can improve defect signal, it is not the most effective inspection method when all noise sources are taken into consideration.

For the EUV SRAF study, the scattered order analysis shows that extra aberration is introduced into the imaging process by the SRAFs. However, with the combined contribution from the illumination sources and the effect of oblique illumination, balanced Bossung curves and larger process window can be achieved. The simulation results also show that SRAFs have a different impact on the overall imaging process, which might result in different restrictions on the SRAF position for the mask-making process.

Finally, the Fresnel zoneplate pattern generation algorithm used for the EUV mask blank inspection experiment is presented. The algorithm can generate zoneplate patterns efficiently for conventional or exotic imaging modes, and there are features in the algorithm to improve the yield of the zoneplate by optimizing its fabrication conditions. This code has been generalized and made available to researchers who want to use Fresnel zoneplate as their imaging optics.

1.4 Dissertation structure

In Chapter 2, the possibility of enhancing the phase defect detection sensitivity using EUV actinic blank inspection is discussed. The thin mask simulation result at EUV wavelength is presented to compare the inspection efficiency between the bright field method and the Zernike phase contrast method. Through-focus defect aerial images and the defect SNR calculation are used to compare the defect detection sensitivity. The experimental results from a programmed bump defect mask using the SHARP EUV microscope are then presented to verify the simulation results. The experimental data also shows the nature of the defect extracted using a phase retrieval algorithm, showing that the multilayer defect is transformed from a pure phase defect to a mixed (phase + absorption) defect as defect size increases. A comparison between the Zernike phase contrast method and the dark field method is conducted, and the results show that the dark field method is better configuration for inspection mode due to higher defect SNR. With this result, the inspection tool design study is conducted for EUV actinic blank inspection using the dark field configuration at the end of Chapter 2, discussing the impact of optical system design parameters including pixel size, photon collection efficiency, and EUV source type on SNR performance. The results are compared with Lasertec's tool design [7] and possible paths to improving the defect sensitivity are proposed.

Chapter 3 focuses on patterned mask inspection. First, the possibility of using optimum phase shift to improve inspection efficiency by identifying both phase and amplitude defects simultaneously is discussed. Then the phase effects of pattern defects is analyzed, trying to utilizing the material-induced phase from the absorber material to increase defect detection sensitivity. Chapter 3 ends with an assessment of the impact of various noise sources and

optical design on pattern defect detection sensitivity for a bright field based EUV actinic pattern inspection tool.

By analyzing the Bossung curves and the aerial images of a semi-isolated 2-bar pattern, the impact of SRAFs on process window enhancement is presented in Chapter 4. Moreover, the physics of why EUV SRAFs can mitigate EUV mask 3D effects is explained by analyzing the scattered orders retrieved from the pupil plane of each illumination pole. The simulation results on SRAFs' positions further show the role of each SRAF in the overall imaging process.

Finally, Chapter 5 shows the detail process flow of a new algorithm developed to generate the desired Fresnel zoneplate pattern. The GDSII (Graphic Database System) pattern images are shown alongside with the process flow to demonstrate the algorithm. Moreover, a new rendering algorithm which can transfer the pattern into multiple file formats for the lithography process is presented to show the flexibility on the computation time and the precision of the desired pattern. Scanning electron microscope (SEM) images of the Fresnel zoneplate from the experiment show the capability of the algorithm at the end of Chapter 5.

Chapter 2

Enhancing Phase Defect Detection Sensitivity for Extreme Ultraviolet Actinic Mask Blank Inspection

In this chapter, EUV actinic blank inspection tool development configuration options are studied. Section 2.1 describes the motivation for EUV mask blank inspection. Section 2.2 discusses the possibility of using the Zernike phase contrast method to increase the phase defect detection sensitivity. Section 2.3 shows experimental demonstration of the Zernike phase contrast method using the SHARP EUV microscope at (LBNL). This section includes the impact of the Zernike phase contrast method on signal-to-noise ratio (SNR) enhancement. In Section 2.4, a direct performance comparison of the Zernike phase contrast method and the dark field method is presented. Finally, Section 2.5 describes the impact of system configuration on the dark field imaging mode considering the impact of pixel size, EUV source type, and photon collection efficiency on defect SNR performance.

2.1 Background

Figure 2.1 shows the general mask-making process flow. After mask blank fabrication, inspection is needed to ensure the mask quality and locate critical defects and their position before blank suppliers deliver the mask blanks to the mask shop. After receiving the blanks, mask shops conduct another blank inspection to verify the mask quality and the defect information provided by the blank supplier before patterning. After mask patterning, a pattern inspection is conducted by the mask shops to identify pattern defects before the mask is sent to the wafer fab for wafer printing. When the patterned mask is used in the fab, pattern inspection is conducted routinely to ensure continued quality.

Figure 2.2a shows a schematic diagram of an EUV mask blank with absorber on top of it. Due to low reflectivity of materials at 13.5 nm EUV lithography wavelength, an EUV mask blank is made out of a multilayer mirror consisting of 40 molybdenum (Mo) and silicon (Si)

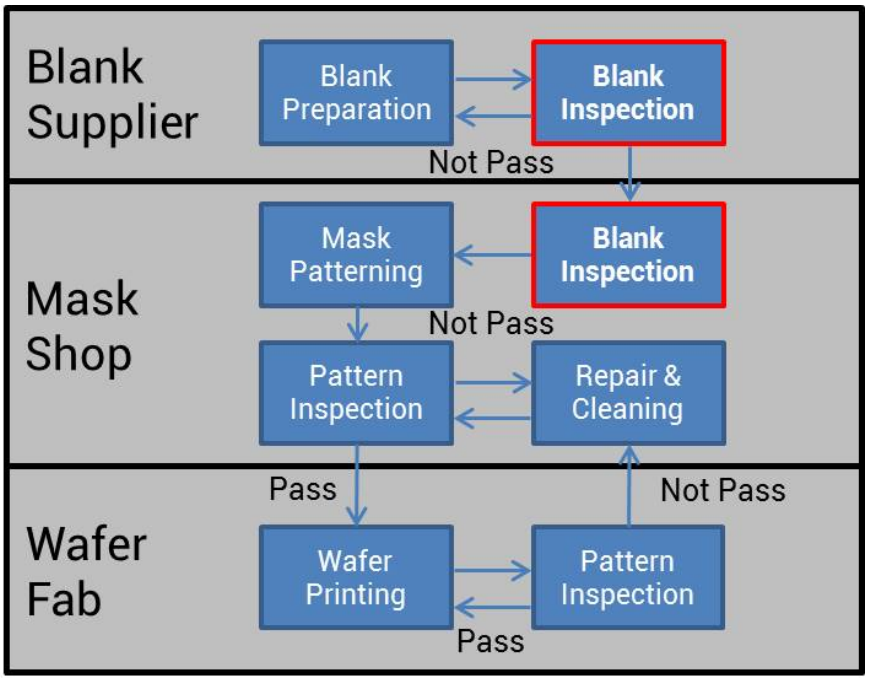

Figure 2.1: The process flow of photomask fabrication [14].

bi-layers. The substrate is a low thermal expansion material (LTEM) to ensure a low spatial fluctuation under continued EUV light exposure. Moreover, surface flatness and substrate defectivity are both critical factors for the mask blank quality. Scratches or particles on the substrate can turn into phase-dominated blank defects even after multilayer deposition [15], as shown in Fig. 2.2b. These phase defects are hard to identify and can cause unexpected CD variation on the desired pattern. On top of the multilayer mirror, a ruthenium (Ru) capping layer with the thickness of 2.5 nm is used to prevent the oxidation of Si layer. The EUV mask blank structure is optimized to maximize the reflecitivity at 13.5 nm wavelength. The theoretical peak reflectivity is around 72%, but the state-of-the-art is less than 70% [16, 17]. In addition to the multilayer, blank suppliers also typically deposit EUV absorber and anti-reflection coating before they send the EUV mask blank to the mask shop. Ta-based absorber material is commonly used in current EUV mask design, but other novel structures or materials have been proposed to further improve the imaging performance by increasing contrast or reducing the mask 3D effects [18].

Since 2009, the EUV mask blank defectivity has been considered one of the most challenging problems facing EUV lithography because it significantly limits the mask yield [19]. The size and the number of the blank defects need significant improvement in order to be ready for high-volume manufacturing. In the past few years, major progress has been made on both the EUV mask blank and EUV mask blank inspection tools. For EUV mask blanks, the mask quality has been improved and the number of critical defects is finally down to

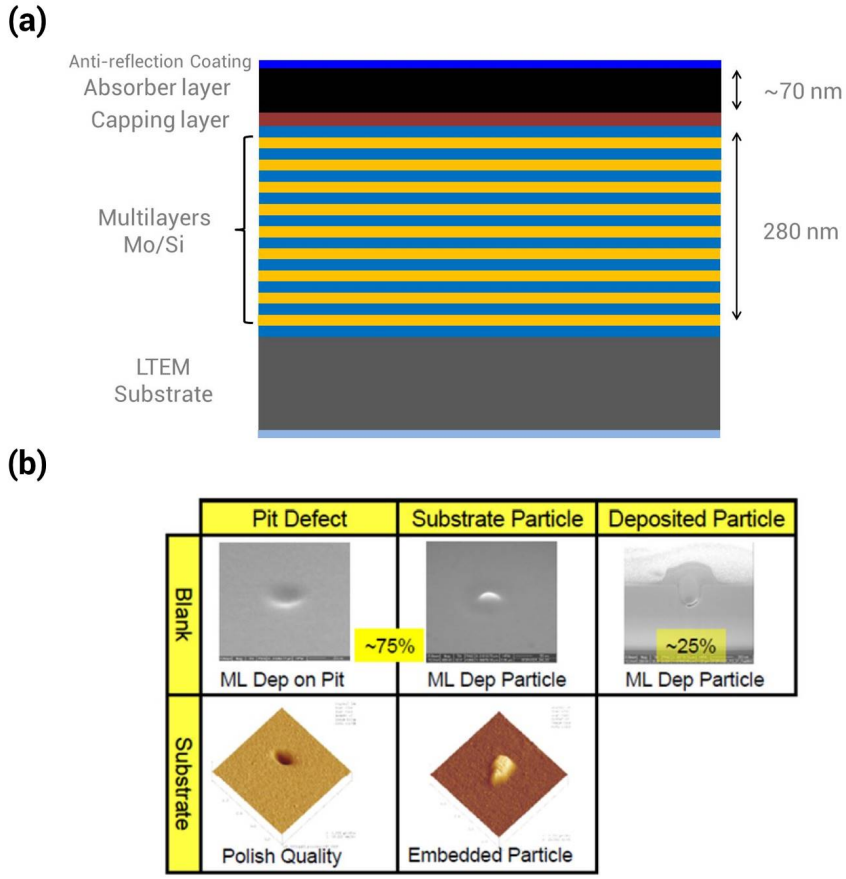

Figure 2.2: (a) Schematic diagram of EUV mask blank with absorber on top of it. (b) EUV mask blank defect types [15].

single digit, as shown in Fig. 2.3. By utilizing mask pattern shift methods, one can hide all the defects under the absorber. Both N7 and N10 defect-free masks have been demonstrated [4]. However, meeting the manufacturing defect specifications will require an actinic blank inspection tool with high defect sensitivity and precise defect location capabilities [20]. However, a commercially available actinic blank inspection tool is not yet ready, even though a tool has been developed and demonstrated by EIDEC, as shown in Fig. 2.4.

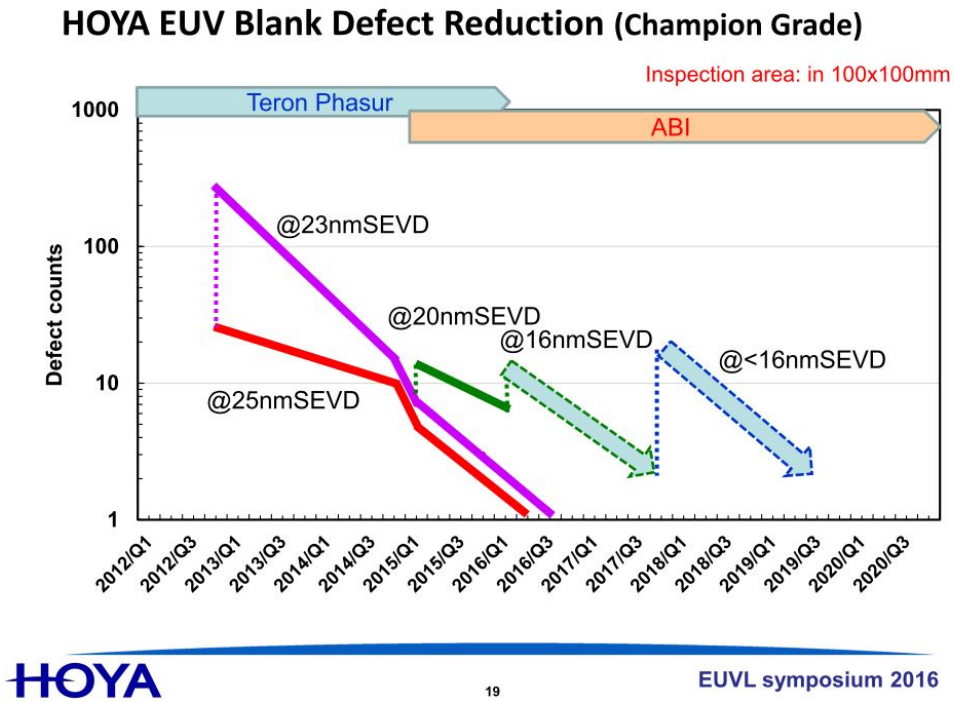

Figure 2.3: EUV mask blank defect reduction since 2012 [19]. SEVD: Spherical equivalent volume diameter.

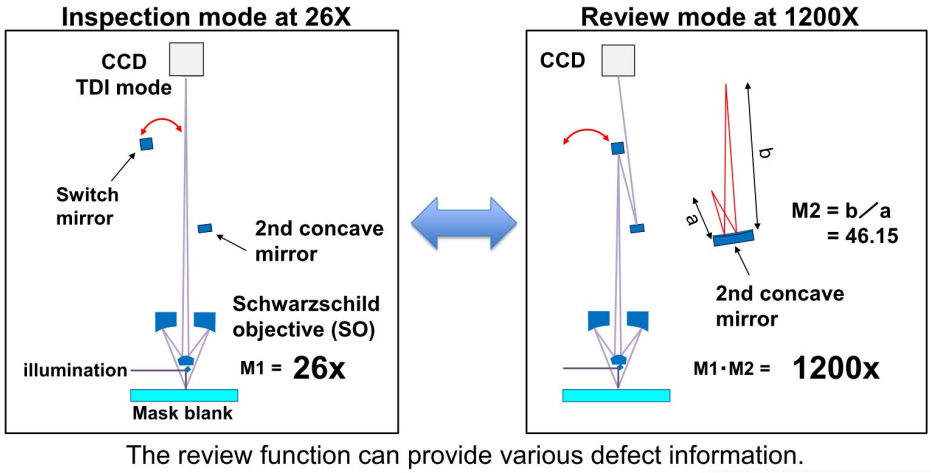

Figure 2.4: The optical configuration for 2 different inspection modes of the actinic blank inspection tool designed by EIDEC [20].

2.2 Simulation study of the impact of the Zernike phase contrast microscopy on phase defect detection sensitivity

Critical phase defects for advanced nodes may represent height deviations at the top of the multilayer of only a fraction of a nm. This makes actinic inspection critical, but even for actinic inspection, finding such small phase defects on a blank can be extremely challenging.

Zernike phase contrast microscopy has been developed for many years and is one of the most useful methods to observe phase objects [21]. The performance of a Zernike phase contrast microscope can be explained using what is known as a phasor diagram, as shown in Fig. 2.5a. Here, the length of the vector indicates the magnitude of the electric field and the direction or angle represents the relative delay of the sinusoidal wave. Rotating the angle a quarter circle clockwise represents a quarter wavelength delay known as a 90° phase shift. This diagram allows electric field contributions from multiple waves with various delays to be summed up by simply adding the directed vector lengths of each wave.

As shown in Fig. 2.5a, a phase object or phase defect typically has very little absorption of background light (B). However, it can create an additional electric field component (D) due to the optical path difference created by the refractive index difference between the object and the environment as light passes through it. The object information (D) in the case of a 90° phase shift is perpendicular to B. The resulting vector sum (M) is nearly unchanged in length. This means that the object (D) is nearly undetectable in measuring the light intensity, which is proportional to the square of the length of M. However, if the phase of B is changed by rotating B 90° counter clockwise, the length of M is reduced by the size of D and the light intensity is reduced to $(M - D)^2$, as shown in Fig. 2.5b. Figure 2.5c shows the case of a clockwise rotation of B leading to an increase in light intensity to $(M + D)^2$. Figure 2.5d shows the improvement in the relative intensity variation by attenuating the collection of the reference background B with what is known as apodization of the lens. Here B is reduced to B' and when the D vector is added only M' remains. Thus the light intensity goes from $(B')^2$ to $(M')^2$ which is typically a larger dynamic range. This method can be applied to phase defects on EUV mask blanks, which similarly only changes the optical path of the light that is projected on it with little absorption.

2.2.1 Simulation settings and parameters for modeling EUV mask blank inspection

The simulation study uses a thin mask 2D model to generate the EUV (13.5 nm) images. To model the defect and mask roughness which are shown in Fig. 2.6, the single surface approximation is used to describe the phase function of the object [22]. The defect and mask roughness images are simulated independently to account for the impact of defect signal and speckle noise respectively. Since a defect can be viewed simply as an extreme event in the mask roughness height distribution, the defect height profile is not directly added to the mask

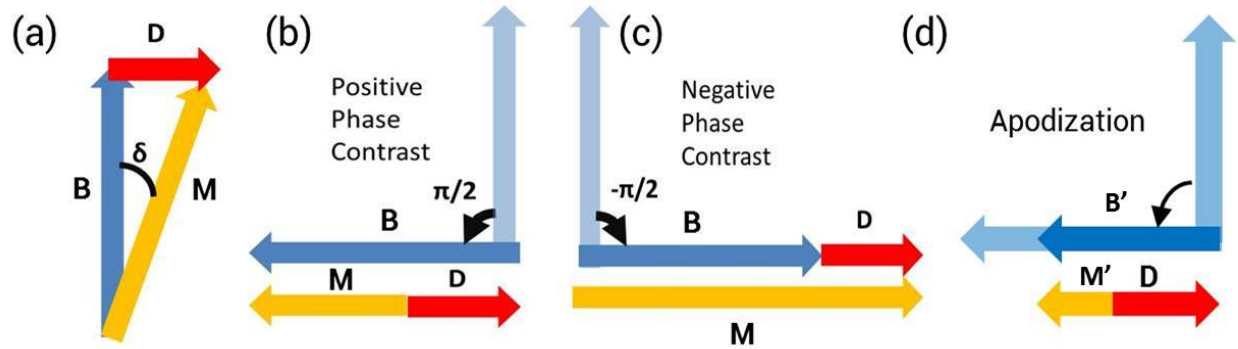

Figure 2.5: Phasor diagram for phase object: (a) The conventional bright field (0° phase shift). (b) The Zernike phase contrast method with +90° phase shift. (c) The Zernike phase contrast method with −90° phase shift. (d) The Zernike phase contrast method with +90° phase shift and apodization. (B: Background intensity, D: Defect wave, M: Measured intensity, δ: Original phase shift)

roughness height profile. Gaussian-shaped phase defects with height ranging from 0.5 to 1.5 nm and an FWHM ranging from 10 to 100 nm are used [9]. The defect shape definition is shown in Fig. 2.7. The mask roughness is assumed to be 77 pm in root-mean-square (RMS) with a correlation length ≈ 100 nm [23, 24, 25].

For the imaging conditions, an outer NA of 0.2 and a disk illumination NA of 0.1 are used as described in Ref. [26]. In order to include phase shift and apodization to improve the defect sensitivity, the pupil function is modified with a ±90° or +180° phase shift which has a shape matched to the disk illumination in order to manipulate the background light. Apodization is defined as the electric field transmission of the background level of the pupil function, ranging from 25% to 100%.

Defect signal strength and defect SNR are defined in Eq. 2.1 and Eq. 2.2. In this section, the noise sources are simplified to speckle noise and system noise. Speckle noise is induced by mask roughness and is calculated by the standard deviation of intensities resulting from the image of a rough mask blank. System noise is a constant accounting for all the other noise sources which are independent of the mask, such as electrical noise from the camera. Larger SNR means the defect is more distinguishable from the noise, which leads to a higher capture rate:

$$\text{Defect Signal} = \frac{\text{Peak Intensity} - \text{Reference Intensity}}{\text{Reference Intensity}} \tag{2.1}$$

$$\text{Defect SNR} = \frac{\text{Defect Signal}}{\text{Speckle Noise} + \text{System Noise}} \tag{2.2}$$

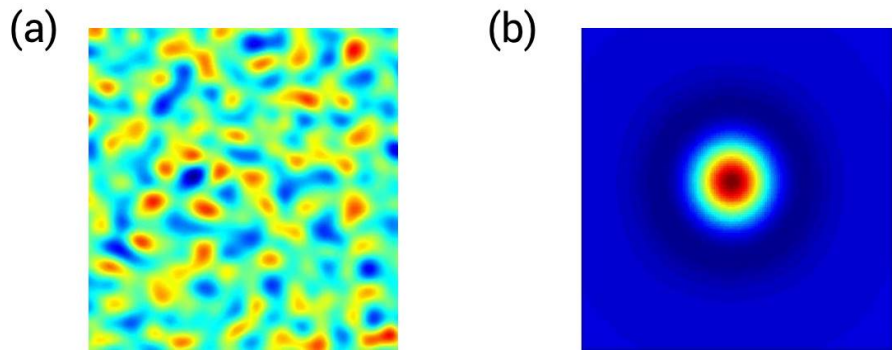

Figure 2.6: (a) The phase of the mask roughness. (b) The phase of the Gaussian-shaped defect.

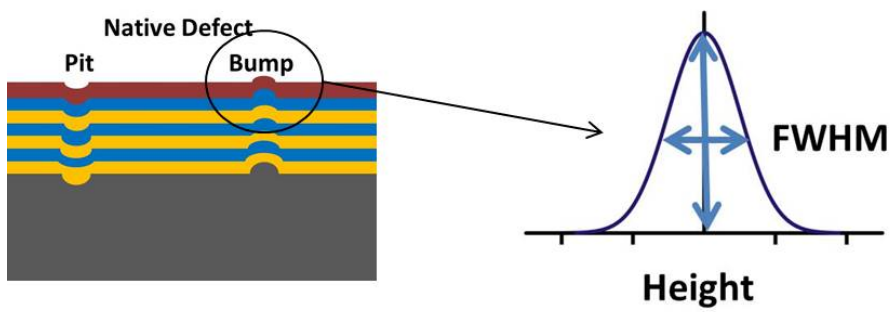

Figure 2.7: Schematic diagram of the multilayer defect, and the definition of the Gaussian-shaped defect.

2.2.2 Impact of the Zernike phase contrast method on phase defect detection sensitivity

Figure 2.8 shows the aerial images at different defocus levels for both bump and pit defects, with the conventional bright field and the Zernike phase contrast method. The defect height/depth is 1 nm and the width is 60 nm [9]. Due to the +90° phase shift added to the background wave, the defect sensitivity has been improved at best focus for the Zernike phase contrast method, while the phase defect is invisible under bright field imaging.

The defect signals at different defocus levels are shown in Fig. 2.9a. With the Zernike phase contrast method, both bump and pit defects have their peak signal strengths at best focus and the signal strength can be improved by 30% at the best scenario. This shows the potential to do an in-focus inspection for phase defects with a higher sensitivity. The differences in the peak defect signal between bump and pit defects are due to the fact that in both cases the +90° phase shift is applied to the pupil. This means that the bump defects

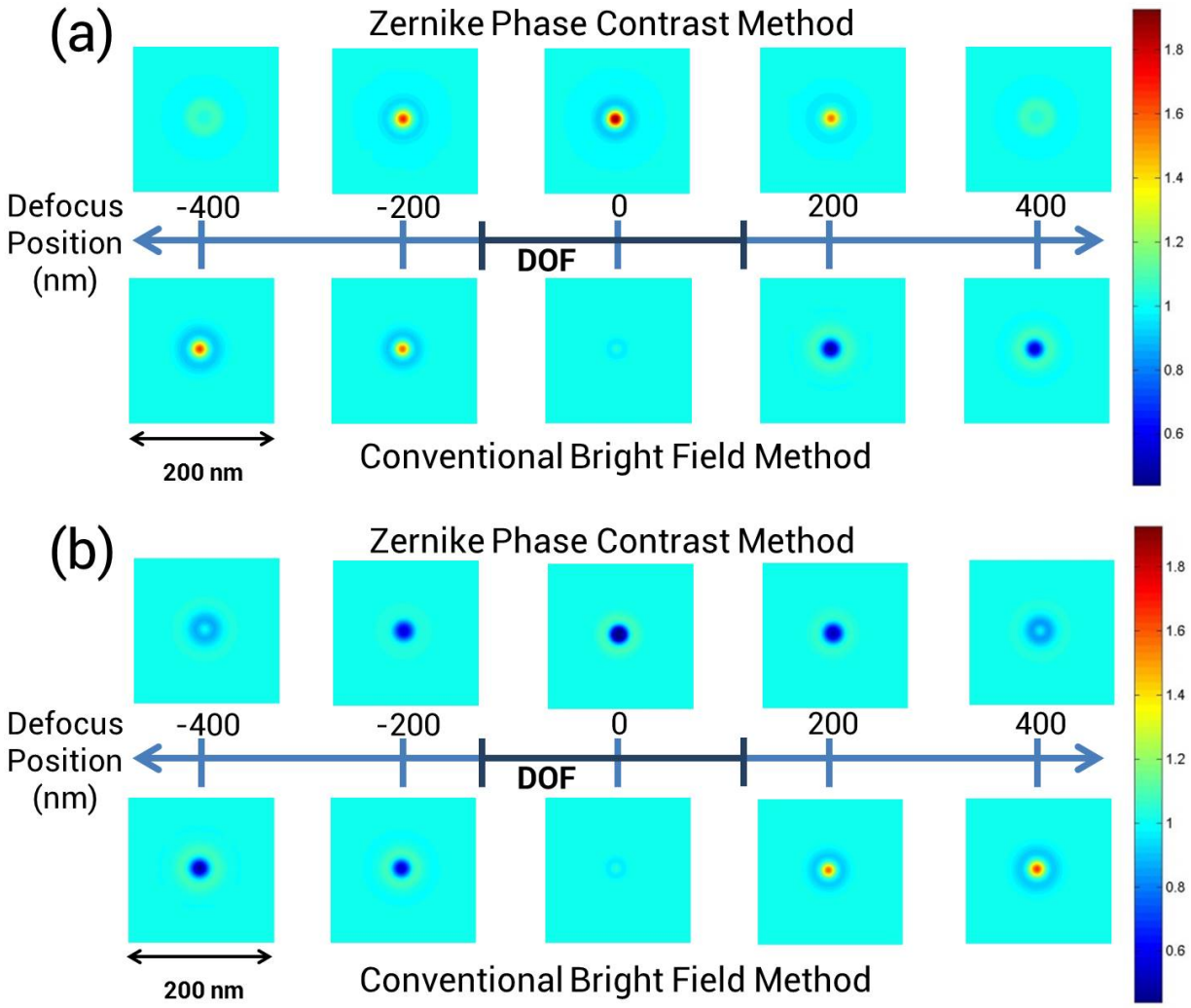

Figure 2.8: Aerial images for phase defect at different defocus levels with the Zernike phase contrast method (+90° phase shift) and the conventional bright field: (a) Bump defect (Height: 1 nm, FWHM: 60 nm). (b) Pit defect (Depth: 1 nm, FWHM: 60 nm).

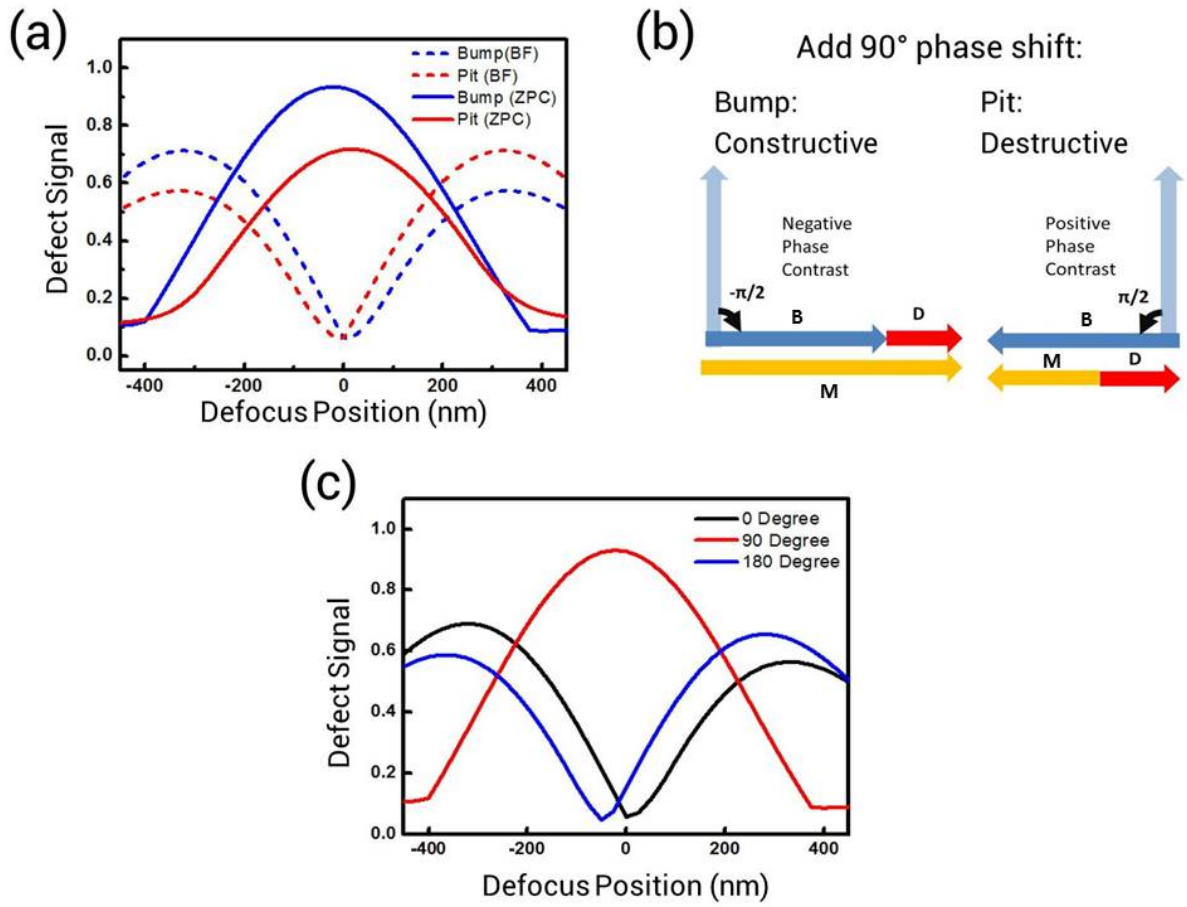

Figure 2.9: (a) Defect signal at different defocus levels using the Zernike phase contrast method (solid curve) or the conventional bright field method (dash curve). Defect Height / Depth = 1 nm. Defect FWHM = 60 nm.(b) Phasor diagram for bump defect and pit defect with a +90° phase shift to its background. (B: Background intensity, D: Defect wave, M: Measured intensity) (c) Defect signal at different defocus levels under different phase shifts in the pupil plane: 0° (Black), +90° (Red), and +180° (Blue). Defect Height = 1 nm. Defect FWHM = 60 nm.

interfere constructively with background light, whereas the pit defects interfere destructively, as shown in Fig. 2.9b. Figure 2.9c shows the bump defect's through-focus behavior for 3 different phase shifts in the pupil plane. At +180° phase, the through-focus behavior is the opposite compared to the conventional bright field (0°) situation.

The defect signal increases with an increase in the defect height, as shown in Fig. 2.10a. Interestingly, with same defect height/depth at 1.5nm, the bump defect signal is 1.4 whereas the pit defect signal is only 0.9. The pit defect signal sensitivity is different from the bump

defect as the defect height/depth varies. This is due to the fact that pit defect is utilizing a different mechanism to improve the defect signal compared to bump defect. For pit defects with a $+90°$ phase shift, the largest destructive interference occurs when the background intensity has the same amplitude as the defect and both get canceled out. Thus based on our definition, the largest signal strength for destructive interference is 1, which explains why pit defects have lower signal strength than bump defects under a $+90°$ phase shift. If a $-90°$ instead of a $+90°$ phase shift is applied to the pupil function, bump defects utilize destructive interference to improve the defect signal and have lower sensitivity to the defect height variation. Pit defects, which utilize constructive interference to enhance the defect signal, have larger signal strength than bump defects and higher sensitivity to the defect height variation. The orientation of the phase shift determines the defect signal sensitivity to the defect height.

Moreover, the defect signal increases first then decreases with an increase in the defect width, as shown in Fig. 2.10b. At the first stage, below the resolution limit, scattered light from the defect cannot be collected by the pupil due to its large diffraction angle. As the defect size increases, the scattering angle becomes smaller and more light is collected by the pupil, thus the defect signal increases. At the second stage, the scattering angle decreases with an increase in the defect size. Part of the scattered light gets into the central phase-shifted region which is used to phase shift the background intensity, thus the phase contrast effect is reduced. This indicates that a proper pupil design is necessary in order to maximize the defect signal from the target defect. Moreover, if the defect width is varied, the peak defect signal position varies for the conventional bright field method, but stays at the same position for the Zernike phase contrast method, as shown in Fig. 2.10c. This shows another advantage of the Zernike phase contrast method: the largest signal at best focus can be collected without any dependence on the defect shape.

To further improve contrast, the apodization method is utilized to reduce the background intensity level. Figure 2.11 shows the result of a bump defect with different apodization levels. For the case with only 25% background electric field transmission (0.25 APD), the defect signal has a $6\times$ enhancement compared with the case with 100% background electric field transmission (1.0 APD). However, the pit defect suffers from the use of destructive interference. This will be discussed in the Section 2.4, but the result is that apodization is not the best way to improve the pit defect signal.

2.2.3 Impact of the Zernike phase contrast method on phase defect SNR

As shown in the previous section, the defect SNR is defined as defect signal divided by speckle noise plus system noise. Therefore, the Zernike phase contrast method has to not just improve the defect signal, but it must also not increase the speckle noise.

Fig. 2.12a shows the speckle noise through-focus behavior under the Zernike phase contrast method and the conventional bright field method. Since the mask roughness is also

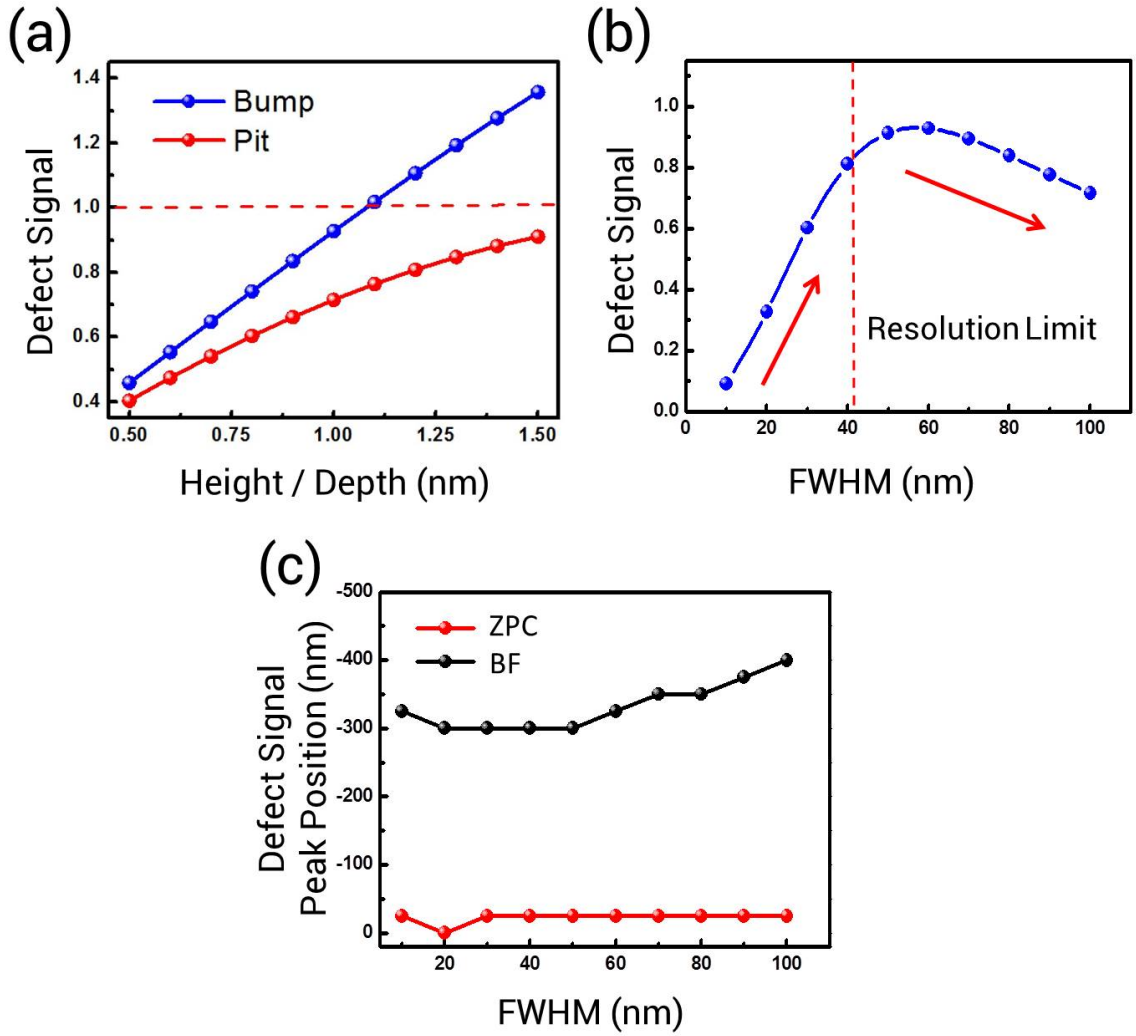

Figure 2.10: (a) Defect signal of the bump (Blue) and the pit (Red) defects at best focus with different defect heights using the Zernike phase contrast method. Defect FWHM = 60 nm. (b) Defect signal of bump defects at best focus with different defect widths using the Zernike phase contrast method. Defect Height = 1 nm. (c) Peak defect signal position using the Zernike phase contrast method (Red) or the conventional bright field method (Black). Defect Height = 1 nm. Defect FWHM = 60 nm.

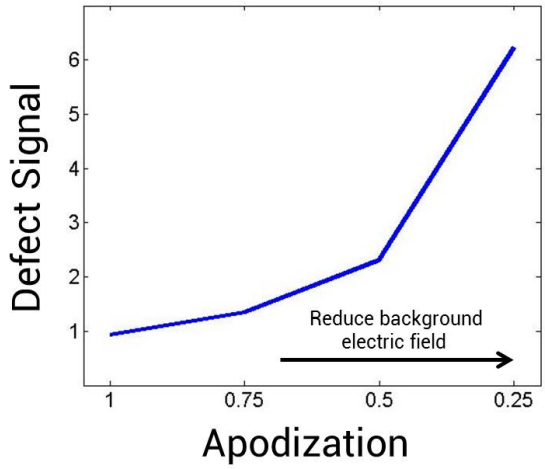

Figure 2.11: Defect signal of bump defect at best focus with different apodization conditions using the Zernike phase contrast method. Defect Height = 1 nm. Defect FWHM = 60 nm. 1.0 apodization means the background electric field transmission is 100%. 0.25 apodization means the background electric field transmission is 25%.

phase-dominated, a similar trend as defect signal is expected. This indicates that both defect signal and speckle noise at best focus are amplified with a +90° phase shift in the pupil plane. Even though the signal and noise are increased at the same time, the defect signal has a stronger enhancement than speckle noise, thus resulting in larger SNR at best focus. With the consideration of system noise, the noise is increased by 2× while the signal is increased by 16×, which results in an overall 7.7× enhancement on defect SNR at best focus.

Comparing the best scenario between these two different approaches, the defect SNR at best focus using the Zernike phase contrast method is still 18% higher than the best defect SNR that can be achieved by the conventional bright field method, as shown in Fig. 2.12b. The results shown here indicate that a higher defect sensitivity and in-focus inspection can be achieved by the Zernike phase contrast method to improve inspection efficiency of the actinic blank inspection tool.

The other aspect in the defect SNR enhancement by the Zernike phase contrast method is the role of the system noise. As shown in Fig. 2.12c, the magnitude of the system noise determines the impact of the Zernike phase contrast method on SNR. If the system noise is the dominant noise source, the impact of the Zernike phase contrast method is mainly on the defect signal while the noise term stays almost constant, thus resulting in larger SNR. On the other hand, if the speckle noise is the dominant noise source, the impact of the Zernike phase contrast method can be on both the defect signal and the speckle noise, which changes the noise terms in Eq. 2.2 accordingly. Therefore, it can result in smaller SNR enhancement.

Figure 2.13a shows the signal, speckle noise, and defect SNR results at best focus with

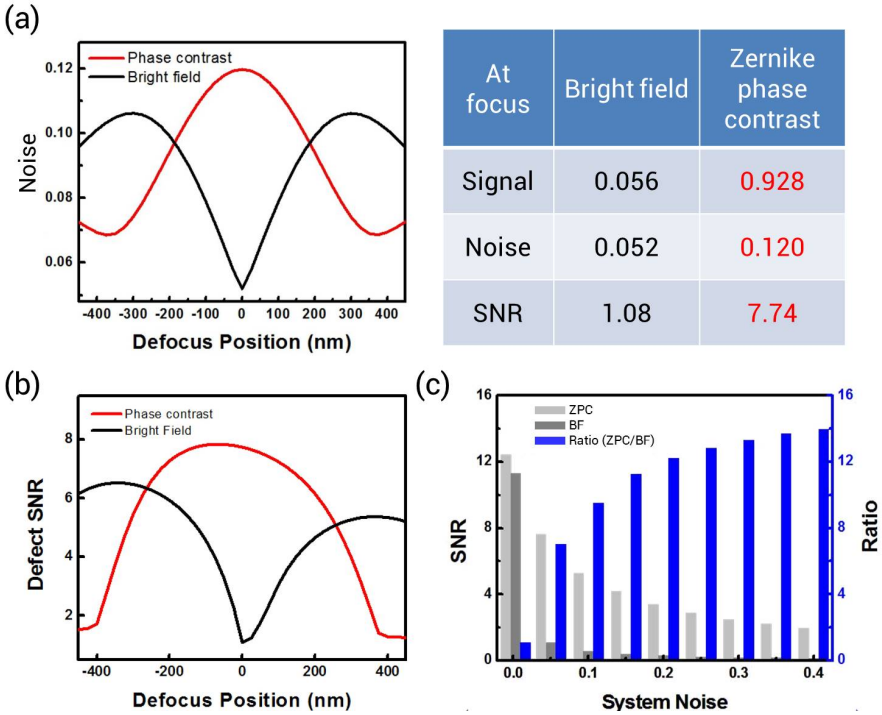

At focus	Bright field	Zernike phase contrast
Signal	0.056	0.928
Noise	0.052	0.120
SNR	1.08	7.74

Figure 2.12: (a) Noise at different defocus positions using the Zernike phase contrast method (Red) and the conventional bright field method. The list shows the signal, noise, and SNR at best focus by these 2 methods. (b) Defect SNR at different defocus positions by the Zernike phase contrast method (Red) and the conventional bright field method (Black). Defect Height = 1 nm. Defect FWHM = 60 nm. System Noise = 5%. (c) Defect SNR at best focus by 2 different methods under different system noise. The ratio indicates the relative enhancement by the Zernike phase contrast method over the conventional bright field method. Defect Height = 1 nm. Defect FWHM = 60 nm.

+90° and apodization. Without normalizing the defect signal and speckle noise to the background level at different apodization conditions, their absolute values are lower as the background transmission decreases. However, the speckle noise drops faster than the defect signal. The difference is due to their frequency distribution. In this analysis, the phase defect FWHM is 60 nm, while the mask roughness correlation length is ≈ 100 nm. The width and the correlation length are mask features determined by the multilayer deposition process. As shown in Fig. 2.13b, the mask roughness has a dominant low-frequency component. This is the reason why by applying the apodization in the pupil design can have a stronger reduction in speckle noise than defect signal thereby improving the SNR. Note that this conclusion would change, should the relative spectral content between defects and mask roughness change.

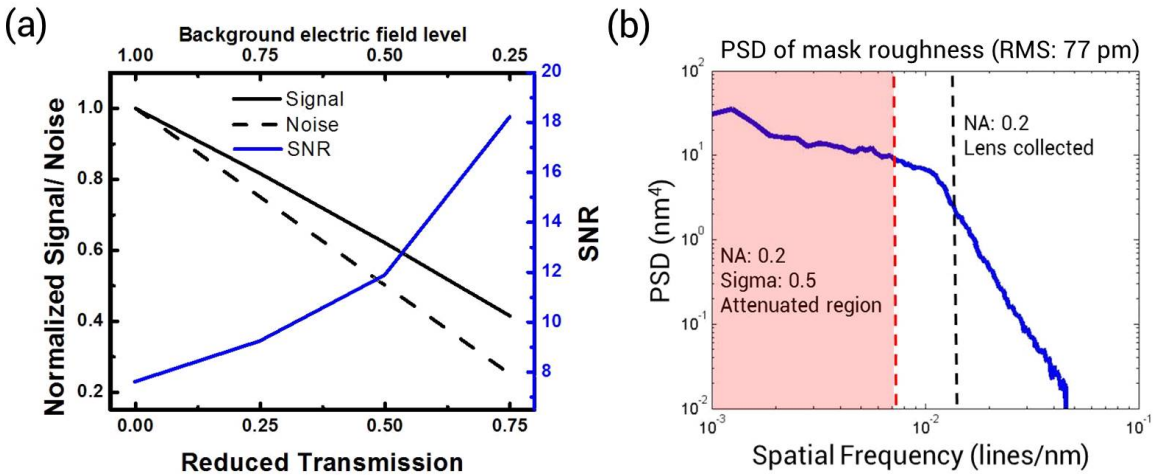

Figure 2.13: (a) Defect signal (Black, solid), speckle noise (Black, dash), and defect SNR (Blue) under different apodization conditions. The x-axis shows the reduced transmission or background electric field level. The signal and noise shown here are not normalized to the background level. Defect Height = 1 nm. Defect FWHM = 60 nm. System Noise = 5%. (b) Surface roughness power spectrum density (PSD) by scatterometry measurement of the EUV mask.

The results shown here indicate that the Zernike phase contrast method has some advantages over the conventional bright field method for blank inspection. However, the benefit of apodization on defect SNR depends on the type of defect. Moreover, if apodization is applied to the pupil plane design and further lowers the background transmission to 0, the imaging system enters the dark field configuration. The defect SNR behavior in the dark field method is different from the Zernike phase contrast method and needs to be discussed. A detailed study on a comparison between the dark field method and the Zernike phase contrast method is conducted in Section 2.4.

2.3 Experimental result of the Zernike phase contrast method on programmed defect mask using the SHARP EUV microscope

First, defect SNR comparison between the conventional bright field method and the Zernike phase contrast method is presented for the smallest defect found on a programmed defect test mask using the Zernike phase contrast method. Then data is presented from a variety of defect sizes, and the impact of absorption on defect signal through-focus behavior is discussed. Finally, through-focus defect images are shown for the inspection of a native

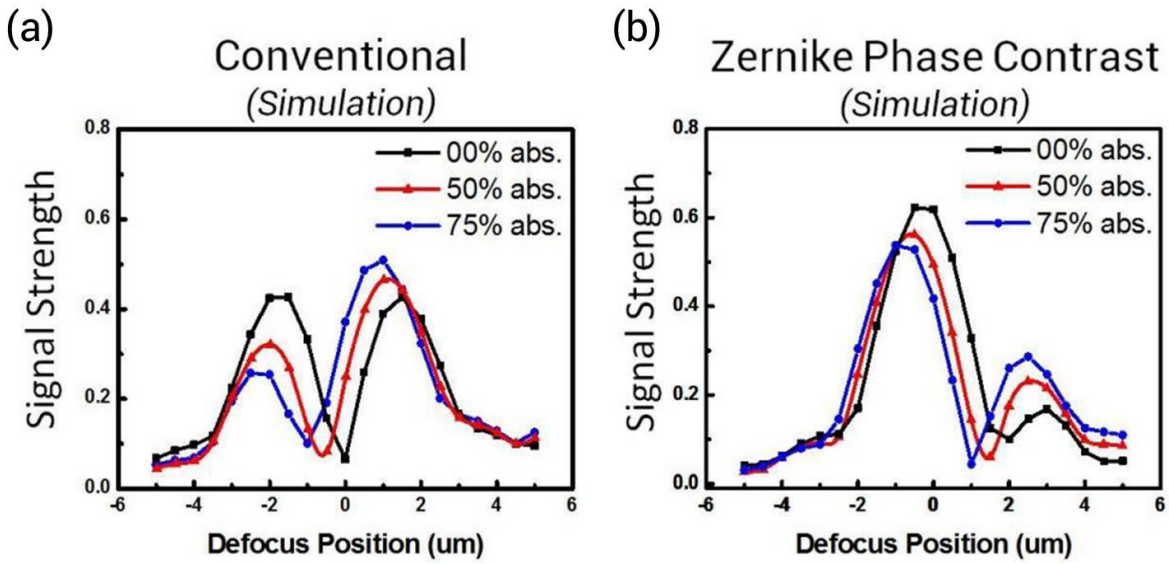

Figure 2.14: (a) Simulation results of defect signal at different defocus positions using the conventional bright field method: Pure phase defect (Black), phase defect with 50% electric field absorption (Red), phase defect with 75% electric field absorption (Blue). (b) Simulation results of defect signal at different defocus positions using the Zernike phase contrast method with the same labeling conventions as in (a).

bump defect under various apodization conditions.

2.3.1 Background on interpreting measured defect information

To determine the actual defect information on the programmed mask, a phase retrieval algorithm based on the weak object approximation is used [27]. The extracted defect data will enable quantitative comparison of the experimental results to expected and modeled results.

Although for convenience phase and absorber defects are considered separately, in reality, true defects are almost always a combination of the two types [28]. To address this fact, the effectiveness of the Zernike phase contrast method in the presence of such real world mixed defects is discussed. The simulated through-focus impact of increasing defect absorption in the conventional bright field method is shown in Fig. 2.14a. The defect signal at best focus increases with the absorption. Despite this significant change in behavior with defect absorption, the Zernike phase contrast method can still manipulate the phase component of the defect and enhance the defect sensitivity, as shown in Fig. 2.14b.

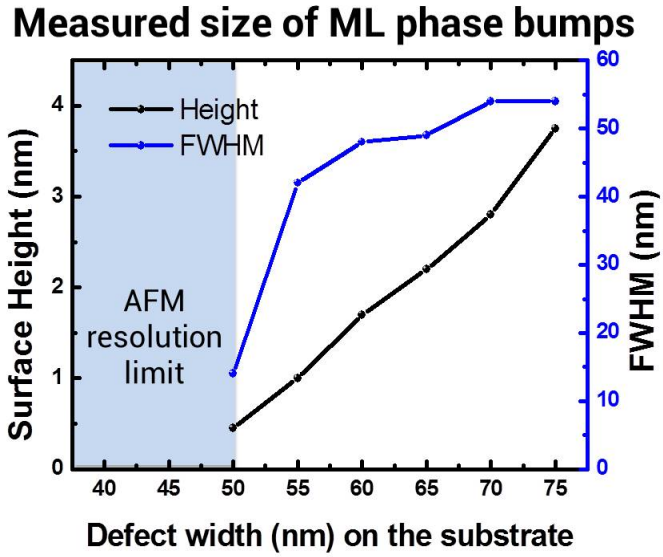

Figure 2.15: The measured programmed defect height (Black) and FWHM (Blue) on the surface by AFM. The defect information for defects with a width 40 nm and 45 nm on the substrate are below AFM detection sensitivity.

2.3.2 Experimental settings and parameters

The test sample for the experiment is a programmed defect mask [29]. The substrate defects are defined by electron-beam lithography using a 48 nm thick hydrogen silsesquioxane (HSQ) photoresist with a square shape on a quartz substrate. The target defect sizes are from 40 to 75 nm and are considered effectively isolated defects. Figure 2.15 shows the height and the FWHM of the programmed defects on the multilayer surface as measured by atomic force microscopy (AFM). The surface height is in the range of 0 to 4 nm and the FWHM on the surface ranges from 40 to 60 nm. As previously reported [29], the defects below 50 nm in width on the substrate fall below the AFM detection sensitivity limit and thus have been omitted from the plot presented here.

The experiment is conducted using the SHARP tool [31], a synchrotron-based EUV microscope for photomask research located at LBNL, as shown in Fig. 2.16. Unlike most of the commercially available EUV lithography tools, The SHARP EUV microscope uses diffractive optics instead of reflective optics for its imaging lens. This enables the possibility of easily including various pupil designs for different applications [30]. Zone displacement is used to create the phase shift at the desired locations in the pupil and absorbing blocks along each zone are used to modulate the transmission efficiency thereby controlling the apodization. A detailed description of the zoneplate pattern generation algorithm is presented in Chapter 5. SEM images of the fabricated Zernike phase shift SHARP zoneplates are shown in Fig. 2.17. The quarter wavelength ($\frac{\lambda}{4}$) displacement in the zone, indicated by the dash lines in

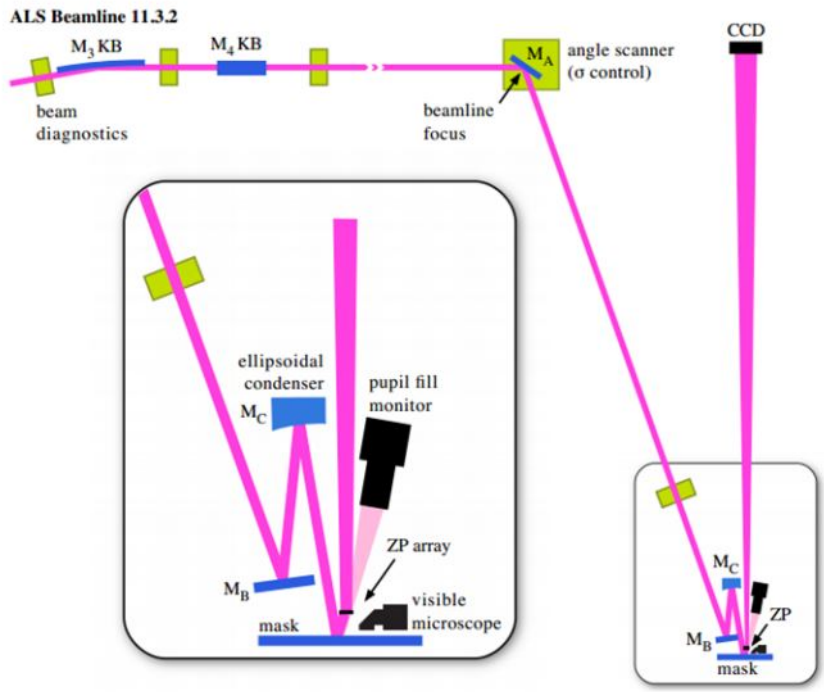

Figure 2.16: The beam path through the SHARP EUV microscope [30].

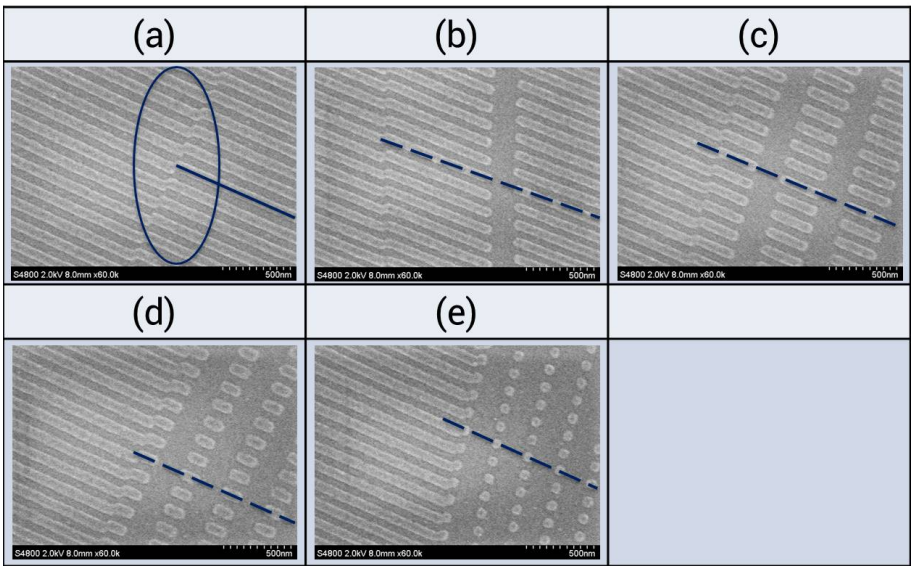

Figure 2.17: The SEM images of the off-axis Fresnel zoneplates implemented in the SHARP EUV microscope: (a) 90° phase shift and 100% transmission. (b) 90° phase shift and 69% transmission. (c) 90° phase shift and 41% transmission. (d) 90° phase shift and 20% transmission. (e) 90° phase shift and 8% transmission.

Fig. 2.17a, represents a relative 90° phase shift between these two regions in the pupil plane. The ratio of the blocks along the lines in Fig. 2.17a to Fig. 2.17e shows the intensity modulation from 100% down to 8% for Fig. 2.17e. The reported intensity transmission values are directly measured in the SHARP EUV microscope. The 4×NA of the bright field and the Zernike phase contrast zoneplates is 0.33. The illumination condition for the experiment is disk illumination with a sigma value of 0.3 or 0.5 depending on the situation. A focus range of ±5 um in 500-nm steps is used.

2.3.3 Enhanced defect SNR using the Zernike phase contrast method

Figure 2.18 shows the complex electric field amplitude and phase from the programmed defect with a width 40 nm on the substrate. The electric field is extracted from the through-focus aerial images using a phase retrieval algorithm [27]. From the complex field of the defect, the effective defect height can be recovered. With a 19° phase shift, the effective height of the 40 nm defect is 0.35 nm. It is interesting to note that this defect is not readily measurable by AFM in the presence of surface roughness. Figure 2.19 shows the measured through-focus SNR of the 40 nm defect (0.35 nm effective height) using zoneplates with phase shifts of 0° and 90°. At 0° (the conventional bright field method), the through-focus behavior qualitatively matches the expected behavior for a pure phase defect with its minimum sensitivity at best focus. On the other hand, at 90° (the Zernike phase contrast method), strong signal strength is observed at best focus with an SNR of 8. The results demonstrate the ability to control the through-focus behavior of multilayer phase defects by adding the phase shift in the pupil plane and verify the simulation results in the previous section that the Zernike phase contrast method can be used to improve inspection efficiency of the phase-dominated multilayer defects with a single scan at best focus. More importantly, an SNR ≈ 8 is achieved for a phase defect which is below the AFM noise level. This shows the importance of actinic blank inspection, which can detect a defect at EUV wavelength that cannot be identified by physically scanning the surface.

2.3.4 Change in nature of programmed defects with size and inspection implications

Figure 2.20a shows the extracted defect electric field amplitude and phase from the SHARP measurements for programmed defect widths ranging from 40 nm to 75 nm on the substrate. The electric fields show that small defects have little amplitude attenuation but the attenuation grows and thereby transmission decreases nearly linearly with size. This change in nature of the programmed defects with size can also be seen in the measured SNR through-focus behavior for particular defect sizes for bright field inspection. Specifically, Fig. 2.20b shows the defect through-focus SNR from the SHARP measurements for the 40 and 60 nm defects. The 40 nm defect has negligible absorption and the defect SNR is unacceptably

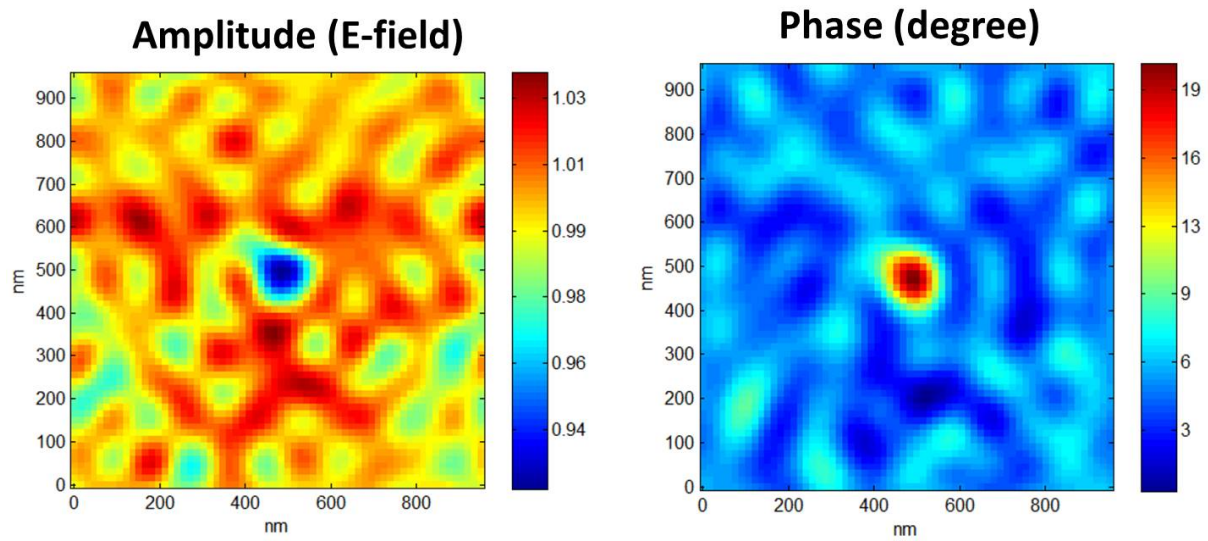

Figure 2.18: Electric field amplitude and phase extracted from through-focus defect aerial images by phase retrieval algorithm. The phase shift degree can be related to the height of the defect.

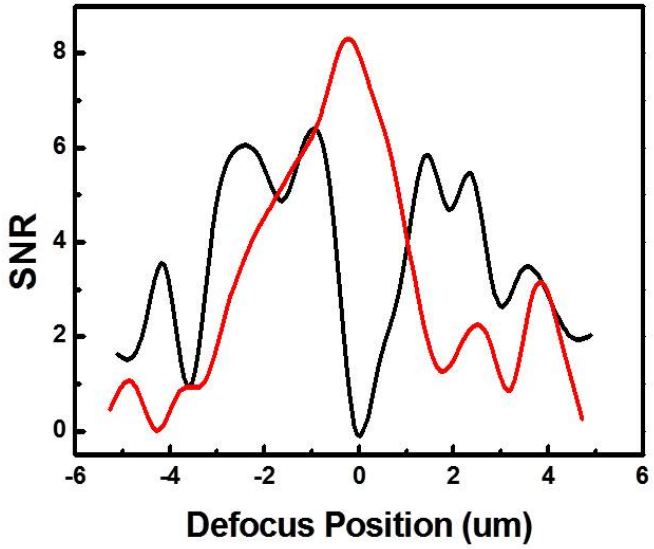

Figure 2.19: Defect SNR at different defocus positions for the 40 nm defect (0.35 nm effective height) with the conventional bright field method (Black) and the Zernike phase contrast method (Red).

low at best focus. On the other hand, the 60 nm defect has a more substantial absorption component and is detectable in focus and has its minimum SNR shifted out of focus.

The Zernike phase contrast method can manipulate the phase component of the multilayer defects to provide adequate SNR at best focus for both small and large defects. Figure 2.21 shows the comparison between the bright field method and the Zernike phase contrast method measurements from the SHARP EUV microscope for 40 nm and 60 nm defects. Both cases indicate that with the Zernike phase contrast method, the defect SNR at best focus is better than the bright field situation even for the attenuated phase defect, as shown in Fig. 2.21b. The results show that as long as the defect has a significant phase component, the Zernike phase contrast method is effective at enhancing in-focus inspection capabilities with high defect sensitivity. On the other hand, if the restriction of in-focus inspection is lifted, the Zernike phase contrast method can outperform the conventional bright field method by a higher peak SNR at optimum defocus position, as shown in Fig. 2.21b. Table 2.1 tabulates a subset of the data in focus from 40 nm to 70 nm defects by both methods, showing the impact of defect absorption on SNR improvement by the Zernike phase contrast method.

Method and Defect	**40 nm**	**50 nm**	**60 nm**	**70 nm**
Bright field	0.7	3.6	12.3	17.1
Zernike phase contrast	7.8	11.6	21	20
Ratio	11×	3.2×	1.7×	1.1×

Table 2.1: Programmed defect tabular measurements of SNR at best focus by the bright field method and the Zernike phase contrast method.

The SNR at best focus for defects with widths ranging from 40 nm to 70 nm is shown in Fig. 2.22 for the conventional bright field method and the Zernike phase contrast method. The behavior depends on the combination of defect height, width, and absorptivity. The defect height determines the optical path length which means it determines the amount of phase component of the defect. Detecting this phase with the Zernike phase contrast method gives a major improvement and provides acceptable SNR for programmed defects below 60 nm. The defect width on the surface determines the scattering angle of the defect diffraction as described in Fig. 2.10b. A narrower defect has a larger range of scattering angles and thus not all the photons can be collected by the pupil. A wider defect has a smaller range of scattering angle but more of the scattered light passes through the central phase shifted region thus the effect of phase contrast for this portion of the light can be negated. The absorption component of the defect improves the in-focus component for large defects to the point that a nearly similar and adequate SNR is obtained in focus for larger defects. The position of minimum SNR and the asymmetric peak SNR value both are strongly dependent on the absorption of the defect and, in fact, can be used to recognize the nature of the phase versus amplitude of the defect.

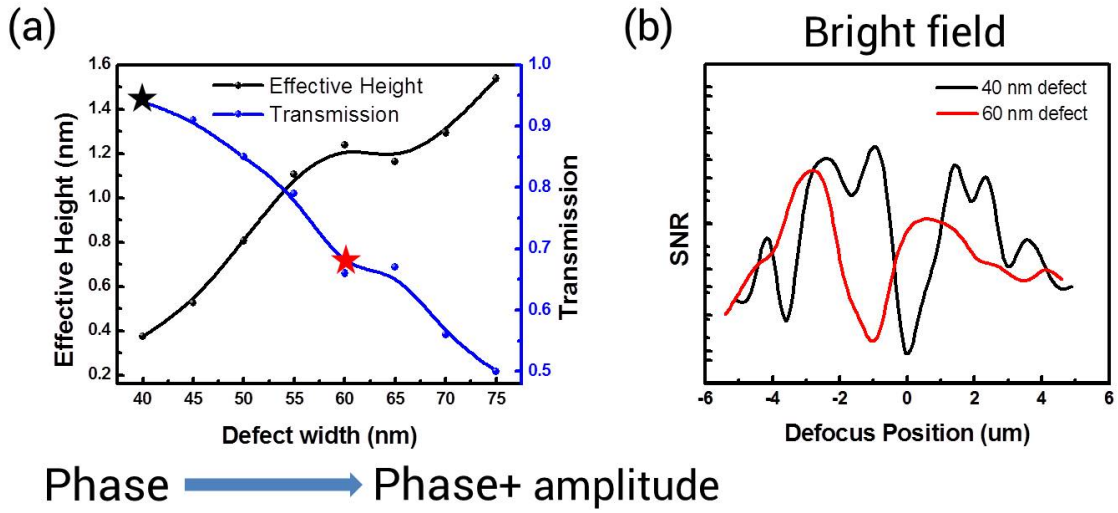

Figure 2.20: Programmed defect measurements (a) Effective height (Black) and transmission/amplitude (Blue) for programmed defects with a width ranging from 40 nm to 75 nm on the substrate. (b) Defect SNR at different defocus positions for the 40 nm defect (0.35 nm effective height, black) and the 60 nm defect (1.24 nm effective height, red) from bright field images.

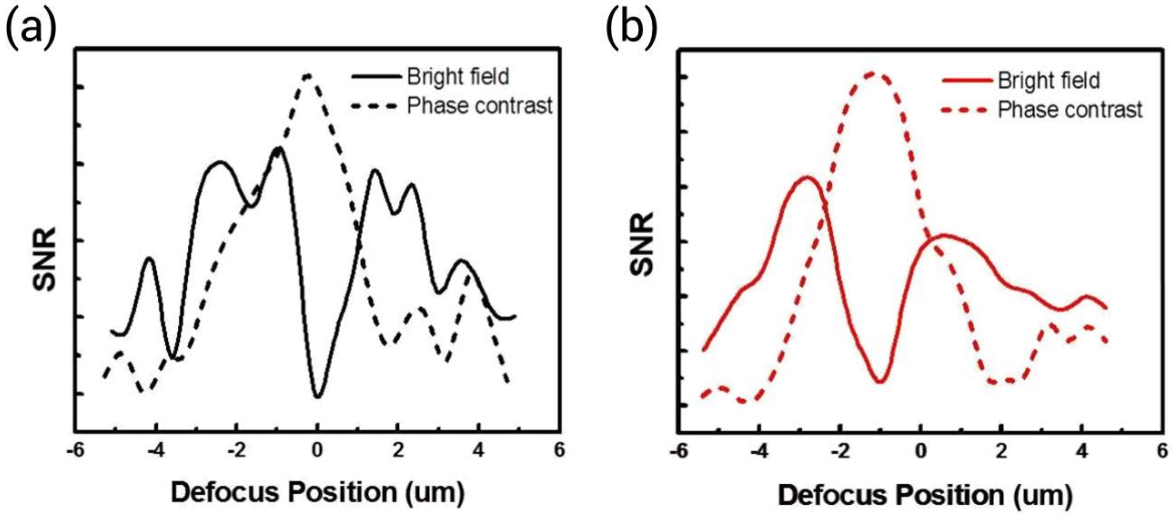

Figure 2.21: Programmed defect measurements for SNR at different defocus positions for the Zernike phase contrast method (Dash) compared to the bright field method (Solid): (a) 40 nm defect (0.35 nm effective height). (b) 60 nm defect (1.24 nm effective height).

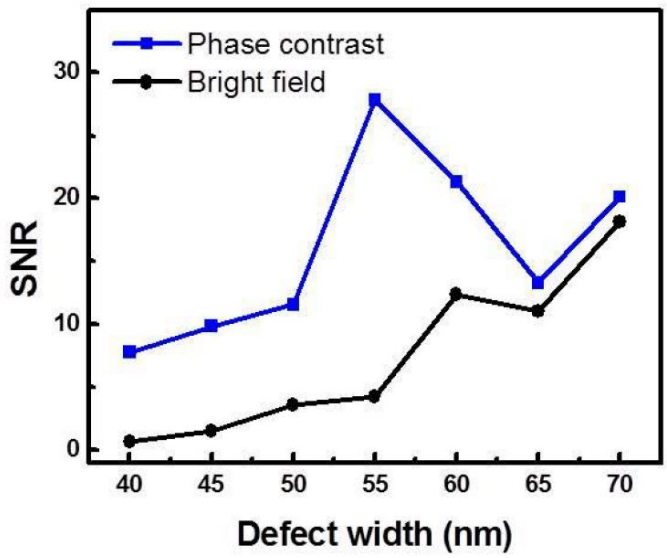

Figure 2.22: Programmed defect measurements of SNR at best focus by the bright field method (Black) and the Zernike phase contrast method (Blue) for defects with widths ranging from 40 nm to 70 nm on the substrate.

2.3.5 Impact of apodization on defect signal, noise, and defect SNR

In order to further improve the SNR, apodization is applied in the pupil to suppress the low-frequency components of the speckle noise from surface roughness while at the same time increasing the contrast of the defect image by lowering the background intensity level as discussed in the previous section. For this case, a native defect found on the mask with an effective size of 1.23 nm $\times$ 120 nm is used. The effective size is extracted using a phase retrieval method [27] and is shown in Fig. 2.23. Five different apodization intensity transmission values are examined: 100%, 69%, 41%, 20%, and 8% for the 90° Zernike phase shift case and are compared with the conventional bright field result. The illumination for this set of data is a disk with a sigma value of 0.5.

Figure 2.24 shows the list of the aerial images of the native defect at different defocus positions using different zoneplates on the SHARP EUV microscope. The background intensity is normalized to a clear field value of unity in order to compare the defect signal in these different situations. The defect intensity from the conventional bright field method (0°/100%) nearly disappears at best focus, while the results for the Zernike phase contrast method (90°/100%) has peak sensitivity at best focus as expected. Moreover, as the background intensity transmission value is lowered to 8%, the defect signal strongly increases to nearly 3.5$\times$ the background level, but the speckle noise from the substrate phase roughness is also observed to increase.

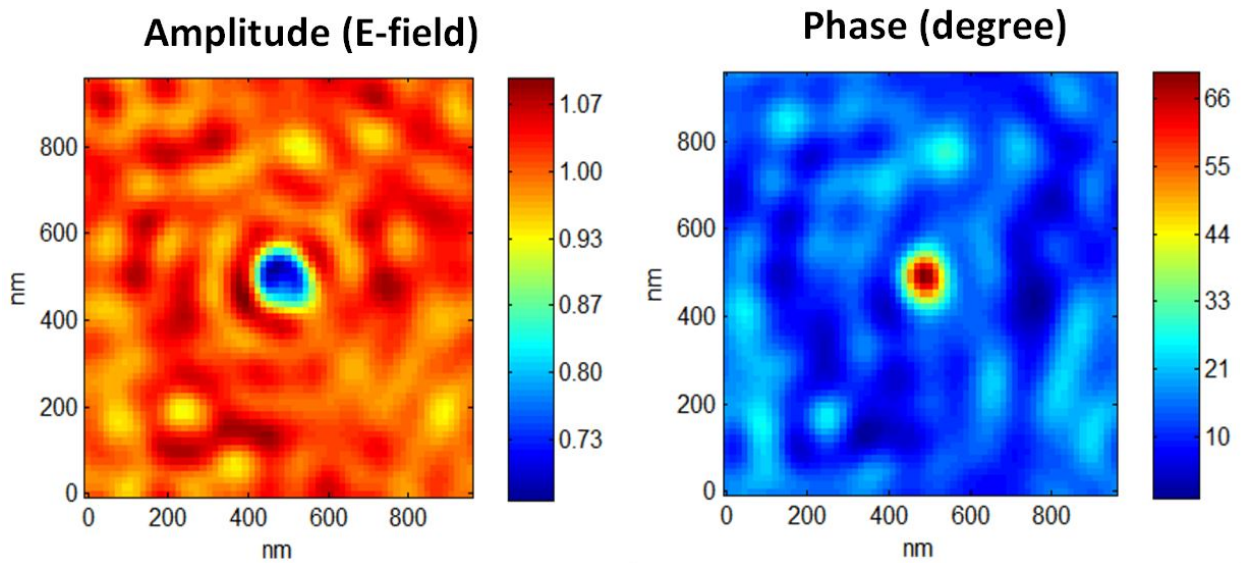

Figure 2.23: Electric field amplitude and phase for a native defect extracted from through-focus aerial images using the phase recovery algorithm. The effective height is 1.23 nm based on the phase of the defect.

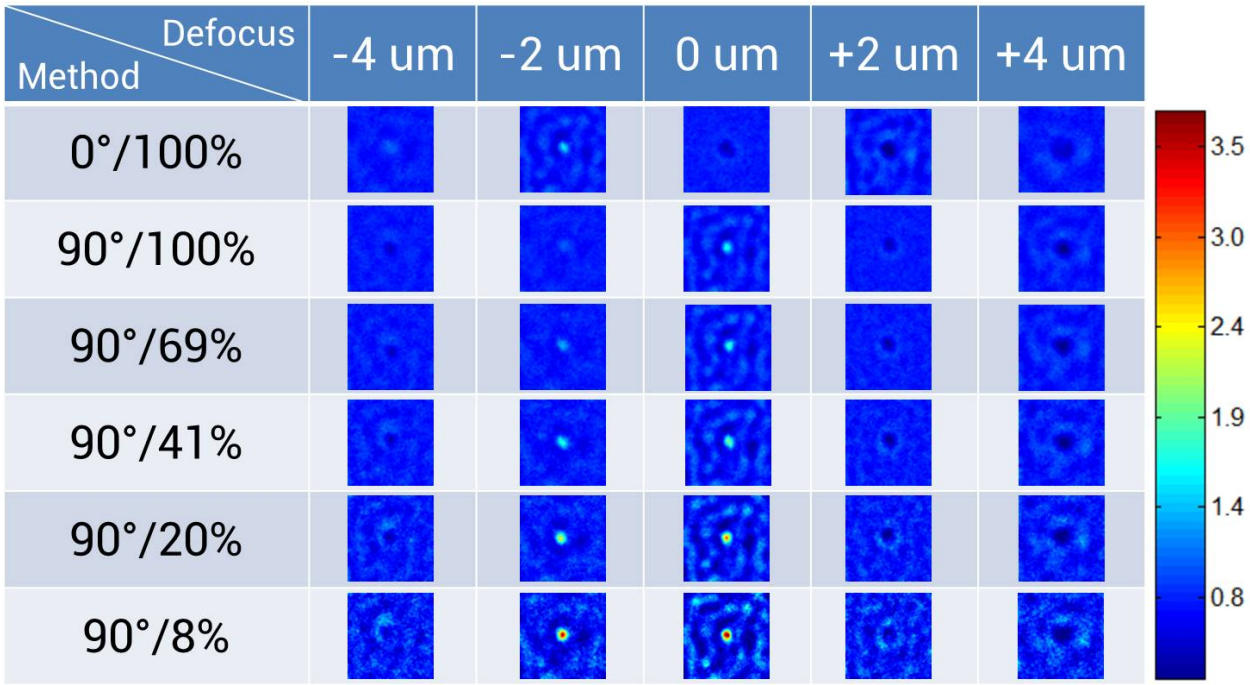

Figure 2.24: Aerial images from the SHARP EUV microscope for a native defect (1.23 nm effective height) at different defocus positions under different pupil designs. The effective height is 1.23 nm based on the phase of the defect.

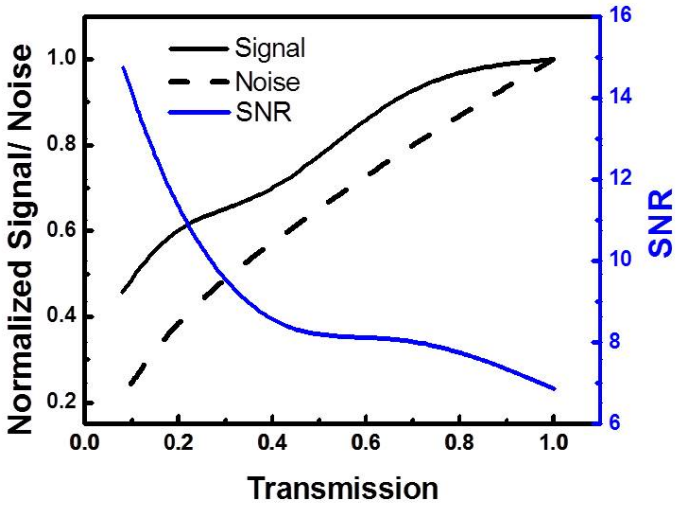

Figure 2.25: Defect signal (Black, solid), noise (Black, dash), and defect SNR (Blue, solid) for a native defect (1.23 nm effective height) as measured on the SHARP EUV microscope at best focus under different transmission of the 0.5 sigma apodization in the phase shifted region.

The change in the defect signal and speckle noise versus apodization levels as measured on the SHARP EUV microscope is shown in Fig. 2.25. The vertical axis on the left is used for both signal and noise. It is normalized to the value for the 100% transmission and a 90° phase shift case without normalizing to their individual background levels. Both signal and noise start from 1 at the transmission of 1. As expected, the normalized signal decreases with a decrease in the transmission (stronger apodization). There are two important observations. The first observation is that although the signal decreases with decreasing transmission, the rate of decrease is quite low. The signal level is still 43% when the transmission apodization is only 8%. This is due to most of the scattered light from the defect falling in the unattenuated region between the central apodization and the edge of the pupil. The second important observation is that the noise is decreasing faster than the signal with a decrease in the transmission. This is because most of the diffracted light from the phase noise roughness is scattered at low angles that fall within the apodized pupil region. The speckle noise is decreased by a factor of 2 more than the defect signal and results in doubling the defect SNR from 7 to 14 at an apodization transmission of 8%.

2.4 Phase defect inspection efficiency comparison between the Zernike phase contrast method and the dark field method

In the previous sections, the simulation and experimental results show the advantages of the Zernike phase contrast method over the conventional bright field method on phase defect inspection. In this section, comparison between the Zernike phase contrast method and the dark field method on the phase defect inspection efficiency is presented. The impacts of defect type, resolution, and photon density on both methods' inspection efficiency are discussed respectively. Moreover, the photon shot noise and the camera noise are included in the SNR calculation, instead of a simplified constant system noise assumption used in the previous sections. In the end, the pupil design matrix study shows the phase defect SNR performance under various phase shifts and apodization conditions.

2.4.1 Simulation settings and parameters

The simulation study uses a thin mask 2D model to generate the EUV (13.5 nm) images. To model the defect, Gaussian-shaped phase defects height or depth are 1 nm and their FWHM are 60 nm are used [9]. The mask roughness is assumed to be 60 pm with a correlation length $\approx$ 100 nm [24, 25]. The defect and mask roughness images are simulated independently to account for the impact of defect signal and speckle noise. Since a defect can be viewed simply as an extreme event in the mask roughness height distribution, the defect height profile is not directly added to the mask roughness height profile.

For the imaging conditions, an outer NA of 0.2 and inner NA (central obscuration) of 0.1 and a disk illumination NA of 0.1 are used as described in Ref. [26]. In order to include phase shift and apodization in the discussion, the pupil functions with phase shifts ranging from 0° to +180° whose shape is matched to the disk illumination is used. Apodization is defined as the electric field transmission of the background level of the pupil function, ranging from 10% $\sim$ 100%. Moreover, to account for the impact of photon levels and pixel size, 1 photon/nm^2 is used as the bright field level photon density.

To get a better understanding of defect SNR performance, the system noise sources are divided into photon shot noise induced by defect signal and background intensity, and a camera noise from the dark current of the CCD camera, thus Eq. 2.2 is redefined as:

$$\text{Defect SNR} = \frac{\text{Defect Signal}}{\text{Speckle Noise} + \text{Photon Shot Noise} + \text{Camera Noise}} \tag{2.3}$$

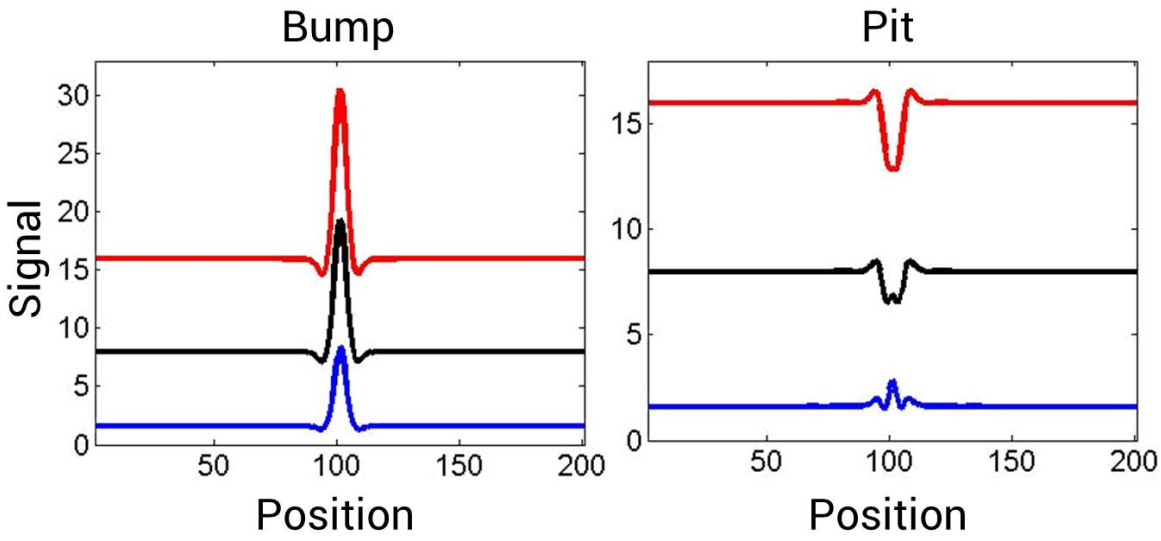

Figure 2.26: Defect Signal for bump and pit under different apodization conditions: 10% (Blue), 50% (Black), and 100% (Red) background transmission. The defect signal doesn't include pixel size into consideration.

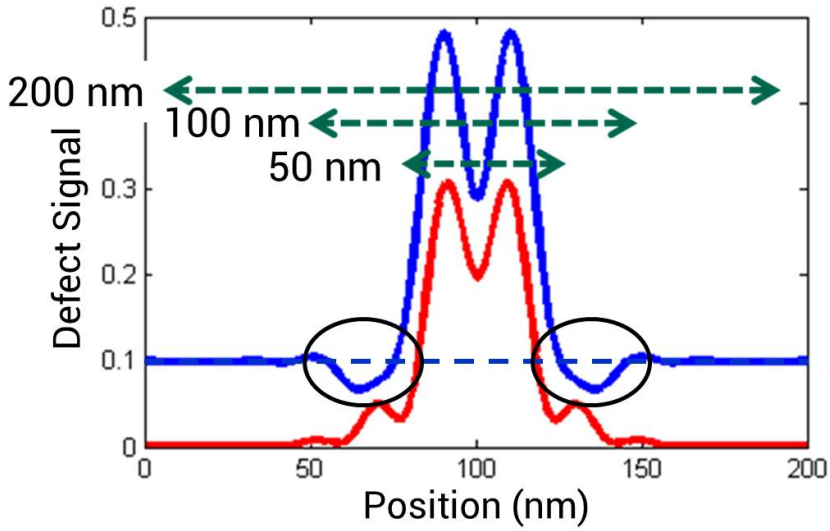

Figure 2.27: Defect Signal for bump defect under 10% (Blue) background transmission by the Zernike phase contrast method, and the dark field method (Red). The defect signal image doesn't include pixel size into consideration.

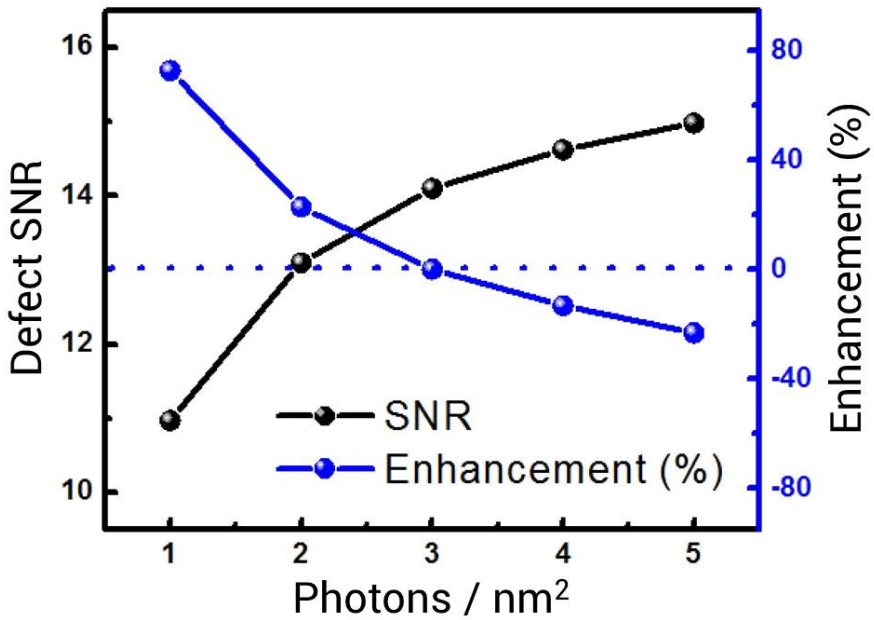

Figure 2.28: Defect SNR (Black) by the Zernike phase contrast method with 10% background transmission at different photon levels. The enhancement (Blue) is the defect SNR ratio between the Zernike phase contrast method and the dark field method. Enhancement > 0 means the Zernike phase contrast method has better defect SNR. Pixel size: $25 \times 25\ nm^2$.

2.4.2 Impact of defect type, resolution, and photon level on defect SNR by the dark field method and the Zernike phase contrast method

Figure 2.26 shows the impact of apodization on different defect types. Even though the apodization can reduce the background intensity level to improve the image contrast and suppress the speckle noise by filtering its low-frequency component, the bump and pit phase defects have different results. Bump defect has better image contrast while the pit defect signal saturates at one point and the peak signal switches sign as the apodization increases. The reason is, under same phase shift condition (+90°), a bump defect experiences constructive interference and has a peak signal larger than the background level, while a pit defect experiences destructive interference and has a peak signal lower than the background level. Therefore, pit defect signal saturates at the bottom of the bright field level and switches sign as the apodization increases, since the intensity always has to be positive. The results indicate that to detect both types of phase defects using the Zernike phase contrast method, apodization should not be applied to the pupil design.

Pixel size is another important factor in inspection efficiency calculation. Smaller pixel

size gives a better image resolution on the mask, thus has higher detection sensitivity. Larger pixel size reduces the inspection time under fixed scanning speed, thus improves the throughput of the inspection system. Figure 2.27 shows the sub-resolution image (pixel size = 1 nm/pixel) by the Zernike phase contrast method and the dark field method. For the defect signal obtained by using the Zernike phase contrast method, the side lobes of the defect signal can cancel out the peak signal enhancement, depending on the pixel size. At smaller pixel size, the side lobe is not included and results in a higher defect signal. At larger pixel size, the side lobes below the bright field level are included in the same pixel and compensate the enhancement on peak defect signal, thus resulting in a smaller defect signal. For the defect signal by the dark field method, a similar situation does not exist since the background intensity is 0. Therefore, the defect signal increases accordingly with an increase in the pixel size. The results shown here indicate that the advantage of defect signal strength by the Zernike phase contrast method over the dark field method is pixel size dependent.

The photon density (source power) impacts the defect SNR enhancement as well. As shown in Fig. 2.28, even though larger photon density increases the defect SNR by using the Zernike phase contrast method, the enhancement is smaller compared with the dark field method. This is due to the increasing photon shot noise from the background intensity with an increase in photon density for the Zernike phase contrast method. Therefore, the Zernike phase contrast method with 10% background transmission only has better defect SNR performance than the dark field method when the photon level is ≤ 2 photons/nm^2. As the photon level increases, the dark field method shows better defect detection sensitivity.

2.4.3 Matrix study on the defect SNR performance under different pixel sizes, phase shifts, and apodization conditions

Systematic study of pupil design and pixel size shows the inspection efficiency comparison between the Zernike phase contrast method and the dark field method in Fig. 2.29. Ratio > 1 indicates the Zernike phase contrast method has better performance. Each plot contains 9 different pixel size settings from 10 nm to 500 nm. Each pixel size settings has various phase shifts and apodization conditions. The x-axis shows different phase shifts in the pupil plane, ranging from 0° to 180°. The y-axis shows different background transmission, ranging from 10% to 100%.

As discussed in the previous section, Figure 2.29 shows that the Zernike phase contrast method can have better phase defect detection sensitivity over the dark field method when the pixel size $\leq 25nm$, and roughly a 90° phase shift without apodization in the pupil plane. Moreover, since the bump and pit defects experience different types of interference under the same phase shift condition, the detection sensitivity is different for them even under the same pupil and pixel size condition. The result shown here indicates that the dark field method is the better configuration since it can operate at larger pixel size with high defect SNR on both types of phase defects from inspection efficiency perspective.

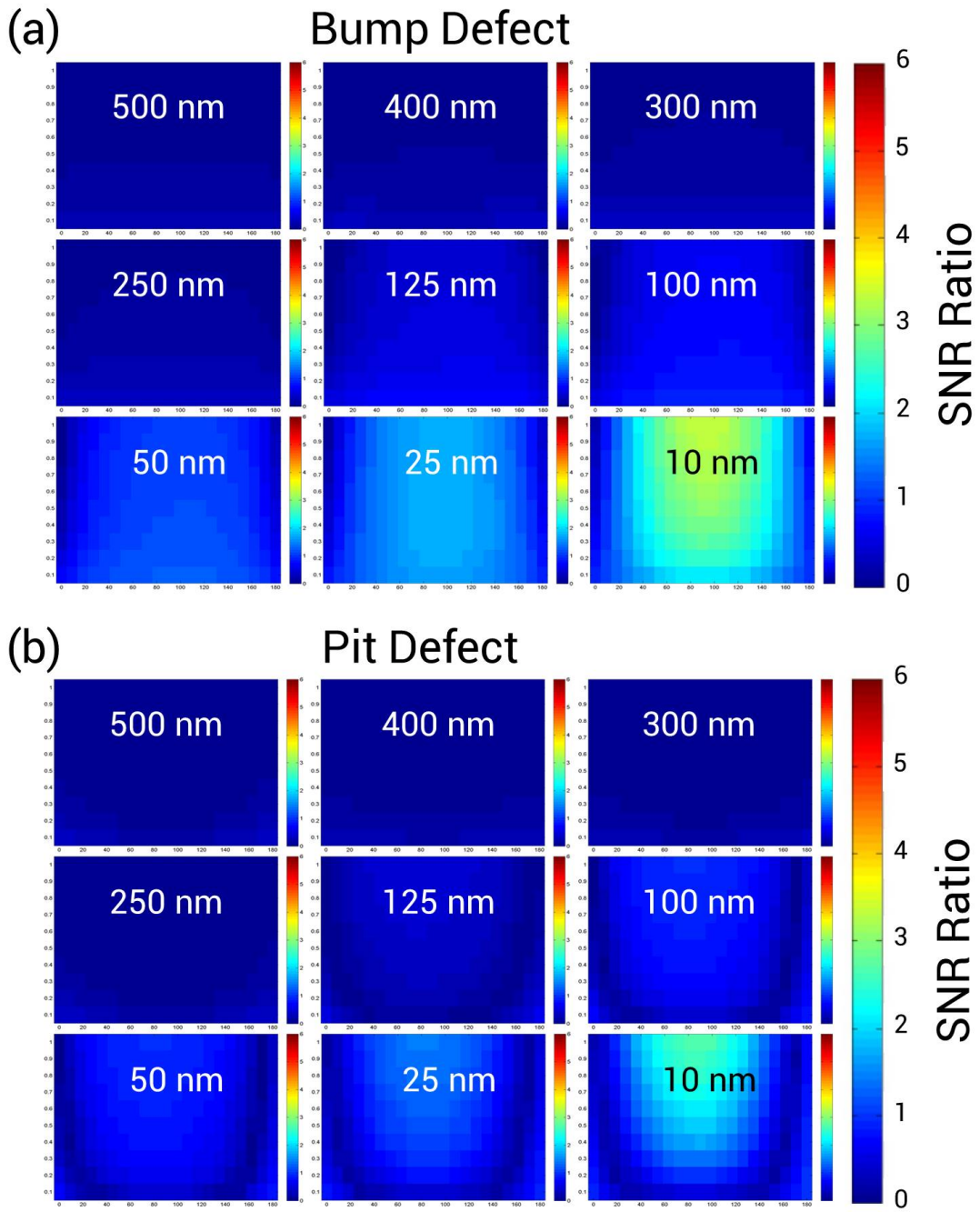

Figure 2.29: Defect SNR for (a) Bump and (b) Pit defect under different pixel sizes. The ratio is defined as the defect SNR by the Zernike phase contrast method over the dark field method. Ratio > 1 means the Zernike phase contrast method has better defect SNR. X-axis: phase shifts in the pupil plane ($0° \sim 180°$). Y-axis: apodization conditions ($10\% \sim 100\%$ background transmission).

2.5 Impact of tool design on defect detection sensitivity for a dark field based actinic blank inspection tool

Nearly defect-free mask blanks, and thus high sensitivity defect detection, are crucial to the commercial viability of EUV lithography. In addition to high sensitivity, high throughput is also critical to mask blank inspection. Here the design study exploring the design tradeoff for an actinic blank inspection tool is reported.

In the previous section, the dark field configuration was found to be the most effective method to get the best overall defect detection sensitivity on a range of defect types. Therefore, the dark field configuration is used to study the impact of tool design choices in 3 categories: pixel size, EUV source type, and photon collection efficiency.

First, this section examines the impact of pixel size on the relationship between signal and noise. Situations in which different noise sources dominate such as speckle noise or photon shot noise can result in different optical designs to maximize the defect SNR. Next, the impact of EUV source type on the choice of optics NA and illumination condition is discussed. The results show that increased photon density can compensate for the loss of the defect signal at larger partial coherent illumination for plasma-discharged sources, thus larger partial coherent illumination is the preferred setting. The impact of photon collection efficiency is also discussed by varying the outer NA or increasing photon density, showing that the impact of outer NA is pixel size dependent and increasing photon density cannot always result in higher defect SNR.

2.5.1 Simulation settings and parameters

In this section, a thin mask 2D model is used to generate the EUV (13.5 nm) images. The defect and mask roughness images are simulated independently to account for the impact of defect signal and speckle noise respectively. Since a defect can be viewed simply as an extreme event in the mask roughness height distribution, the defect height profile is not directly added to the mask roughness height profile. The data process flow is shown in Fig. 2.30 and also described in Ref. [32]. First, pixel-binning of the densely-sampled aerial image is utilized to mimic the results under different inspection pixel sizes for both defect and surface roughness images. Then the simulated detected image intensity is scaled in photons based on the illumination settings. Finally, the defect signal and the speckle noise can be calculated from these images, and the SNR is computed, as shown in Eq. 2.4.

$$\text{Defect SNR} = \frac{\text{Defect Signal}}{\text{Speckle Noise} + \text{Photon Shot Noise} + \text{Camera Noise}} \tag{2.4}$$

As shown in Fig. 2.31a, Gaussian-shaped phase defects with height either 0.5 nm or 1 nm and an 60 nm FWHM are used based on the typical results describe in Ref. [9]. For speckle, the mask roughness is assumed to be 60 pm which is within the range (50 $\sim$ 70

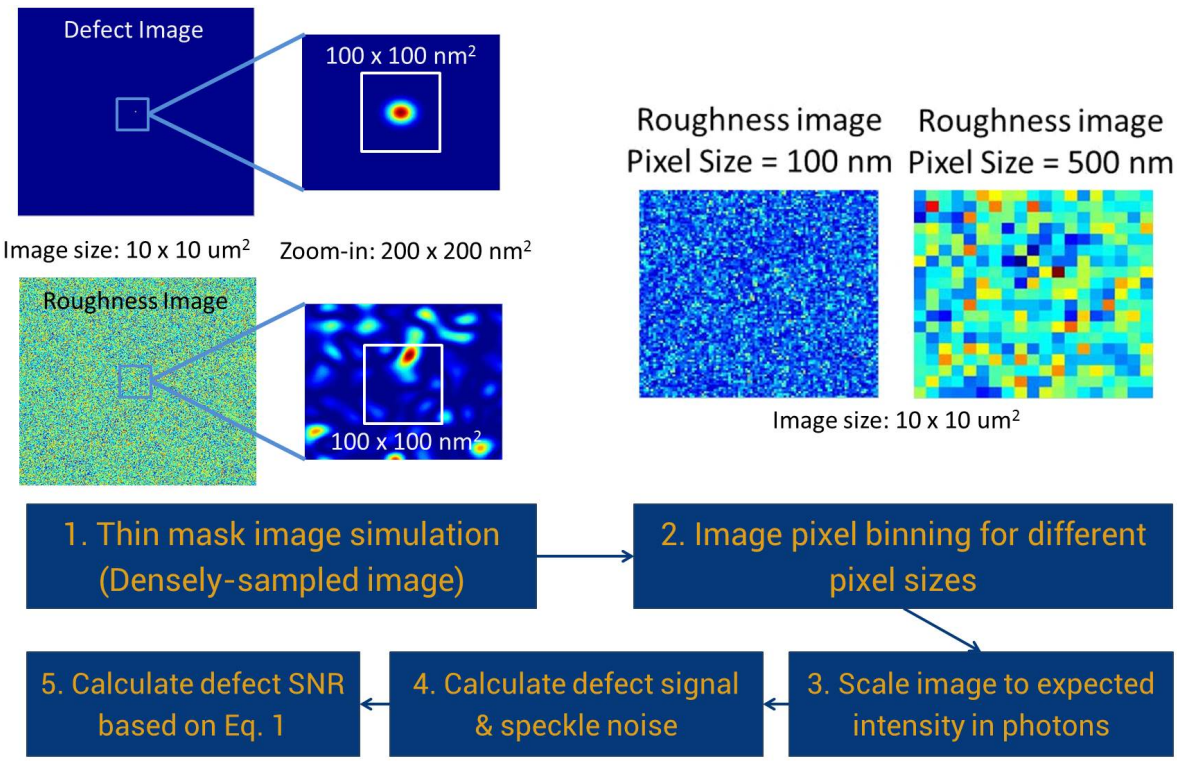

Figure 2.30: Data process flow. Images shown in this figure are in the dark field imaging mode. Images physical size: 10×10 um^2 (zoom-in images physical size: 200×200 nm^2). Roughness image in raw image section is in log-scale to improve the visibility. The rest of the images are in linear scale. Binned defect images are not shown in the figure since the defect intensity distribution is smaller than the pixel size and thus the ideal binned defect image contains only a single bright pixel in an otherwise completely dark field.

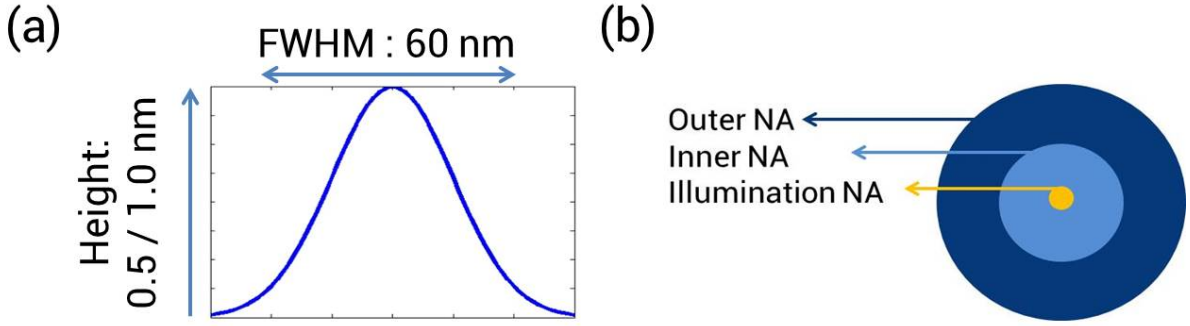

Figure 2.31: (a) Defect information. (b) Optics and illumination definition.

pm) for a typical high-quality EUV mask blank [24], and the correlation length of the mask roughness is $\approx$ 100 nm based on experimental results [25]. For the imaging conditions, a dark field configuration is assumed as described in Ref. [26] with an outer NA of 0.15 to 0.5, inner NA (central obscuration) of 0.025 to 0.25 and a disk illumination NA of 0.01 to 0.25 are used, as shown in Fig. 2.31b. For the detector conditions and photon densities, the pixel size is in the range of 100 nm to 500 nm in mask scale, and the photon level on the mask is $0.1 \sim 62.5$ photons/nm^2. the actual number of photons per pixel detected at the CCD camera is also noted to be only $1\% \sim 5\%$ of the bright field level due to the dark field configuration, the EUV mirror loss, and the CCD camera efficiency. To consider the impact of different source types in the following discussion, the DPP (Discharge produced plasma) / LDP (Laser-assisted discharge plasma) sources are assumed to have a varied photon density depending on illumination NA, while the compact synchrotron or free electron laser sources are assumed to have a fixed photon density as a function of illumination NA [33, 34, 35]. Schematic diagrams of the sources are shown in Fig. 2.31. Equation 2.4 defines the defect SNR used in the following discussion.

2.5.2 Impact of pixel size on defect SNR

Pixel size determines the image resolution and also the inspection efficiency. Pixel size depends on both CCD camera pixel size and magnification of the optical system. The impact of pixel size on the defect signal and the noise under fixed optics and illumination setting is shown in Fig. 2.32. As pixel size increases, more photons per pixel results in larger signal and noise. A 30% signal strength enhancement is achieved while the noise is increased by 300% when the pixel size is increased from 100 nm to 500 nm. This is due to the size of the target defect image being smaller than the smallest considered pixel size, thus further increasing the pixel size has a minor impact on signal strength compare to speckle noise. Moreover, the relationship between speckle noise and signal shot noise varies as well. As shown in Fig. 2.32b, the signal shot noise is the dominant noise source at smaller pixel size, meaning that the defect SNR can be improved by the larger signal strength coming from increased photon density. On the other hand, the speckle noise is the dominant noise source at larger pixel sizes meaning that the signal and noise increase simultaneously with an increase in photon density. Figure 2.32c shows the defect SNR comparison between various pixel sizes for different optical configurations. The results indicate that compared with the NA of the optical system, the pixel size is the dominant factor on defect SNR performance. The results shown here indicate that there is a trade-off between inspection efficiency and defect detection sensitivity. Larger pixel size can scan the mask blank faster than the smaller pixel size configuration, but the defect sensitivity is also lower than the smaller pixel size configuration .

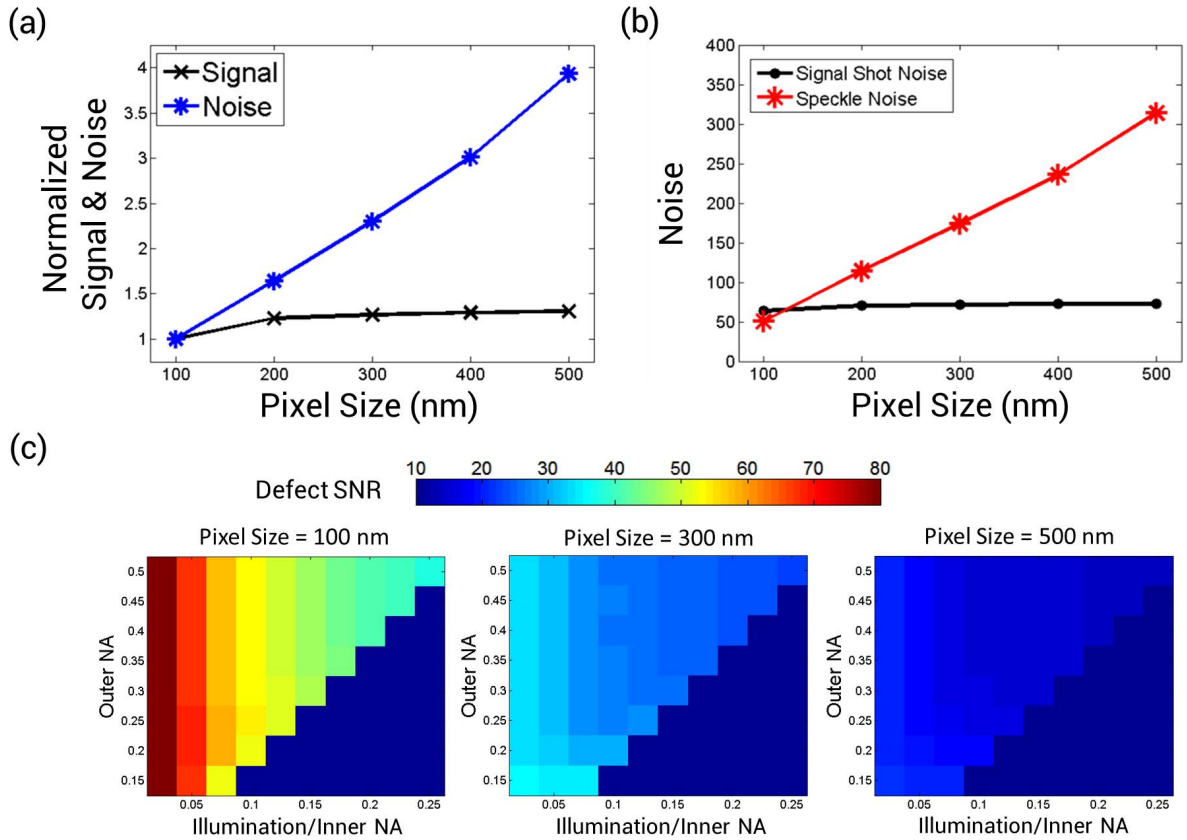

Figure 2.32: (a) Normalized defect signal (Black) and noise (Blue) under various pixel sizes, relative to the value at 100 nm pixel size. Noise includes signal shot noise, speckle noise, and camera noise. Photon density: 5.6 photons/nm^2. Pixel size: 100 $\sim$ 500 nm. Outer NA / Inner NA / Illumination NA: 0.25 / 0.075 / 0.075. (b) The impact of pixel size on different noise sources. Signal shot noise (Black) and speckle noise (Red). Photon density: 5.6 photons/nm^2. Pixel size: 100 $\sim$ 500 nm. Outer NA / Inner NA / Illumination NA: 0.25 / 0.075 / 0.075. (c) Defect SNR under various pixel sizes at different optical NA configurations. Photon density: 10 photons/nm^2. Pixel size: 100 $\sim$ 500 nm. Defect and roughness used in this figure: Height = 1 nm, FWHM = 60 nm. Mask roughness: 60 pm.

2.5.3 Impact of source type on defect SNR

The relationship between partial coherence and collected source power depends on the EUV source type. Synchrotron type sources allow a new degree of freedom in that the partial coherence can be adjusted independently of the collected source power. This can be achieved, for example, using a scanning mirror to create arbitrary pupil-fill patterns from the coherent beam while maintaining the photon density [31]. On the other hand, for plasma-discharge sources like LDP or DPP, larger illumination NA increases the partial coherence and at the same time increased the photon density.

Figure 2.33a shows the impact of larger illumination NA and photon density on defect signal strength for LDP / DPP sources. The results indicate that larger partially coherent illumination actually improves the defect signal strength by compensating for the loss of defect signal from increasing photon density. Therefore, in the signal shot noise dominated situation, different source types need different illumination settings to reach optimum defect SNR. As shown in Fig. 2.33b, larger partial coherent illumination results in better defect SNR for discharge type sources, while coherent illumination results in higher defect SNR for synchrotron type sources.

In the dark field configuration, the relationship between illumination NA and inner NA (central obscuration) determines the defect signal strength and thereby the overall defect SNR. Figure 2.34a shows the impact of the mismatch between illumination and inner NA on defect signal strength, the defect signal using coherent illumination is down to 0.5% of the reference value at illumination NA = 0.25 when the optical system is using an inner NA = 0.25. Therefore, the illumination NA has to match the inner NA (central obscuration) to maximize the defect SNR, as shown in Fig. 2.34.

2.5.4 Impact of photon collection efficiency on defect SNR

With larger outer NA, more scattered light can be collected by the inspection system, but this does not necessarily translate to a higher defect SNR. Figure 2.35a shows the trend of signal and noise as a function of pixel size as the outer NA increases. At pixel size = 100 nm, which is roughly the size of the defect image, increasing the outer NA initially increases the signal faster than the noise thereby resulting in higher SNR, but the defect SNR improvement saturates as the outer NA exceeds 0.3. On the other hand, at pixel size = 500 nm, larger outer NA increases the noise faster than the defect signal thereby resulting in lower defect SNR, but the impact on defect SNR also saturates as the outer NA surpasses 0.3. Figure 2.35b shows the impact of outer NA on various noise sources under different pixel sizes. At pixel size = 100 nm, signal shot noise is slightly larger than the speckle noise and both noise sources have a similar trend as outer NA increases. At pixel size = 500 nm, speckle noise is the dominant noise source and therefore determines the trend for the noise shown in Fig. 2.35a. The results here indicate that as pixel size varies, the relationship between various noise sources varies as well which results in different responses as the outer NA increases. Also, based on the frequency distribution of the mask roughness and the defect shape, outer

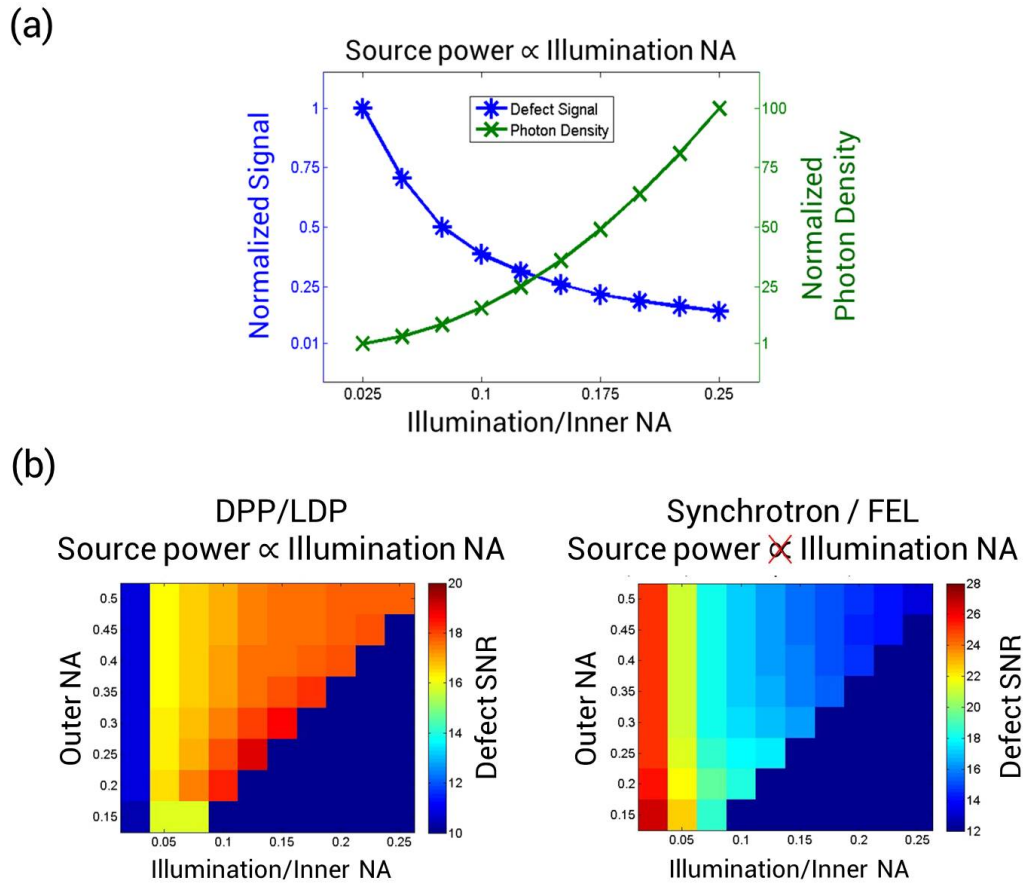

Figure 2.33: (a) The impact of illumination NA on signal strength (Blue) and photon density (Green) for a plasma source. The signal is normalized relative to the value at illumination NA = 0.025. Defect size: Height = 1 nm, FWHM = 60 nm. Pixel size: 100 nm. Outer NA: 0.5. Inner NA is the same as illumination NA for this plot. (b) Defect SNR at different optical NA configurations and source types. Defect size: Height = 0.5 nm, FWHM = 60 nm. Mask roughness: 60 pm. Photon density: 0.1 $\sim$ 62.5 photons/nm^2 for DPP / LDP source (10 photons/nm^2 at illumination NA / inner NA = 0.1). 10 photons/nm^2 for synchrotron / FEL source. Pixel size: 100 nm.

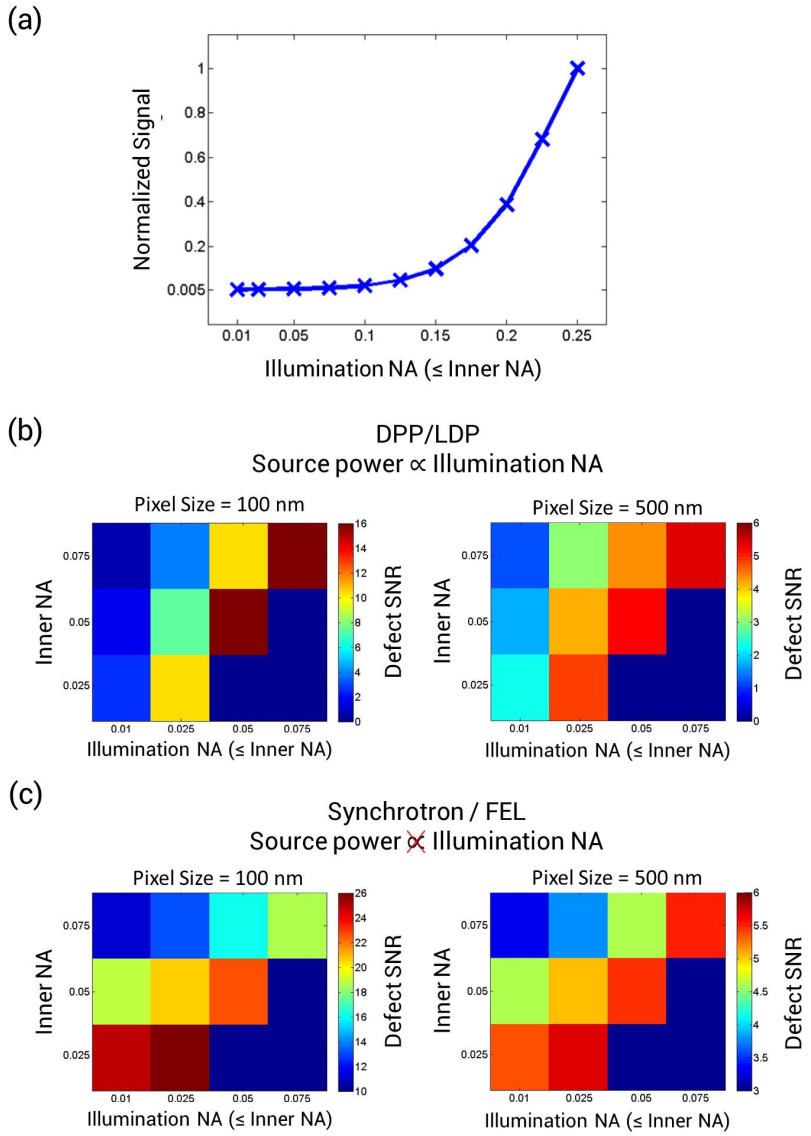

Figure 2.34: (a) The impact of illumination NA on defect signal under fixed inner NA (central obscuration). Defect size: Height = 1 nm, FWHM = 60 nm. Pixel size: 100 nm. Outer NA / Inner NA: 0.5 / 0.25. (b) Defect SNR under various illumination NA and inner NA (central obscuration) conditions using DPP / LDP source. Defect size: Height = 0.5 nm, FWHM = 60 nm. Mask roughness: 60 pm. Photon density: 0.1 $\sim$ 5.6 photons/nm^2 (10 photons/nm^2 at illumination NA / inner NA = 0.1). Pixel size: 100 and 500 nm. Outer NA: 0.15. (c) Defect SNR under various illumination NA and inner NA (central obscuration) conditions using synchrotron / FEL sources. Defect size: Height = 0.5 nm, FWHM = 60 nm. Mask roughness: 60 pm. Photon density: 10 photons/nm^2. Pixel size: 100 and 500 nm. Outer NA: 0.15.

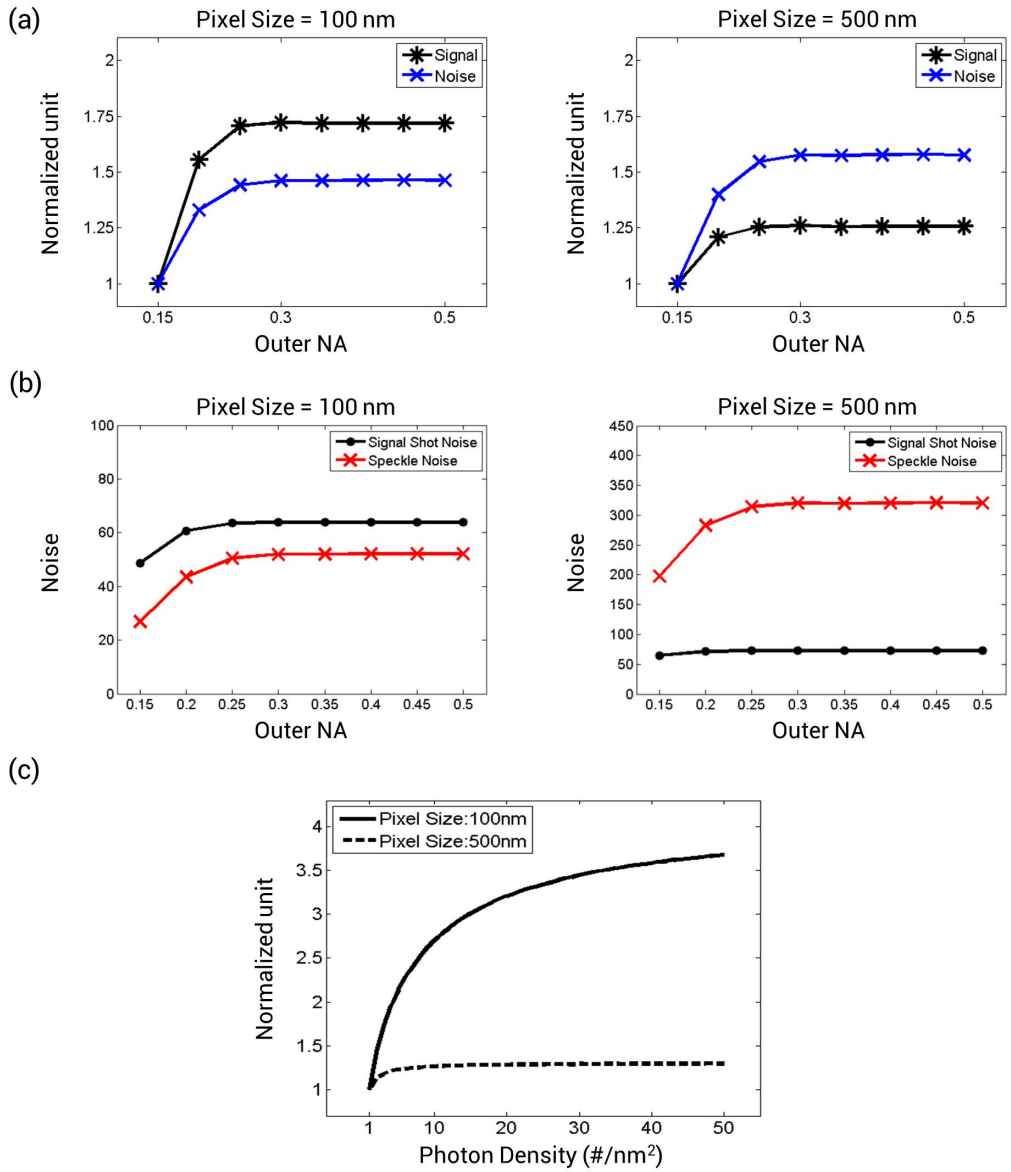

Figure 2.35: (a) Normalized defect signal (Black) and noise (Blue) under various outer NA, relative to the value of NA = 0.15. Noise includes signal shot noise, speckle noise, and camera noise. Photon density: 5.6 photons/nm^2. Pixel size: 100 and 500 nm. Inner NA / Illumination NA: 0.075 / 0.075. (b) The impact of outer NA on signal shot noise (Black) and speckle noise (Red). Photon density: 5.6 photons/nm^2. Pixel size: 100 and 500 nm. Inner NA / Illumination NA: 0.075 / 0.075. (c) The impact of photon density on defect SNR under fixed optical and illumination configurations. Pixel size: 100 nm (Solid curve) and 500 nm (dash curve). Outer NA / Inner NA / Illumination NA: 0.25 / 0.1 / 0.1. Defect and roughness used in this figure: Height = 1 nm, FWHM = 60 nm. Mask roughness: 60 pm.

NA beyond 0.3 does not have a significant impact on defect SNR performance. Therefore, in order to improve the defect SNR performance, using high NA optics to improve the photon collection efficiency is not very effective for an actinic blank inspection tool.

To improve the defect detection sensitivity of an existing blank inspection tool, upgrading the source power might be a cost-effective approach compared to modifying the optical imaging system. Figure 2.35c shows the impact of photon density on defect SNR under fixed optical NA configuration. At pixel size = 500 nm, the improvement saturates at less than 5 photons/nm^2 with a maximum 30% SNR improvement. At pixel size = 100 nm, the defect SNR improvement saturates at around 40 photons/nm^2 with a maximum 270% enhancement. The difference is due to the relationship between various noise sources, as shown in Fig. 2.32b. However, when the speckle noise becomes the dominant noise source as photon density increases, defect SNR saturates for both pixel size conditions. The result shown here indicates that simply improving the EUV source power (photon density) does not necessarily lead to better SNR.

2.5.5 How to improve the defect SNR by varying pixel size and source power under fixed optical configuration

As the technology node advances, the requirement on EUV mask blank defectivity naturally tightens. In this section, the possibility of improving the critical defect SNR by upgrading the source power or changing the pixel size under a fixed tool optical configuration is discussed.

The outer NA, inner NA, and illumination NA used in this section are 0.25, 0.1, and 0.1 respectively. The critical defect sizes are 0.5 and 1.0 nm in height, with 1.0 nm representing the initial EUV technology node requirement and 0.5 nm representing the expected next generation node requirement. In both cases, a defect width of 60 nm is assumed [9]. The mask roughness is assumed to be 60 pm with a correlation length $\approx$ 100 nm [24, 25]. The threshold defect SNR is set to 15 for the critical defects to ensure a high capture rate.

Figure 2.36 shows the defect SNR for both critical defects under various photon densities and pixel sizes. As discussed in the previous sections, pixel size has the dominant impact on defect SNR while the impact of photon density saturates in the 5 to 10 photons/nm^2 range. For a 1.0 nm height defect, a pixel size of approximately 500 nm and a photon density near 2 photons/nm^2 is sufficient to reach the target SNR value. However, for a 0.5 nm defect, the pixel size must be reduced to 100 nm and the photon density increased to 4 photons/nm^2 to reach the target. The results also indicate that with a 500 nm pixel size, increasing photon density does not improve the defect SNR for the 0.5 nm defect. As explained in the previous section, this is a result of the defect SNR saturating at higher photon densities due to the speckle noise increasing along with the defect signal.

Figure 2.37 shows the list of the required source power for actinic blank inspection to reach the desired defect SNR in the same inspection time for the two different critical defect sizes. Here the 1.0 nm defect is used as the reference case. The effective source power in the illumination cone and the DPP source power in 2π sr (solid angle) are calculated based

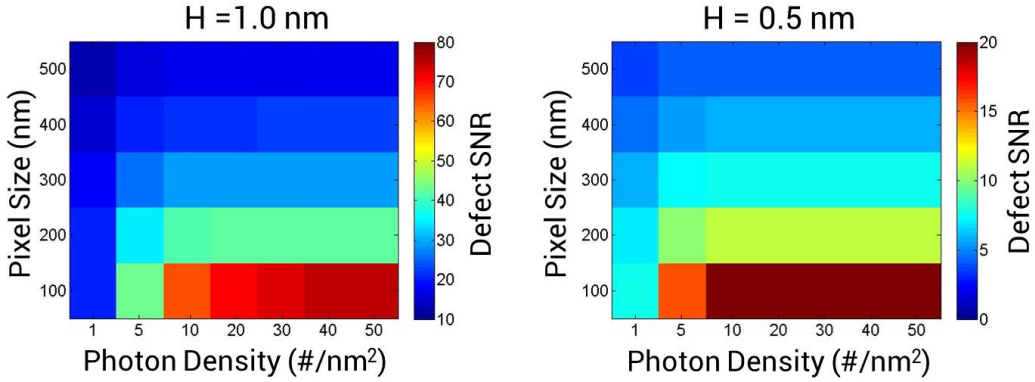

Required pixel size & photon density to reach SNR ≥ 15		
Defect Height (nm)	Pixel Size (nm)	Photon Density (#/nm²)
1.0 (ref.)	**500**	**2**
0.5 (target)	**100**	**4**

Figure 2.36: Critical defects SNR at best focus under various pixel sizes and photon densities. Defect size: Height = 0.5 and 1 nm, FWHM = 60 nm. Outer NA / Inner NA / Illumination NA: 0.25 / 0.1 / 0.1. Photon density: 1 $\sim$ 50 photons/nm^2. Pixel size: 100 $\sim$ 500 nm. The list inserted in the figure shows the required pixel size and photon density for each defect to get SNR $\geq$ 15.

Critical Defect	H = 1nm (Reference)	H = 0.5 nm (Target)	
Pixel Size Requirement (nm)	500	**100**	
Scanning Speed	1x	**25x**	**1x***
Photon Density Requirement	1x	**2x**	**2x**
Effective Source Power (mW in 16° cone angle)	26	**1300 (50×)**	**52 (2×)***
DPP source power (Watt / 2π sr)	5	**250**	**10***

Figure 2.37: The list showing the EUV source power requirement under fixed inspection time for EUV actinic blank inspection tool. *With increased CCD camera pixel counts to cover a larger footprint on the mask which can keep the scanning speed as the same even under smaller pixel size.

on published results [26]. For the 0.5 nm defect, there are two scenarios: with or without increased CCD pixel count, which can lead to different source power requirements. Without increasing CCD pixel count, the scanning speed of the inspection tool has to increase due to smaller field size. This also reduces the exposure time for each pixel thus introducing an additional burden on the source power requirement. A 50× increase in source power is needed due to the smaller pixel size and higher photon density requirement. With increased CCD pixel count, a larger footprint on the mask can be covered in order to keep the scanning speed the same to compensate the impact of the smaller pixel size. With this configuration, only 2× in source power is needed for the smaller critical defect. For the DPP / LDP source, a 10 Watt source power in 2π sr (solid angle) is enough under this new configuration for the 0.5 nm defect with an SNR ≈ 15.

2.6 Conclusion

In this chapter, potential optical configurations to improve the signal strength of phase defect and thereby increase inspection tool efficiency were discussed. To leverage the nature of the defect, the possibility of using the Zernike phase contrast method at EUV wavelength for phase defect inspection on EUV mask blanks was studied. The simulation results showed that a higher defect sensitivity (+30%) and in-focus inspection capability can be achieved by the Zernike phase contrast method, while the conventional bright field method needed through-focus scanning and resulted in lower defect detection sensitivity. With the consideration of defect SNR, the Zernike phase contrast method still has higher SNR (+18%) even though the speckle noise from the phase-dominated mask roughness is also increased. Moreover, with apodization in the pupil plane, the defect SNR can be further improved by utilizing the difference in frequency distribution between defect signal and speckle noise. Stronger reduction on noise than signal improves the overall SNR.

The SHARP EUV microscope at LBNL was used to demonstrate the Zernike phase contrast method for EUV actinic blank defect inspection. Due to the flexibility of Fresnel zoneplates, a customized pupil function can be easily introduced into the imaging system compared to using reflective optics (mirror), which is difficult and costly to fabricate. The experimental results confirmed the thin mask simulation results regarding the advantages of the Zernike phase contrast method. Phase defect as small as 0.35 nm in height, which is below the AFM measurement noise level, was detected with an SNR ≈ 8 at best focus. Moreover, the impact of mixed (phase + absorption) defects was discussed. Analysis showed that increasing the absorption component in the defects can change their through-focus behavior and affect the defect SNR improvement at best focus by the Zernike phase contrast method. Measurements for a native defect using different apodization conditions showed that the signal decreases more slowly than the noise with reducing background intensity transmission. From 100% to 8% intensity transmission, the signal is reduced by 55% while the noise is reduced by 80%, thus resulting in a 2× enhancement on defect SNR.

The simulation results on inspection efficiency comparison between the Zernike phase

contrast method and the dark field method were analyzed to gain a better understanding of the impact of defect type, pixel size, and photon level in the inspection system toward defect SNR. Instead of using speckle noise and a constant system noise to account for all the other noise sources in the inspection system, defect SNR was calculated by the consideration of photon shot noise, speckle noise, and camera noise. The results showed that the Zernike phase contrast method has different detection sensitivity for bump and pit defects due to the different physical mechanisms. Moreover, photon shot noise from the background limits the advantages of the Zernike phase contrast method to small pixel size and low photon level. This means that the Zernike phase contrast method is only suitable for review mode, which requires fine image resolution, while the dark field method is the preferred approach for inspection mode because it can operate at larger pixel size and higher photon density, which can lead to high throughput and high detection sensitivity.

At the end of the chapter, the impact of various tool design parameters on a dark field based EUV actinic blank inspection was studied including pixel size, EUV source type, and photon collection efficiency. The dominance of pixel size on defect SNR was first shown in the discussion. Increasing pixel size significantly beyond the defect size can collect more speckle noise than the defect signal, thereby reducing the SNR. The results also showed that the dominant noise source transitions from defect shot noise to speckle noise as pixel size increases. Studying the impact of EUV source type showed that a plasma source works best with larger NA illumination whereas the synchrotron source works best with nearly coherent illumination, given that the mask illumination photon density is assumed to increase with collection NA for plasma sources, but be fixed as a function of collection NA for synchrotron sources. The impacts of increasing the outer NA and photon density were studied as well. The impact of outer NA saturates at outer NA ≥ 0.3. The impact of increasing photon density saturates faster with increasing pixel size. The system requirements for future critical defects showed that a smaller pixel size and a stronger source power are needed to increase the critical defect SNR.

Chapter 3

Enhancing Pattern Defect Detection Sensitivity for Extreme Ultraviolet Actinic Patterned Mask Inspection

This chapter investigates issues regarding EUV patterned mask defectivity and actinic (at-wavelength) inspection tool development. In Section 3.2, the multilayer defect detection sensitivity on EUV patterned mask using the Zernike phase contrast method is discussed. Also explored is the possibility of improving inspection efficiency for phase and absorber defects simultaneously by optimizing the phase shift in the pupil. The phase effects in EUV pattern defects and implications on the Zernike phase contrast method are discussed in Section 3.3. In Section 3.4, the impact of optical design and noise sources on pattern defect sensitivity for a bright field based EUV actinic inspection tool is discussed to analyze the required tool design that can reach the desired defect detection capability.

3.1 Background

Patterned mask inspection is used to assure the image quality of the patterned mask. The mask-making procedure is shown in Fig. 3.1 [14]. In this flow, patterned mask inspection occurs at both the mask shop and wafer fab. It plays an important role in ensuring the cleanliness of the mask, both before it is used and during its use for wafer printing. Any unexpected defect or contamination must be identified so that appropriate mask cleaning or repairs can be applied.

For EUV masks, the pattern is defined by the absorber material on top of the Ru-capped multilayer mirror, as shown in Fig. 3.2. Currently, Ta-based absorber materials, e.g. TaN and TaBN, are being used due to their high absorption at EUV wavelength. However, other absorber materials like Ni or Co which have stronger absorption than Ta are also being considered, as they may enable reduction of mask thickness, and thereby the thick mask effects [36]. The potential for Ni and Co can be seen in the refractive index data shown in

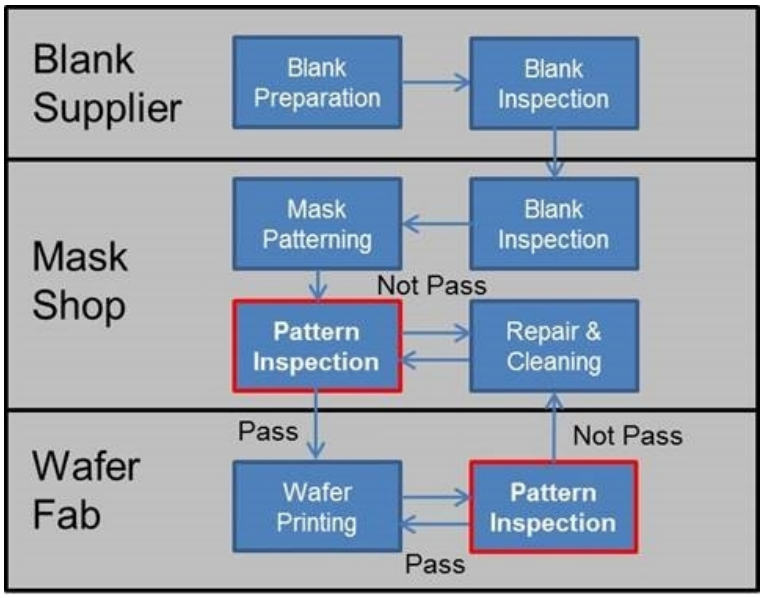

Figure 3.1: The process flow of photomask fabrication [14].

Figure 3.2: Schematic diagram of EUV mask.

Fig. 3.11 from their higher absorption and yet similar phase delay of Ta. Moreover, different patterned mask designs like etched multilayer, multilayer absorber, and etched phase shifting mask which show better imaging performance than the current EUV patterned mask design have been proposed [37, 38, 39].

Due to the status of mask blank defectivity, a dark field mask that has limited open area is commonly used to cover the blank defects by the absorber [19]. However, beyond the defects from the mask blank, the defects created during the pattern fabrication process pose a larger problem. To identify the pattern defect, optical inspection using DUV light is currently the standard approach. Even though the operating wavelength for DUV inspection (193 nm) is different from the EUV mask (13.5 nm), it still provides enough optical

Figure 3.3: Optical properties of the elements at 13.5 nm, showing the potential candidate to replace Ta-based absorber [36].

resolution for the current technology node. However, as EUV lithography marches towards high-volume manufacturing for the future advanced node (< 7nm), the resolution limitation of DUV inspection becomes a problem [14]. Electron-beam inspection is an alternative solution. However, the current low throughput makes this method suitable only for technology development, but not for high-volume manufacturing [40].

To have a long-term solution for EUV patterned mask inspection, EUV actinic pattern inspection is highly desired. Actinic inspection enables superior optical resolution and through-pellicle inspection which is not feasible by either DUV or electron-beam inspection [9]. However, a clear development plan to bring an actinic patterned mask inspection tool into production has not yet been initiated, even though this concern has been raised in the past few years.

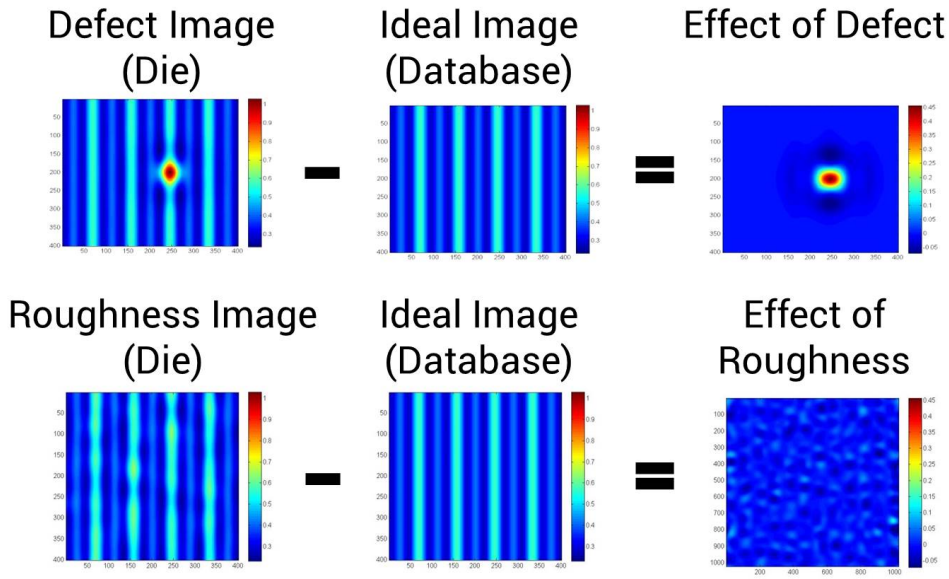

Figure 3.4: Schematic diagram of the die-to-database approach for the impact of pattern defect signal.

3.2 Simulation study of phase-enhanced defect detection sensitivity for EUV patterned mask inspection

In patterned mask inspection, both multilayer defects and absorber defects are of concern. The defect sizes studied here are those deemed to produce critical dimension (CD) variations of a maximal critical size when projection printed with dipole illumination. For simplicity in this section, the multilayer defect is assumed to be a pure phase defect, while the pattern defect is assumed to be pure amplitude.

The simulation study uses a thin mask 2D model to generate the EUV (13.5 nm) images. In the subsequent analysis, die-to-database inspection is assumed, as shown in Fig. 3.4. In this section, the defect and mask roughness images with layout pattern are simulated independently. In defect and roughness images, the impact of the phase defect and the phase roughness is shown in the space of the dense line pattern under the disk illumination. The images indicate that the phase defect and phase roughness affect the pattern image quality. With the ideal (defect free) image of the layout pattern from the database, the difference caused by the defect and the mask roughness can be identified. Then defect signal strength and speckle noise can be calculated by subtracting the background pattern signal to show the effect under various conditions.

With this information, the defect SNR is defined in Eq. 3.1. In this section, the noise

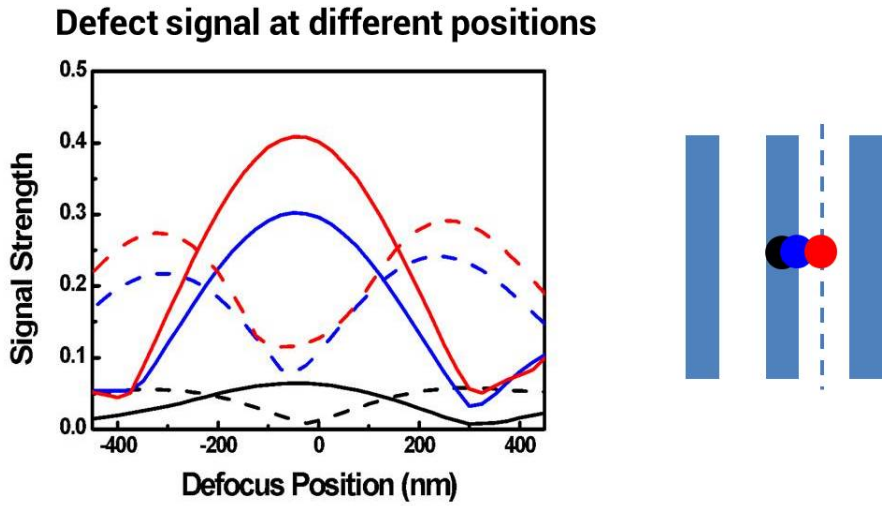

Figure 3.5: Phase defect (Height: 1 nm, FWHM: 40 nm) signal strength at different defocus positions. Black: beneath the pattern. Blue: at the edge of the pattern. Red: centered at the spacing. Solid curves: the Zernike phase contrast method. Dash curves: the conventional bright field method (Left). The relative position of defects on the pattern (Right).

sources are simplified to speckle noise and system noise. Speckle noise is assumed to come from mask roughness and is calculated as the standard deviation of intensities resulting from the noise image. System noise is a constant to account for all other noise sources which are independent of the mask such as photon noise and electrical noise from the camera. Larger SNR means the defect is more easily distinguished from the noise, which leads to a higher capture rate:

$$\text{Defect SNR} = \frac{\text{Defect Signal}}{\text{Speckle Noise} + \text{System Noise}} \tag{3.1}$$

To further extend the application of the Zernike phase contrast method beyond the actinic blank inspection, its application to patterned mask inspection is studied in this chapter. The impact of the interaction between the multilayer defect and the absorber pattern on the defect signal while using the Zernike phase contrast method is discussed in Section 3.2.1. The possibility of improving the inspection efficiency for phase and amplitude defects simultaneously in patterned mask inspection is explored in Section 3.2.2.

3.2.1 Impact of multilayer defect location on defect sensitivity using the Zernike phase contrast method

This section discusses the impact of multilayer defect location on defect sensitivity. The bump defect used in the thin mask simulation is 1 nm in height and its FWHM is 40 nm.

The linewidth of the dense line pattern used in the study is 44 nm on the EUV mask (11 nm in wafer scale). The inspection NA is 0.2, and disk illumination with a sigma value of 0.5 is assumed.

As shown in Fig. 3.5, the enhancement of the phase defect peak signal strength depends on its position relative to the absorber pattern. The improvement in peak signal strength is larger with less pattern overlap. The peak signal strength has 37.8% enhancement compared with the maximum value obtained with the conventional bright field method when the defect is centered in the space, while the enhancement drops to 22.8% and 9.4% when the defect is at the edge and beneath the absorber line respectively. The results indicate that the interaction between the phase defect and the absorber pattern compensates the effect of the Zernike phase contrast method. However, the maximum signal value remains at best focus when there is a +90° phase shifts in the pupil plane.

3.2.2 Improve inspection efficiency on absorber and phase defects by varying the phase shifts in the pupil plane

Figure 3.6a shows the signal strength at different defocus positions for a phase defect with and without the Zernike phase contrast method. As expected, the peak signal strength is at best focus for the phase defect when the Zernike phase contrast method is applied. However, as shown in Fig. 3.6b, the position of the amplitude defect peak signal strength is moved out of focus when the Zernike phase contrast method is used. Therefore, there is only one type of defect at best focus that can be observed even with the Zernike phase contrast method.

To see if it is possible to observe both types of defects at best focus simultaneously, the signal strength of phase and amplitude defects at best focus is calculated with different phase shifts from 0° to +90°. The signal strength shown in Fig.3.6c has been normalized to its maximum value for both types of defects. The phase defect height is 1 nm and an FWHM ranges from 20 to 100 nm. The width of the square amplitude defects ranges from 20 to 100 nm. As shown in Fig. 3.6c, phase defects have maximum signal strength with +90° while the amplitude defect signal strength drops to 25% of its maximum value at +90°. By choosing a phase shift of $\approx +50°$, an acceptable trade-off between phase and amplitude defect signal strengths can be achieved. With optimized phase shift, one can observe both amplitude and phase defects with a single scan at best focus thereby potentially improving inspection throughput.

Figure 3.7 shows the defect SNR for phase and absorber defects on a patterned mask as a function of different phase shifts. These defects are chosen to introduce at least 5% CD variation at the wafer plane by simulation. The maximum SNR for phase and absorber defects is found at +90° and 0° phase shifts respectively. At the optimized phase shift, the SNR for phase defects is 4 and the SNR for absorber defect is 10. The effect of speckle can increase by a factor of $\sqrt{2}$ if the effect of surface roughness is based on the die-to-die comparison. The result shown here indicates the possibility of improving the throughput of the mask inspection system by detecting phase and absorber defects simultaneously by

utilizing proper pupil design.

3.3 The study of phase effects in EUV mask pattern defects

Due to both the oblique illumination of EUV lithography system and strong material-induced phase from the EUV absorber material, absorber defects on EUV masks cannot be treated as pure absorption objects. A recent study shows that absorber defects on patterned masks act like phase defects based on Bossung plot analysis [41]. The results indicate that the phase effects on the absorber defect needs to be addressed to optimize the printing condition on the wafer. It is also important for the development of patterned mask inspection tools to fully understand the defect behavior and options for optimizing sensitivity.

In this section, the impact of illumination conditions, material properties, and defect sizes on through-focus behavior including defect sensitivity and its peak signal position is discussed. Potential solutions to reduce the impact of phase effects on absorber defects from the inspection point of view are explored, including new absorber materials and the optimum phase shift method.

3.3.1 Background

Unlike the original Zernike phase contrast method which is shown in Fig. 3.8a, the optimum phase shift method is targeted for defects with mixed (phase + absorber) behavior, like the EUV mask pattern defect, which is formed by phase-shifting absorber material. As shown in Fig. 3.8b, the 90° phase shifts on unscattered background light is not aligned with the scattered light from hybrid defects. Therefore, a more optimal phase shift is needed to achieve better image contrast, as shown in Fig. 3.8c.

3.3.2 Simulation settings and parameters

Rigorous 3D mask modeling is used to study the EUV mask absorber phase effects [42]. In order to improve the simulation efficiency, the Fourier boundary condition is used to model an EUV multilayer mirror. For the default absorber material, a combination of TaN and TaON is used, as shown in Fig. 3.9. For the inspection optical configuration, an NA of 0.2 is used, and the illumination is set to disk with a sigma of 0.3. The pattern used for the following discussion is dense line and iso-line (line : space = 1 : 3) pattern with 16 nm half pitch in wafer scale, and also dense contact pattern with 20 nm half pitch in wafer scale. Square extrusion and intrusion defects with a size up to 50% of the half pitch of the desired pattern are used for the discussion. To show the impact of the defect, a die-to-database defect detection approach is used, as shown in Fig. 3.4.

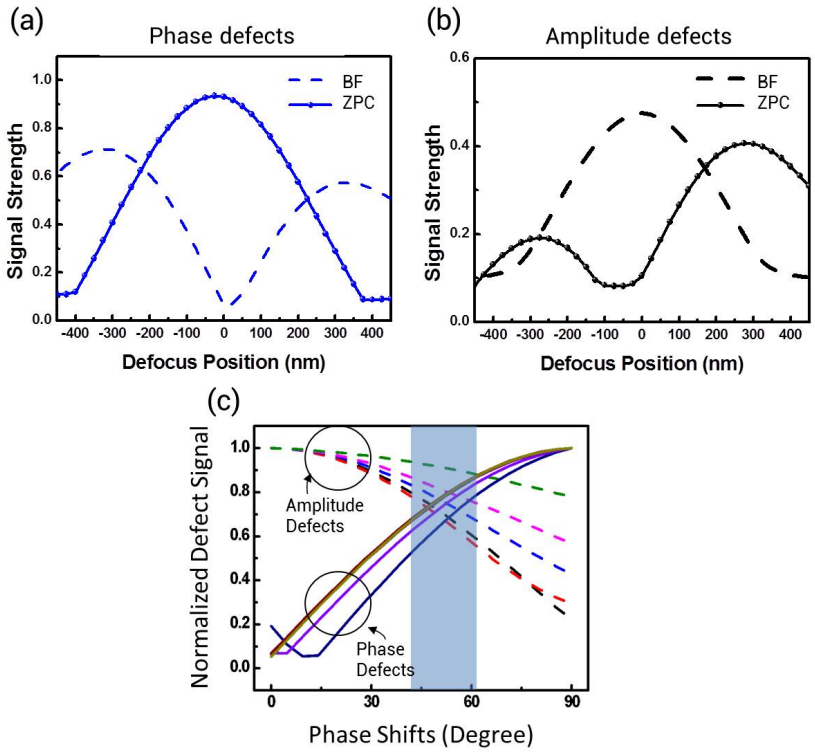

Figure 3.6: Defect signal strength at different defocus levels with the Zernike phase contrast method (solid curve) and the conventional bright field method (dash curve): (a) Bump defect (Height: 1 nm, FWHM: 60 nm). (b) Amplitude defect (Width: 10 nm). (c)Normalized signal strength at the focus for both amplitude and phase defects with different phase shifts degree. Shaded area indicates the optimized phase shift region.

Defect Type	SNR @ focus 0 degree	SNR @ focus 47 degree	SNR @ focus 90 degree
Amplitude at the edge (width: 25nm*50nm)	14.80	***9.63***	4.65
Bump at the spacing (h: 1nm, fwhm: 60nm)	0.92	***3.42***	4.5
Pit at the spacing (h: 1nm, fwhm: 60nm)	0.92	***3.02***	3.58
Bump at the spacing (h: 1.5nm, fwhm: 40nm)	2.48	***3.66***	5.71
Pit at the spacing (h: 1.5nm, fwhm: 40nm)	2.48	***4.74***	4.84

Figure 3.7: The list of defect SNR at best focus with different phase shifts for different types of the defect at different locations on the mask by patterned mask inspection.

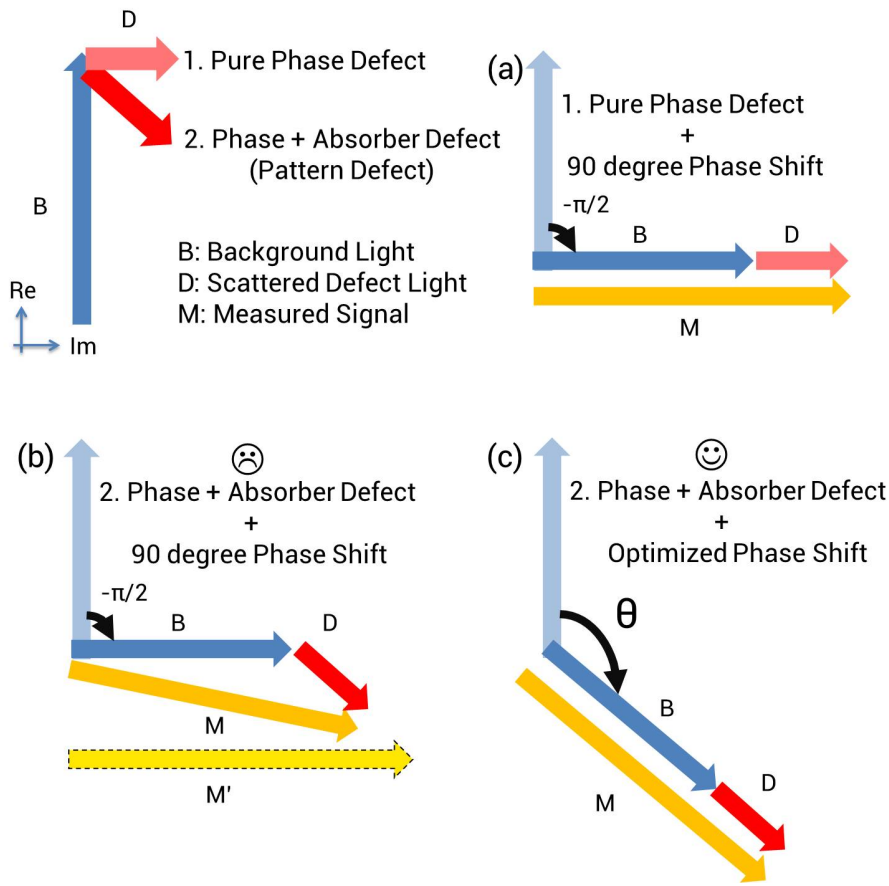

Figure 3.8: Phasor diagram for pattern defect: (a) 90° phase shifts with pure phase defect. (b) 90° phase shifts with pattern defect. (c) Optimum phase shift method for pattern defect.

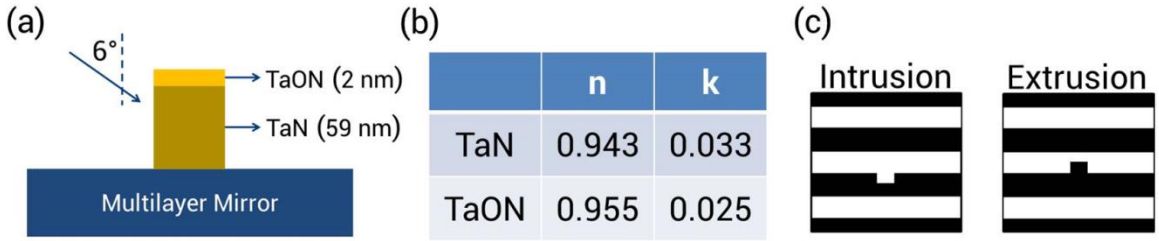

	n	k
TaN	0.943	0.033
TaON	0.955	0.025

Figure 3.9: (a) Side view of a schematic diagram of EUV mask pattern: absorber pattern height and illumination orientation. (b) Optical properties of the absorber materials at EUV wavelength (13.5 nm). (c) Top-down view of intrusion / extrusion defect definition: Black is the absorber and white is the spacing.

3.3.3 Impact of illumination, material property, and defect size on pattern defect through-focus behavior

To show the impact of different variables on pattern defects, the defect near field (amplitude, phase) distribution can be used to provide the information, as shown in Fig. 3.10. For both types of defects, the defect amplitude distribution with oblique illumination is different from the normal incidence case and has a stronger energy accumulation/consumption in the defect region. For the phase distribution, the extrusion defect has more structure than the intrusion defect due to the coupling of neighboring absorber patterns. Also, oblique illumination changes the phase distribution at the edges of intrusion defects. The through-focus behavior of both intrusion and extrusion defects is shown in Fig. 3.11. Different defect types have different sensitivity even under the same illumination condition and defect size. Moreover, illumination angle is shown to have a significant impact on the results.

The EUV absorber material-induced phase is due to the difference in the real part of the refractive index (n) between air and the absorber material. The phase effects of EUV patterned mask has been reported by various researchers, showing the impact on imaging performance [41, 43, 12]. For defect inspection, the material-induced phase also changes the defect near field distribution. As shown in Fig. 3.12a, with the real part of the refractive index intentionally set to 1 while keeping the absorption (k) as the same, the defect amplitude drops drastically. The energy confinement effect is due to the difference in refractive index forming a waveguide effect in the defect region. The intrusion defect has stronger energy confinement in the defect region while the extrusion defect has stronger energy consumption in the defect. Changing the material properties also changes the through-focus behavior and sensitivity, as shown in Fig. 3.12b. Less waveguide effect reduces the defect sensitivity, and less induced phase makes the defect absorption dominated. Both types of defects have lower sensitivity than the TaN-based pattern defect, and the peak signal position is closer to the best focus position which indicates the defect is absorption dominated.

The defect amplitude and phase are changed accordingly under various defect sizes, as shown in Fig. 3.13a. The magnitude and peak position of amplitude and phase distribution vary as defect size changes. However, defect size only has an impact on defect sensitivity, not the overall through-focus behavior. As shown in Fig. 3.13b, the different defect sizes have a similar through-focus trend with different defect signal strengths. This feature can be utilized by the optimum phase shift method. The same pupil function can be applied to different defect sizes to enhance their defect sensitivity simultaneously due to the similarities of their through-focus behavior.

3.3.4 Reduce phase effects on pattern defect by new materials

To reduce the absorber phase effects, alternative EUV absorber material systems with the real part of the refractive index (n) close to 1, or materials with strong absorption can be used. These new materials can reduce the absorber height thereby reducing the induced phase. Table 3.1 shows the alternative material solutions to reduce material-induced phase.

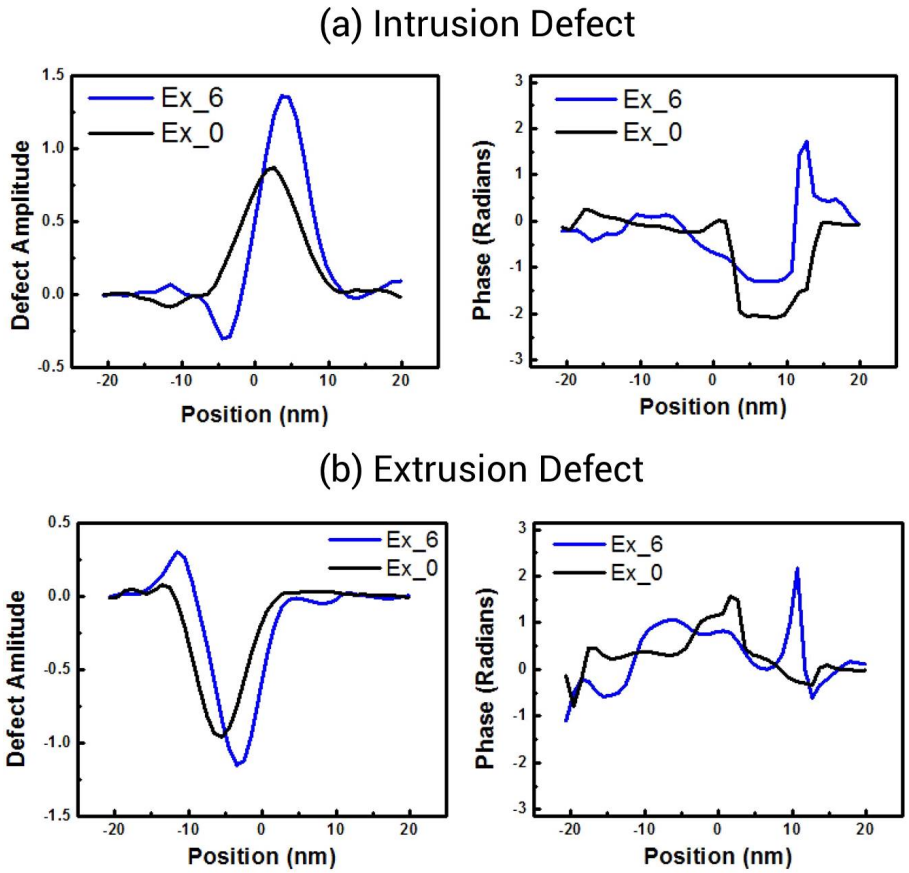

Figure 3.10: Defect near field distribution (a) Intrusion defect: CRA = 6° (Blue) and CRA = 0° (Black). (b) Extrusion defect: CRA = 6° (Blue) and CRA = 0° (Black). Defect size: 8×8 nm^2 in wafer scale.

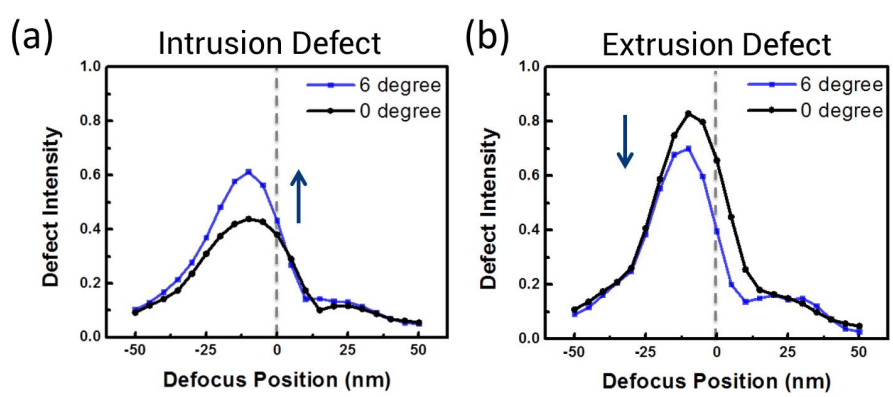

Figure 3.11: (a) Intrusion defects through-focus behavior: CRA = 6° (Blue) and CRA = 0° (Black). (b) Extrusion defects through-focus behavior: CRA = 6° (Blue) and CRA = 0° (Black). Defect size: 8×8 nm^2 in wafer scale.

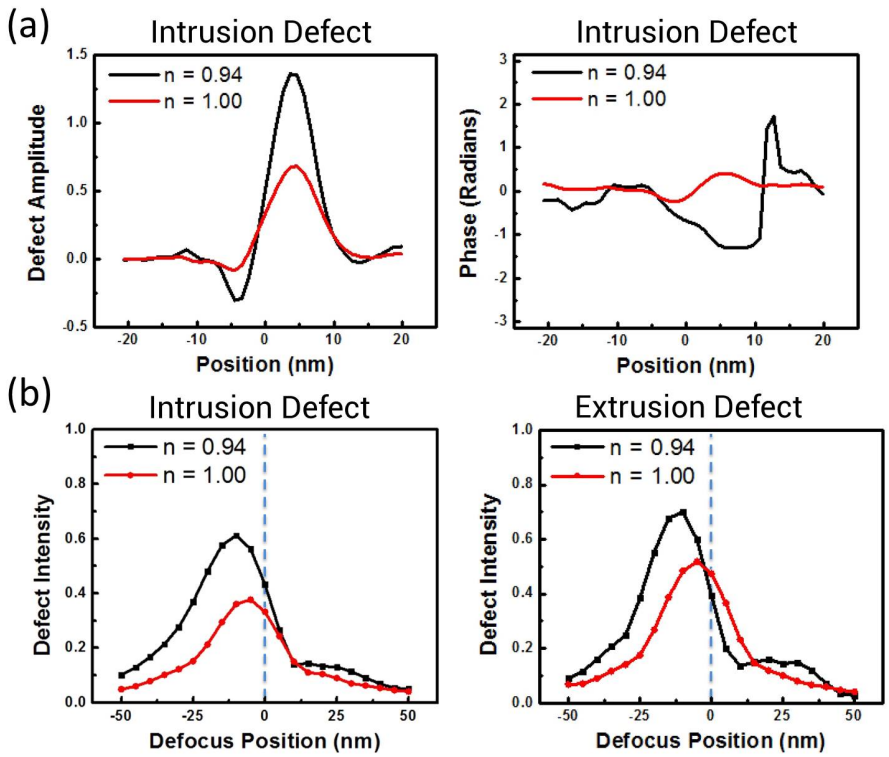

Figure 3.12: (a) Intrusion defect near field distribution: $n = 0.94$ (Black) or $n = 1$ (Red). (b) Intrusion (Left) and extrusion (Right) defects through-focus behavior: $n = 0.94$ (Black) or $n = 1$ (Red). Defect size: 8×8 nm^2 in wafer scale.

Compared to the TaN-based absorber, Nickel (Ni) has stronger absorption and n close to TaN, and Germanium (Ge) has n closer to 1 with absorption about the same as TaN. In order to compare the impact of material-induced phase by different absorbers, the absorber heights for Ni and Ge have been adjusted in the simulation model to match the absorption of TaN-based material system.

$\lambda = 13.5nm$	**n**	**k**
TaN (Ref.)	0.943	0.033
Ni	0.948	0.073
Ge	0.995	0.032

Table 3.1: Refractive index $(n + ik)$ of EUV absorber material at 13.5 nm. Data for Nickel (Ni) and Germanium (Ge) are retrieved from CXRO/LBNL database.

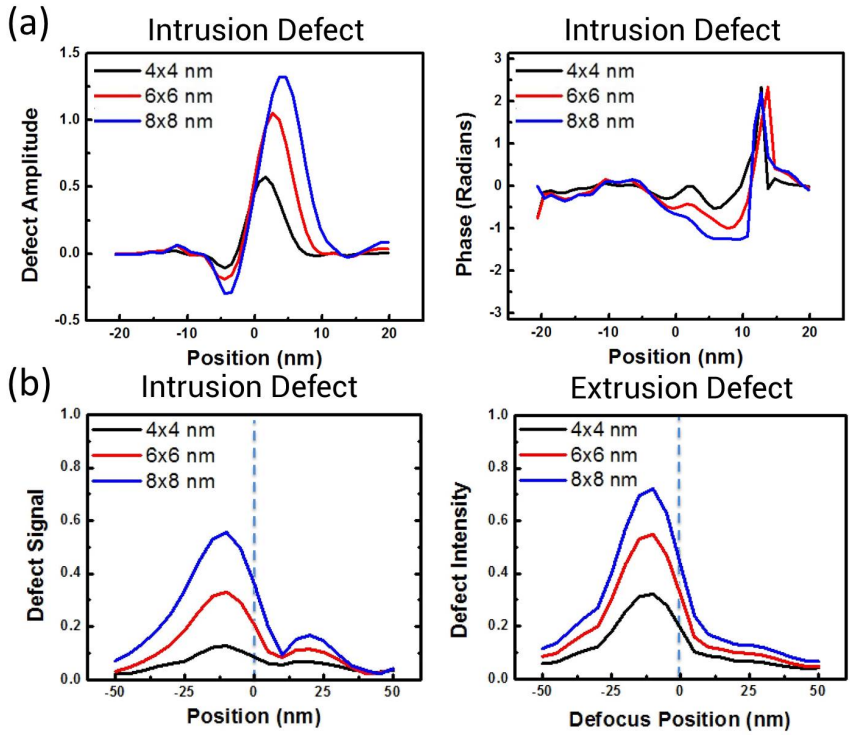

Figure 3.13: (a) Intrusion defect near field distribution with different defect sizes: 4×4 nm^2 (Black), 6×6 nm^2 (Red), and 8×8 nm^2 (Blue). (b) Intrusion (Left) and extrusion (Right) defects through-focus behavior with different defect sizes: 4×4 nm^2 (Black), 6×6 nm^2 (Red), and 8×8 nm^2 (Blue). The scale mentioned in the figure is in wafer scale.

The corresponding near field data is shown in Fig. 3.14. Ni exhibits smaller amplitude due to reduced absorber height, and Ge has smaller amplitude due to the reduced difference in refractive index between Ge and air. Ni and Ge both have smaller phase in the defect region compared with TaN-based materials. Figure 3.15a shows the extrusion defect through-focus behavior for various absorber material systems. With reduced phase effects, Ni and Ge show a different trend from that of TaN. First, the defect signal is smaller which indicates reduced impact of the material-induced phase under the same absorption condition. Second, the material-induced phase is smaller for Ni and Ge compare to TaN and the peak signal positions are closer to focus, as shown in Fig. 3.15b. For the optimum phase shift method which improves the defect signal at best focus, Ni-based and Ge-based 8×8 nm^2 intrusion defects have their optimum phase shifts at $-48°$ and $-28°$ respectively, as opposed to $-54°$ for TaN-based intrusion defects, as shown in Fig. 3.15c.

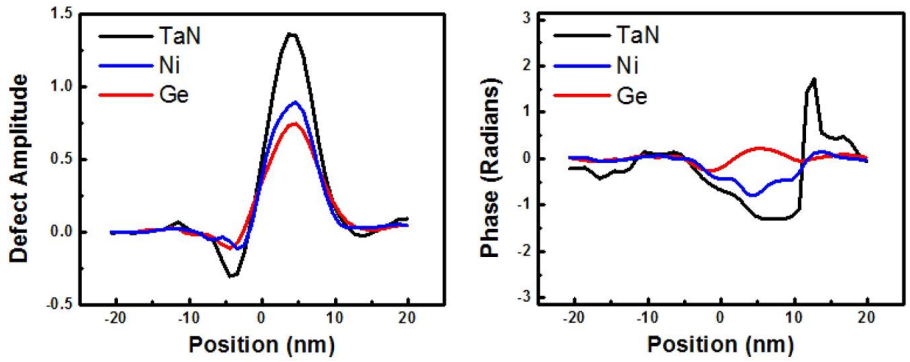

Figure 3.14: Intrusion defect near field distribution with different absorber materials: TaN (Black), Ni (Blue), and Ge (Red). Defect size: 8×8 nm^2 in wafer scale.

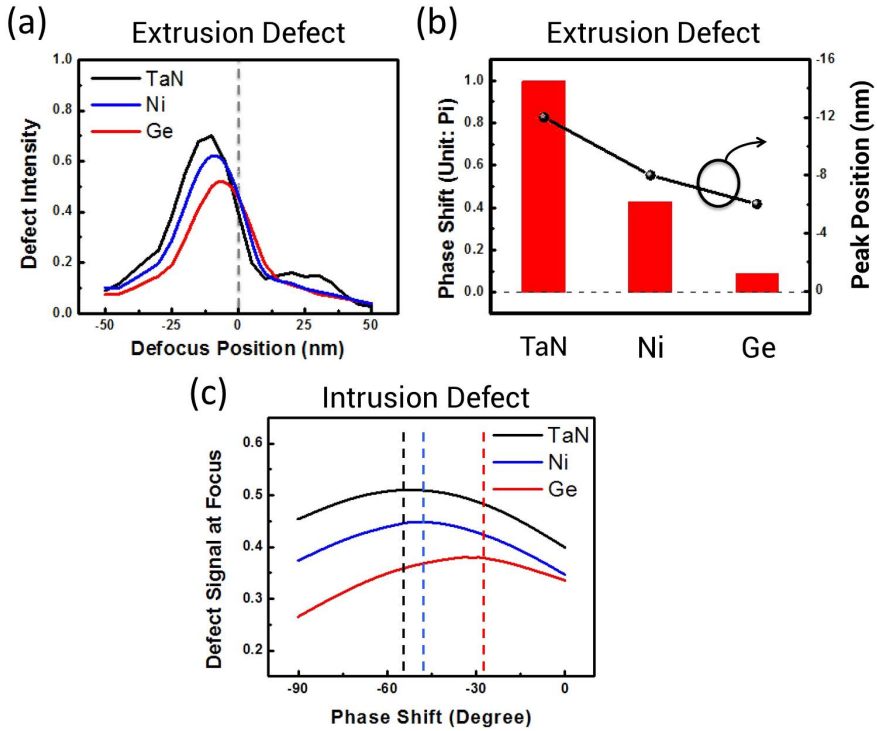

Figure 3.15: (a) Extrusion defect through-focus behavior with different absorber materials: TaN (Black), Ni (Blue), and Ge (Red). (b) Material-induced phase and the peak defect signal position of the extrusion defect with different absorber materials. (c) Intrusion defect signal at best focus under various phase shifts with different absorber materials: TaN (Black), Ni (Red), and Ge (Blue). Defect size: 8×8 nm^2 in wafer scale.

3.3.5 Improve pattern defect sensitivity by the optimum phase shift method

In order to improve pattern defect inspection efficiency in the TaN-based material system, the optimum phase shift method can be used to modify defect through-focus behavior. As previously reported, the Zernike phase contrast method is utilized to form strong interference between the background and multilayer defect waves thereby increasing the sensitivity at best focus [44, 45, 46]. Since multilayer defects on the EUV mask blank are mostly phase dominated, a 90° phase shift maximizes the defect signal strength. However, the optimum phase shift is different for an absorber defect on a patterned mask due to the nature of the defect, which is a combination of phase and absorption.

The optimum phase shift for different defect types on dense line pattern is shown in Fig. 3.16a. Extrusion defects have an optimum phase shift close to $-60°$ among various defect sizes, while intrusion defects have an optimum phase shift $\approx -45°$. Moreover, extrusion defects have larger signal enhancement than intrusion defects, as shown in Fig. 3.16b. The difference in optimum phase shift and signal enhancement between extrusion and intrusion defects can be attributed to the difference in mask properties, as shown in Fig. 3.16c. The extrusion defect has larger footprint than the intrusion defect under the same illumination condition even though their size on the mask is the same. For an iso-line pattern, similar defect behavior in terms of optimum phase shift and signal enhancement is observed, as shown in Fig. 3.17.

For dense contact pattern, the impact of the optimum phase shift method depends on defect size and location, as shown in Fig. 3.18. With the same defect size, the location of the defect determines the optimum phase shift. Defects at the right edge of the dense contact suffer a stronger shadowing effect than the other defects under the same illumination condition, as shown in Fig. 3.18c. Therefore, these defects have a larger optimum phase shift and larger signal enhancement than those located at the center or left edge of the contact. Moreover, the impact of the optimum phase shift method is negligible for defect size $< 2 \times 2$ nm^2.

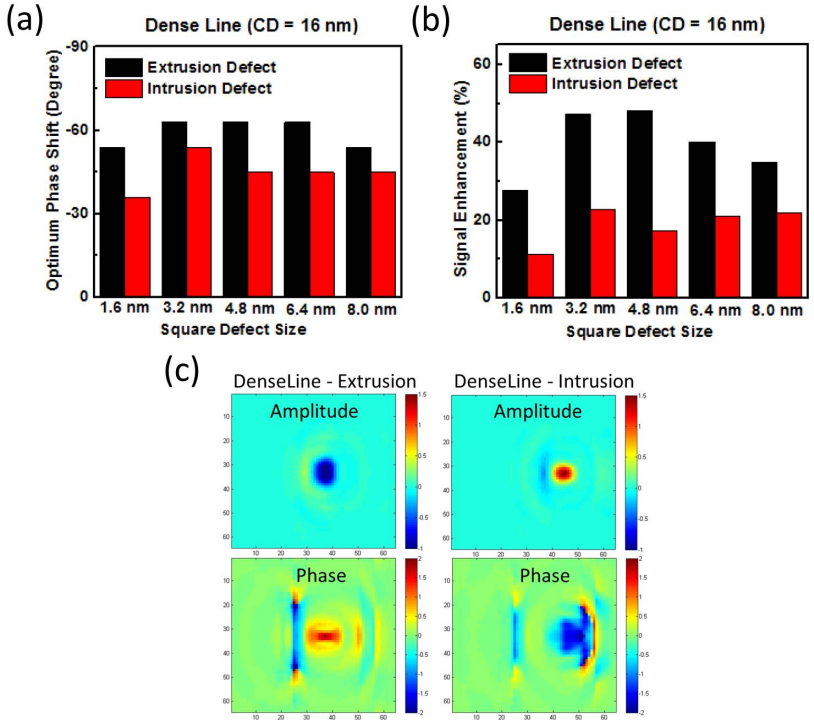

Figure 3.16: (a) Optimum phase shift for various defect sizes of extrusion defects (Black) and intrusion defects (Red) on dense line pattern. (b) Signal enhancement for various defect sizes of extrusion defects (Black) and intrusion defects (Red) on dense line pattern. (c) Extrusion (Left) and intrusion (Right) defects near field distribution. Defect size: 8×8 nm^2. The scale mentioned in the figure is in wafer scale.

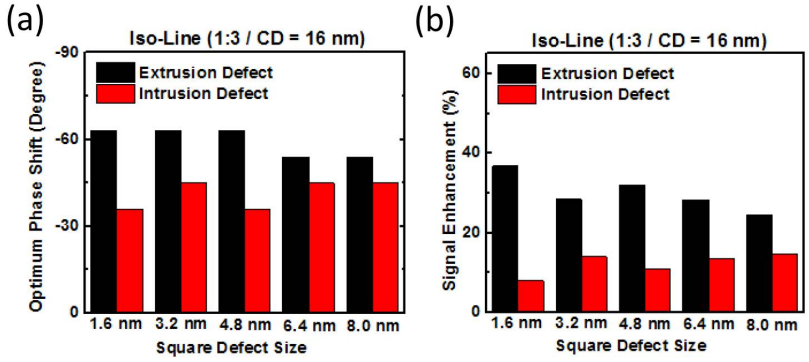

Figure 3.17: (a) Optimum phase shifts for various defect sizes of extrusion defects (Black) and intrusion defects (Red) on iso-line pattern. (b) Signal enhancement for various defect sizes of extrusion defects (Black) and intrusion defects (Red) on iso-line pattern. The scale mentioned in the figure is in wafer scale.

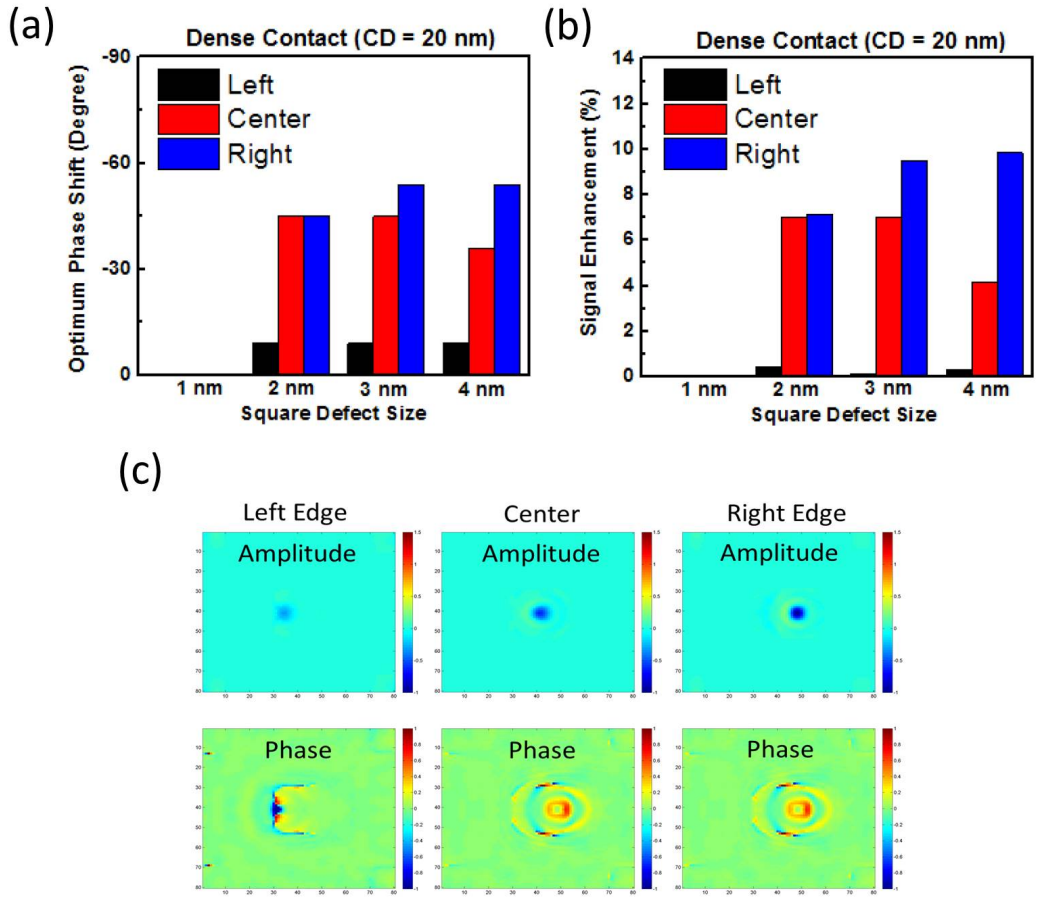

Figure 3.18: (a) Optimum phase shifts for various defect sizes at left (Black), center (Red), and right (Blue) of the dense contact pattern. (b) Signal enhancement for various defect sizes at left (Black), center (Red), and right (Blue) of the dense contact pattern. (c) Near field distribution for defects at different locations in dense contact pattern. Defect size: 4×4 nm^2. The scale mentioned in the figure is in wafer scale.

3.4 Impact of noise sources and optical design on pattern defect detection sensitivity for EUV actinic pattern inspection

In this section, the relationship between various noise sources and the optical design in a bright field based EUV actinic patterned mask inspection tool is studied. Noise sources in patterned mask inspection include speckle noise from the surface roughness, camera noise from the dark current of the CCD camera, and photon shot noise. Additionally, pixel size and photon level (source power) are critical factors in determining the throughput and defect sensitivity. With a fixed number of photons per pixel, a larger pixel size might increase the throughput but lower both the defect signal strength and noise. On the other hand, with a fixed number of photons per nm^2, a larger photon count per pixel achieved by increasing the pixel size might increase the pixel signal strength but also increase the photon shot noise from the defect signal and background pattern intensity. Also, even though the optimum phase shift method can improve defect sensitivity by utilizing the phase component of the pattern defect as mentioned in the previous section, a detailed SNR calculation is needed to understand the impact of the optimum phase shift method on various noise sources.

To gain a better understanding of these trade-offs and interplay, in this section the impact of each noise source and defocus under various pixel sizes and photon densities on defect SNR is discussed. Defect sensitivity for a set of critical defects is then calculated and the limiting case which has the smallest defect SNR is identified. To improve the limiting case defect SNR, the impact of defocus is studied and the possibility of introducing a nominal defocus into the inspection system to achieve a better defect capture rate is discussed. In the end, a comparison of inspection efficiency in the conventional bright field method and the optimum phase shift method is presented.

3.4.1 Simulation settings and parameters

The simulation study presented here uses a hybrid (2D + 3D) mask model to generate the EUV images. For the imaging conditions, a bright field imaging mode with an NA of 0.16 and disk illumination with a sigma value of 0.3 is used. For the detector conditions, pixel size ranging from 10 nm to 50 nm in mask scale is used, and a photon level of 1000 photons/pixel or approximately 10 to 50 photons/nm^2, is used for the simulation depending on the pixel size. The patterns used in the simulation are ideal without the impact of mask line edge roughness (LER). The goal of actinic inspection of the patterned absorber is to identify locations where significant deviations from design in the absorber shape occur. Dense line and iso-line perpendicular to the 6° incident illumination angle with 64 nm half pitch in mask scale, and also ideal dense contact pattern with 80 nm half pitch in mask scale ared used for the study. Square-shaped extrusion and intrusion defects with size ranging from 6.4×6.4 nm^2 to 40×40 nm^2 are used. The definition of extrusion/intrusion defect and the optical properties of the absorber materials used for the EUV mask pattern are shown in

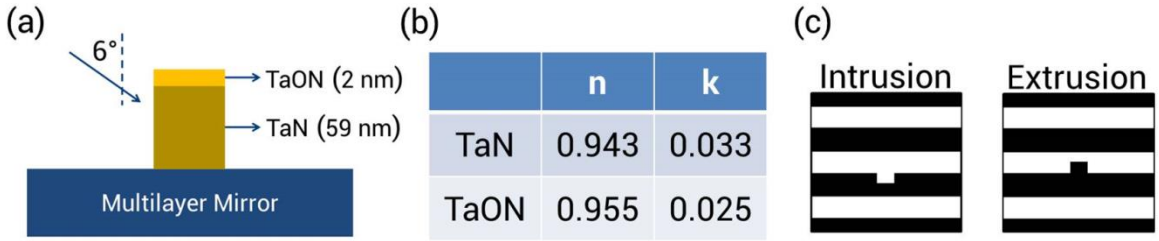

	n	k
TaN	0.943	0.033
TaON	0.955	0.025

Figure 3.19: (a) Side view of a schematic diagram of EUV mask pattern: absorber pattern height and illumination orientation. (b) Optical properties of the absorber materials at EUV wavelength (13.5 nm). (c) Top-down view of intrusion / extrusion defect definition: Black is the absorber and white is the spacing.

Fig. 3.19. For speckle, the mask roughness used is assumed to be 60 pm with a correlation length of approximately 100 nm [24, 25]. In the analysis, a die-to-database defect detection approach is assumed, subtracting the ideal (noise free) background pattern image, as shown in Fig. 3.4. However, as shown in Section 3.2, instead of simulating pattern defect and mask roughness images independently, a hybrid (2D + 3D) model is used to include both the absorber and substrate properties into the image simulation. Equation 3.2 shows the defect SNR definition used in the following discussion [47]. Photon shot noise includes the impact of both defect signal and pattern background intensity.

$$\text{SNR} = \frac{\text{Defect Signal}}{\text{Speckle Noise} + \text{Camera Noise} + \text{Photon Shot Noise}} \tag{3.2}$$

To include both the absorber and substrate properties into the patterned mask inspection modeling, the patterned mask electric field from a 3D model is extracted [42] and mixed with the 2D mask roughness electric field, as shown in Fig. 3.20. The reason to use the 2D mask roughness model instead of the 3D model is because it has previously been reported that the multilayer roughness effect can be adequately modeled with the single surface approximation [48]. This hybrid approach allows us to include not just the mask 3D effects of EUV mask, but also the interaction between mask roughness and pattern electric field modulation while keeping reasonable constraints on the size of the computation.

From the densely-sampled aerial image, pixel binning is used to mimic the results under different pixel sizes for both die and database images. Also, in our modeling of the inspection process, the effective signal to be derived is based on a 2×2 pixel convolution of the image. Figure 3.20 shows the aerial image as pixel size increases from 10 nm to 30 nm. In the final step, the system noise such as photon noise and camera noise is included to calculate the defect SNR from die-to-database images as those shown in Fig. 3.20.

In previous studies [41, 49], it was shown that the impact of the pattern phase effects due to the phase-shifting of absorber materials causes pattern defects to exhibit a mixed (phase + absorber) behavior. The impact of this, as shown in Fig. 3.21, is that the peak

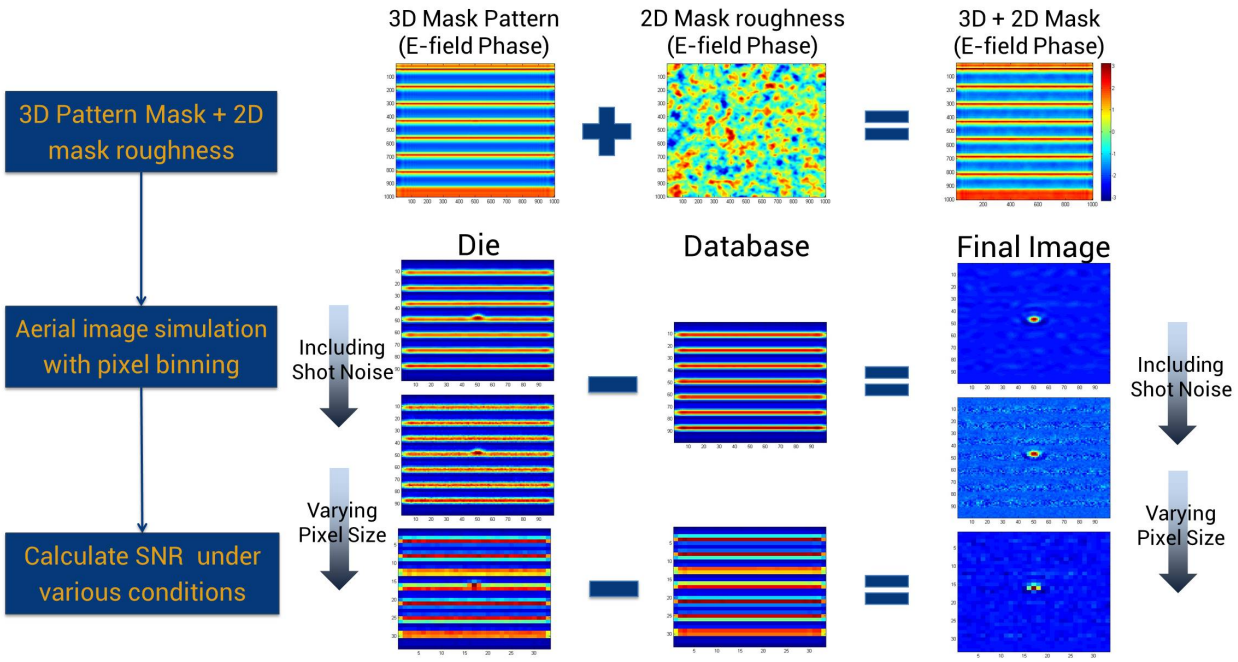

Figure 3.20: Schematic diagram of the defect SNR calculation process flow.

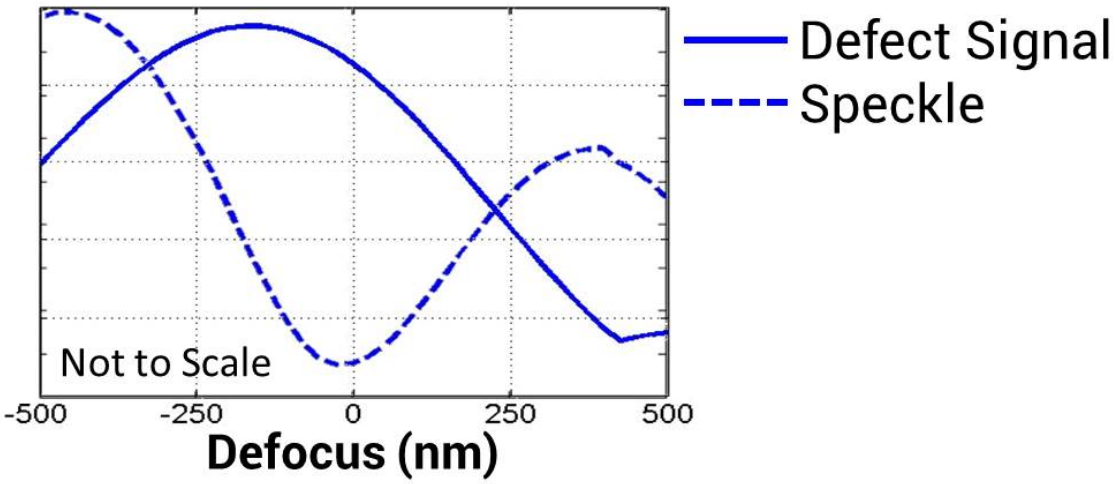

Figure 3.21: Schematic diagram of the defect signal and the speckle noise through-focus behavior. Defect Type: Dense line intrusion defect with a size $\approx 26 \times 26$ nm^2 on the mask.

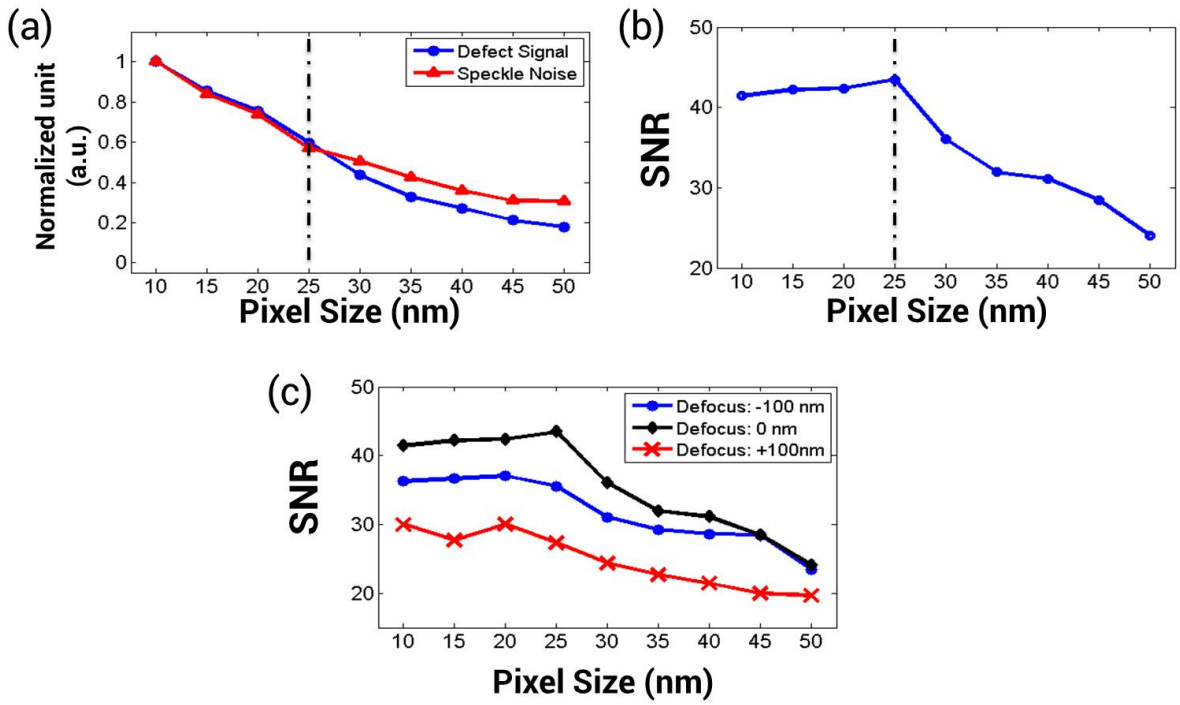

Figure 3.22: (a) Normalized defect signal and speckle noise under various pixel sizes relative to the value at 10 nm pixel size. (b) Defect SNR under various pixel sizes, only defect signal, and speckle noise are taken into the defect SNR calculation. (c) Defect SNR under various pixel sizes and different defocus positions: Defocus position = −100 nm, 0 nm, and +100 nm. Defect Type: Dense line intrusion defect with a size ≈ 26 × 26 nm^2 on the mask. The best focus position is defined as the position has minimum speckle contrast, as shown in Fig. 3.21.

defect signal is no longer at the best focus position of an ideal absorber defect. Moreover, the interaction between mask roughness and patterned mask also causes an asymmetric through-focus behavior for speckle noise and thus asymmetric through-focus SNR.

3.4.2 Defect signal vs. speckle noise under various pixel sizes and defocus positions

In the first step, only the defect signal and speckle noise are considered in the SNR calculation in order to understand the impact of pixel size on both terms. The example defect used here is a dense line intrusion defect with a size of 26 × 26 nm^2. As shown in Fig. 3.22a, the normalized signal strength and speckle noise drop with an increase in pixel size. Moreover, Figure 3.22b shows that signal drops faster than speckle noise as pixel size increases, causing smaller defect SNR when a larger pixel size is used in the inspection tool.

The drastic change of defect SNR when the pixel size is larger than 25 nm is due to the pixel area exceeding the optical resolution. The optical resolution limit for our system is 51 nm based on the NA (0.16) and the wavelength (13.5 nm). Therefore, the aerial image width of the sample defect used here is ≈ 50 nm, which is below the resolution limit. Also, in our modeling of the inspection process, the effective signal is derived from a 2×2 pixel convolution of the raw camera image raising the effective inspection pixel size to 50 nm. When the camera pixel size is smaller than 25 nm, the defect intensity distribution is larger than the effective pixel size. Therefore, increasing pixel size also leads to increased peak signal. When the pixel size becomes larger than 25 nm, the convolved area is larger than the defect intensity distribution and lowers the defect signal.

As shown in Fig. 3.22c, the impact of the phase associated with the pattern defect causes asymmetric through-focus defect SNR. The best focus position is defined as the position that has minimum speckle contrast, as shown in Fig. 3.21. Defocus position = +100 nm (image closer to the lens) has a smaller defect SNR compared with the other 2 cases of best focus and defocus of −100 nm. The asymmetric behavior is the limiting factor on the defect SNR performance if the inspection tool is operated near the best focus position.

3.4.3 Defect signal vs. speckle noise and camera noise under various pixel sizes and defocus positions

The dark current in the CCD camera is a primary noise source that impacts the defect SNR. For this analysis, the camera noise is assumed to be a constant with varying pixel sizes. As shown in Fig. 3.23a, the defect SNR at various pixel sizes drops significantly and the trend is quite different compared with the previous case of speckle noise only. The reason is that the speckle noise, caused by the phase-dominated mask surface roughness at best focus under our illumination and optic settings (bright field), is much smaller than the camera noise. The RMS of the camera noise is 12 (unit:$\sqrt{Photons}$) while the speckle noise at best focus is only 5.5 (unit:$\sqrt{Photons}$). Therefore, the noise term in Eq. 3.2 is dominated by a constant camera noise and the overall trend of defect SNR is determined by the defect signal: smaller signal strength with an increase in pixel size. Figure 3.23b shows the result at various defocus positions. The results from the best focus and defocus position = −100 nm have similar defect SNR trend while defocus position = +100 nm has smaller defect SNR performance. The best focus position is again defined as the position that has minimum speckle contrast, as shown in Fig. 3.21.

3.4.4 Defect signal vs. speckle noise, camera noise, and photon shot noise under various pixel sizes and defocus positions

Next, the impact of photon shot noise, originating from the defect signal and background pattern intensity is considered. With a fixed photon density (source power), larger pixel size means more photons in a single pixel. For defect signal strength, this means that

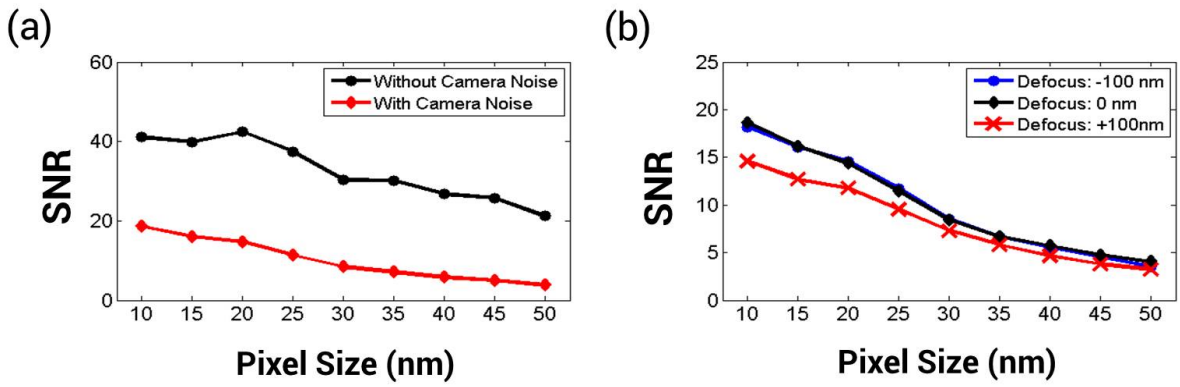

Figure 3.23: (a) Defect SNR under various pixel sizes. Defect signal, speckle noise and with or without camera noise are taken into the defect SNR calculation. (b) Defect SNR under various pixel sizes at different defocus positions: Defocus position = −100 nm, 0 nm, and +100 nm. Photon levels: 1000 photons/pixel, photon shot noise is not included for defect SNR calculation. Defect Type: Dense line intrusion defect with a size $\approx 26 \times 26$ nm^2 on the mask. The best focus position is defined as the position has minimum speckle contrast, as shown in Fig. 3.21.

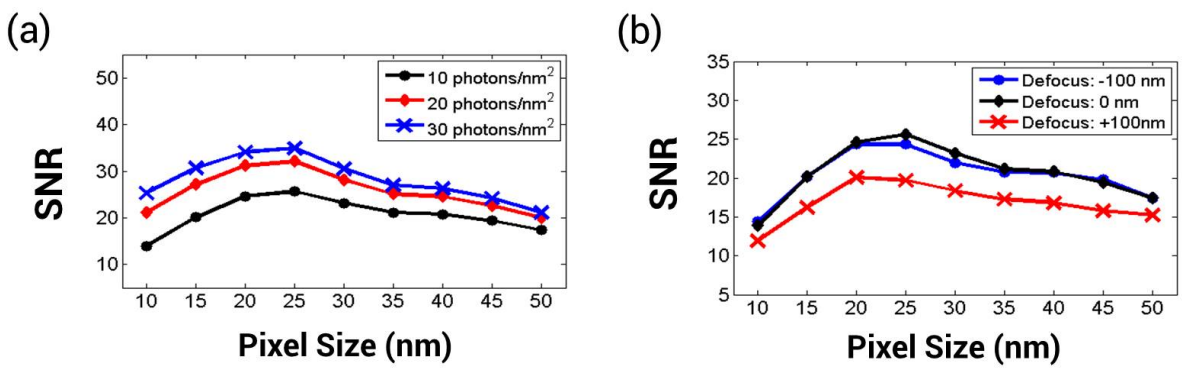

Figure 3.24: (a) Defect SNR under various pixel sizes and photon densities: 10, 20, and 30 photons/nm^2. Defect signal, speckle noise, camera noise, and photon shot noise are taken into the defect SNR calculation. (b) Defect SNR under various pixel sizes at different defocus positions: Defocus position = −100 nm, 0 nm, and +100 nm. Photon density: 10 photons/nm^2. Defect Type: Dense line intrusion defect with a size $\approx 26 \times 26$ nm^2 on the mask. The best focus position is defined as the position has minimum speckle contrast, as shown in Fig. 3.21.

the signal strength in number of photons is larger simply by virtue of increasing the pixel size. However, the corresponding photon shot noise ($\sqrt{\text{Photons}}$) from both defect signal and pattern background intensity increases as well. The interaction between defect SNR and pixel size under fixed photon density is shown in Fig. 3.24a. There exists an optimum pixel size to maximize the defect SNR under fixed photon density. This is due to the fact that the growing defect signal strength is compensated by the increase of photon shot noise. Moreover, under fixed pixel size, the defect SNR improvement is smaller as photon density increases. When pixel size is 25 nm, the defect SNR improves 25% with a 2× increase of photons per pixel from 10 to 20 photons/nm^2. However, the defect SNR only improves 8% with a 1.5× increase of photons per pixel from 20 to 30 photons/nm^2.

Figure 3.24b shows the result at various defocus positions when all the noise terms in the SNR calculation are included, as shown in Eq. 3.2. Under fixed photon density, there is an optimum pixel size to reach the highest defect SNR. Moreover, due to the asymmetric impact of defocus, defocus position = −100 nm and best focus position have similar defect SNR performance and defocus position = +100 nm has the smallest defect SNR.

3.4.5 Critical defect case study and how to improve the defect SNR for limiting case

Based on the results shown in the previous sections, the defect SNR performance is calculated for defects that cause 10% CD variation on the pattern aerial image. To determine the critical defects for dense line, iso-line, and dense contact patterns, projection lithography tool imaging parameters are used, as opposed to the inspection mode parameters described in the introduction. For inspection mode, the major goal is to identify the defect efficiently, thus simplified illumination condition and high NA optical system are used. On the other hand, printing mode is set to print various desired patterns uniformly, thus different customized illumination settings are used for different pattern designs. In this section, the projection lithography tool imaging parameters include an NA of 0.33 and dipole illumination with a sigma value between 0.2 and 0.9 with 90° opening angle for dense line pattern, disk illumination with a sigma value 0.5 for iso-line pattern, and quasar with a sigma value between 0.2 and 0.9 with 45° opening angle for contact pattern.

Table 3.2 shows the critical defect for each situation. The smallest critical defect is the extrusion defect for the iso-line pattern, which is $\approx 13 \times 13$ nm^2 on the mask. Figure 3.25 shows the critical defect SNR results under various pixel sizes and photon densities with defocus position = +100 nm, which was the worst case studied above. As shown in Fig. 3.25b, the extrusion defect SNR is in the range of 3 to 7 no matter the pixel size and photon density. This defect would be the limiting case of all critical defects since it has the smallest defect SNR and thus the smallest capture rate.

Figure 3.26 shows the iso-line extrusion critical defect through-focus SNR result, with pixel size and photon density of 30×30 nm^2 and 50 photons/nm^2 respectively. Precise defocus range control is needed to reach the desired defect SNR since the defect SNR is sensitive to

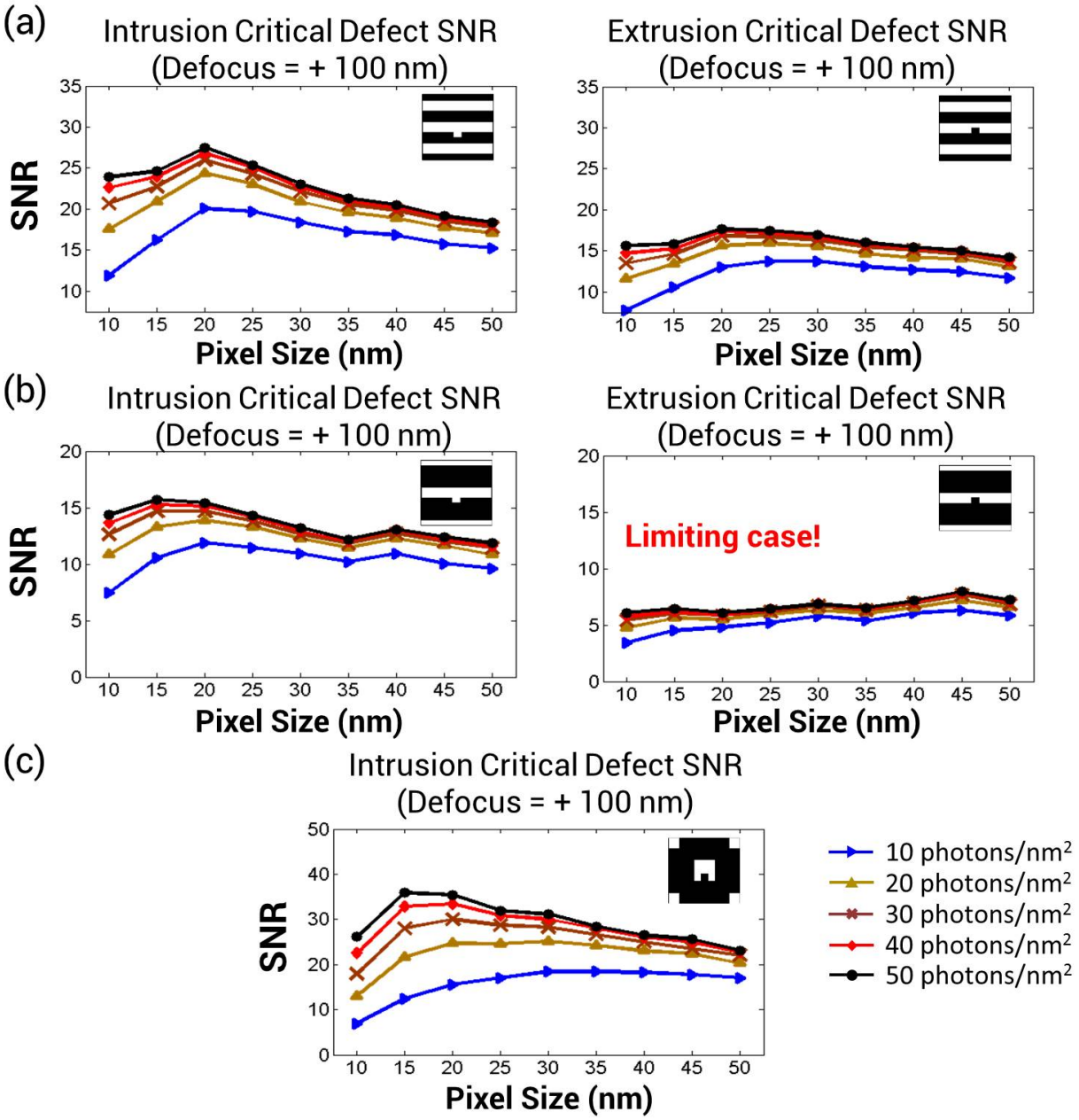

Figure 3.25: Critical defect SNR at defocus position = +100 nm for various patterns: (a) Dense Line (b) Iso-Line and (c) Dense Contact. Legends in (c) indicate the photon density level for each curve, ranging from 10 to 50 photons/nm^2. The best focus position is defined as the position has minimum speckle contrast, as shown in Fig. 3.21.

Pattern Type	Defect Type	size (nm^2)
Dense Line	Intrusion	25.6×25.6
	Extrusion	19.2×19.2
Iso Line	Intrusion	19.2×19.2
	Extrusion	12.8×12.8
Dense Contact	Intrusion	16×16

Table 3.2: Critical defect size for different pattern designs.

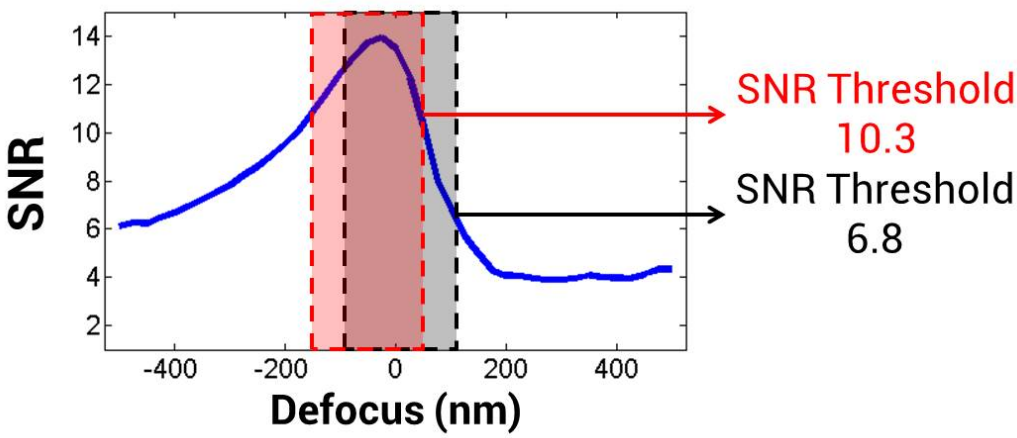

Figure 3.26: Defect SNR through-focus behavior for iso-Line extrusion critical defect. Pixel size: 30×30 nm^2. Photon density: 50 photons/nm^2. Defocus range: ± 500 nm. Blue box: Defocus range: -100 nm $\sim +100$ nm. Red box: -150 nm $\sim +50$ nm. The best focus position is defined as the position has minimum speckle contrast, as shown in Fig. 3.21.

the defocus position, as shown in Fig. 3.26. Moreover, the defect signal and speckle noise both have an asymmetric through-focus behavior due to the phase effects of EUV mask. For the iso-line extrusion critical defect, $SNR_{min} = 6.8$ at defocus position $= +100$ nm. However, if a nominal defocus of -50 nm is introduced to operate the inspection tool in a defocus range: -150 nm $\sim +50$ nm. With this new setting, $SNR_{min} = 10.3$ at defocus position $= +50$ nm, a 50% improvement in SNR. Moreover, it is interesting to note that the new best focus position (defocus $= -50$ nm) of the inspection tool corresponds to neither the maximum aerial image contrast nor minimum speckle contrast.

3.4.6 Comparison between the conventional bright field method and the optimum phase shift method on pattern defect SNR

As shown in the previous Section 3.3, the optimum phase shift method can improve pattern defect signal strength. In this section, the critical defect SNR calculation based on Eq. 3.2 using the optimum phase shift method is presented and compared with the bright field result.

Figure 3.27 shows the behavior of defect signal, speckle noise, and SNR under various phase shifts and apodization conditions. The defect SNR result shows that even though apodization can lower the impact of speckle noise, the defect signal is reduced simultaneously and results in lower defect SNR. On the other hand, phase shift is a better way to improve the defect SNR by utilizing the different behaviors between defect signal and speckle noise.

However, photon density can change the impact of the optimum phase shift method, as shown in Fig. 3.28. At higher photon density, defect SNR variation is even more sensitive to the phase shifts in the pupil plane. A 35% defect SNR reduction is observed as the phase shift in the pupil plane increases from 0° to -90° at 50 photons/nm^2, while the defect SNR variation is down 20% under the same phase shift variation condition at 10 photons/nm^2. The difference is due to variation in the relationship between defect signal shot noise, speckle noise, and camera noise as photon level increases.

Figure 3.29a shows the defect SNR enhancement relative to the bright field method among the critical defects listed in table 3.2. The optimum condition is chosen to maximize the smallest defect SNR among the critical defects. However, the impact of the optimum phase shift method on SNR is only in a range between $0\% \sim 7\%$ compared to the bright field method with optimized defocus. The improvement raises to $0\% \sim 9\%$ if different phase shifts and apodization conditions are adopted for each critical defect, as shown in Fig. 3.29b. The result shown here indicates that even though the optimum phase shift method can improve the absorber defect signal, it has only minor impact on the overall SNR when various noise sources are considered. It is not clear that this small change in SNR performance would warrant the increase in complexity that implementing the optimal phase shift method in an EUV patterned mask inspection tool would present.

3.5 Conclusion

In Section 3.2, the multilayer defect detection sensitivity on EUV patterned mask while using the Zernike phase contrast method was studied. The multilayer defect signal improvement is compensated by the overlap with the pattern. but the defect signal through-focus behavior remains the same. Moreover, the application of the Zernike phase contrast method is extended to not just phase defects, but also to absorber defects. When considering both types of defect, an optimum phase shift can be used in the pupil plane, instead of the conventional value ($\pm 90^\circ$), to improve the combined defect detection sensitivity.

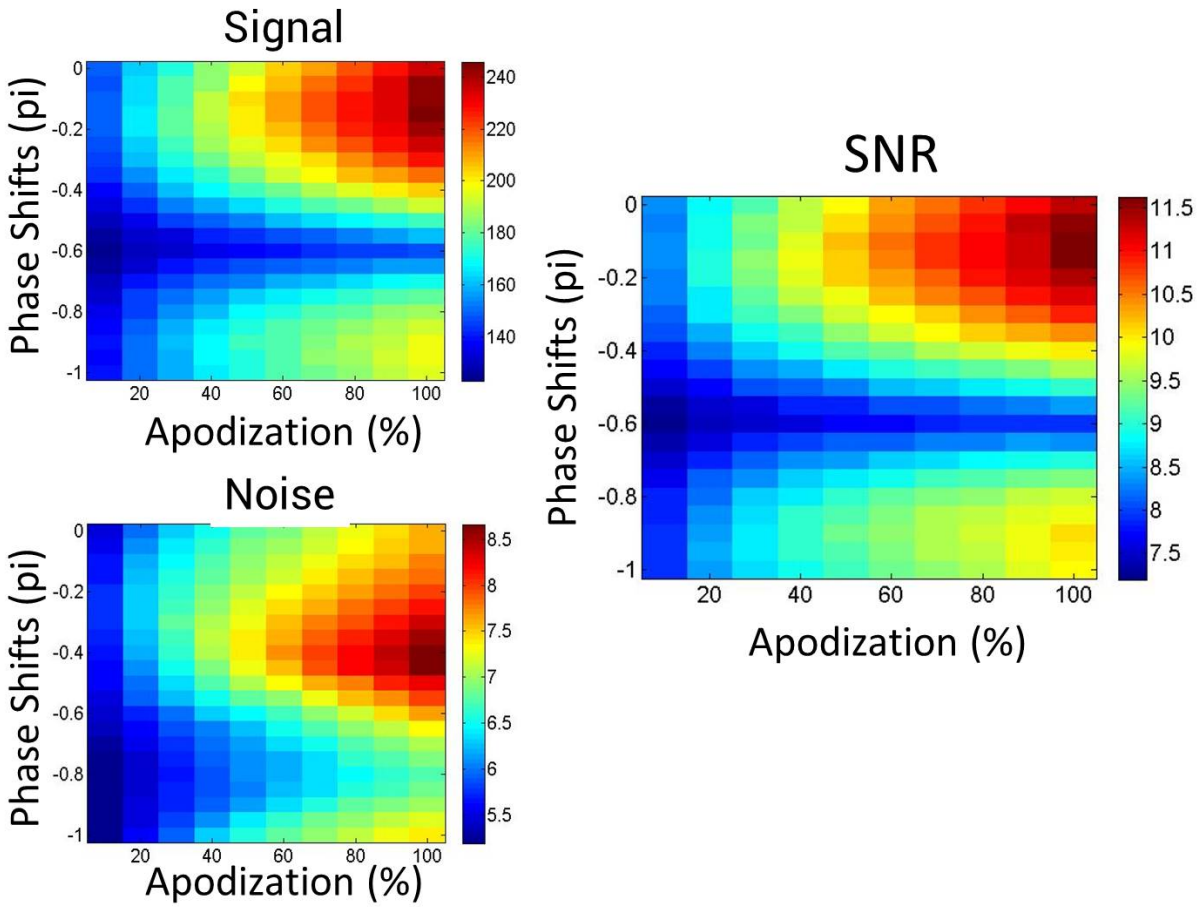

Figure 3.27: (a) Defect signal at best focus under different phase shifts and apodization conditions. (b) Speckle noise at different phase shifts and apodization conditions. (c) Defect SNR at best focus under different phase shifts and apodization conditions. Phase shifts range: $0 \sim -180°$. Apodization range: $10\% \sim 100\%$ bright field intensity transmission. Defect Type: Dense line intrusion defect with a size $\approx 26 \times 26$ nm^2 on the mask. Photon Density: 10 photons/nm^2. Pixel size: 10 nm in mask scale. The best focus position is defined as the position has minimum speckle contrast, as shown in Fig. 3.21.

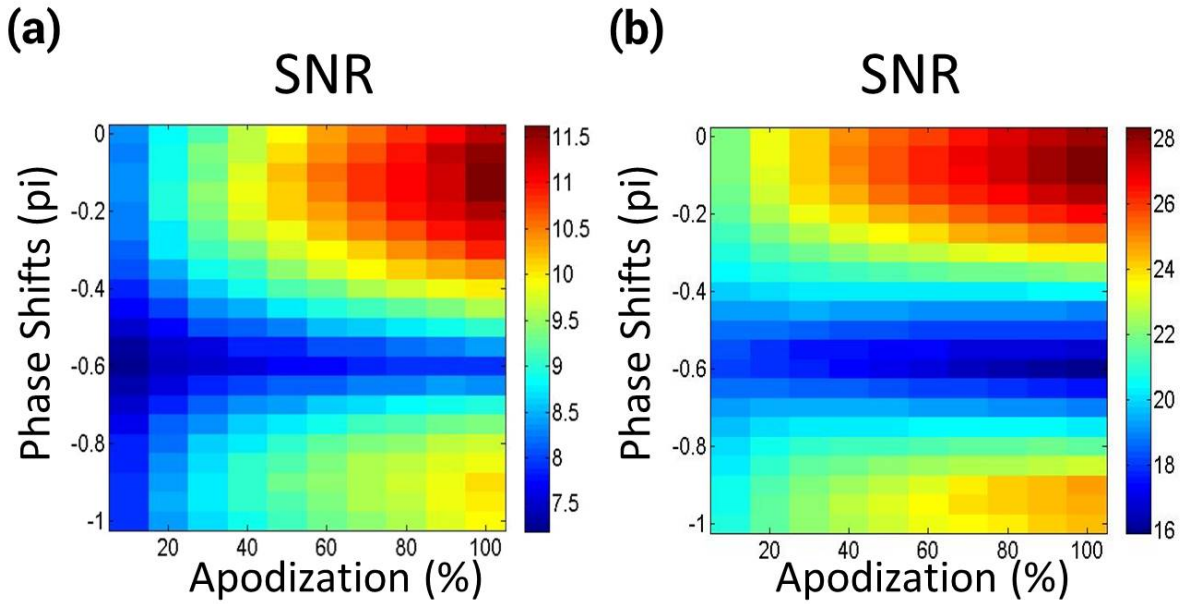

Figure 3.28: Defect SNR at best focus under different photon density: (a) 10 photons/nm^2. (b) 50 photons/nm^2. Phase shifts range: $0 \sim -180°$. Apodization range: $10\% \sim 100\%$ bright field intensity transmission. Defect Type: Dense line intrusion defect with a size $\approx 26 \times 26$ nm^2 on the mask. Pixel size: 10 nm in mask scale. The best focus position is defined as the position has minimum speckle contrast, as shown in Fig. 3.21.

The impact of illumination, material, and defect size on the pattern defect through-focus behavior was analyzed to discuss the phase effects of EUV mask pattern defects in Section 3.3. Illumination has different impacts on intrusion and extrusion defect signal strength. Moreover, the material-induced phase due to the difference in absorber refractive index from air can cause energy confinement/consumption and accumulate phase at the defect region. The phase effects of pattern defect increase the defect signal strength and affect the peak defect signal position, while defect size only changes defect sensitivity and not through-focus behavior. With alternative absorber materials, the defect behavior can be changed by reducing the phase effects using stronger absorption or n closer to 1. By adding an optimum phase shift to the pupil plane to form strong interference between the background and the pattern defect scattered light, the defect signal at best focus can be improved. For example, a 29% defect signal enhancement at the focus on a TaN-based 8×8 nm^2 intrusion defect is achieved using a $-54°$ phase shift.

For the bright field patterned mask inspection tool design study, the impact of various noise sources and the optical design on defect SNR was discussed in Section 3.4. The simulation results indicated that signal drops faster than speckle noise as pixel size increases

(a)

Pattern/Defect	SNR Bright field	SNR Optimum Phase Shifts	Δ(%)
Dense Line Extrusion	40.6	40.7	+0%
Dense Line Intrusion	33.47	36.1	+7%
Iso-Line Extrusion	25.57	25.73	+0%
Iso-Line Intrusion	15.6	16.3	+4%
Dense Contact Intrusion	32.2	33.4	+3%

(b)

Pattern/Defect	SNR Improvement (%)	Optimum pupil setting (Phase shifts / Apodization)
Dense Line Extrusion	+0%	0°/100%
Dense Line Intrusion	+9%	-18°/100%
Iso-Line Extrusion	+0%	0°/100%
Iso-Line Intrusion	+4%	-9°/100%
Dense Contact Intrusion	+9%	-36°/100%

Figure 3.29: (a) The list of critical Defects SNR at best focus using the optimum phase shift method and the enhancement relative to the bright field method. The phase shift and apodization condition is chosen to maximize the smallest defect SNR among the critical defects. (b) The maximum SNR enhancement at best focus relative to the bright field method for the critical defects and its corresponding phase shift and apodization condition. Photon density: 20 photons/nm^2. Pixel size: 30 nm in mask scale. Critical defect size is listed in table 3.2. The best focus position is defined as the position has minimum speckle contrast, as shown in Fig. 3.21.

due to the resolution limit of the defect aerial image intensity distribution. The simulation results also showed that even though larger pixels can lead to more photons per pixel under fixed photon density (source brightness), the defect SNR is smaller due to the increase of both defect signal and photon shot noise ($\sqrt{\text{Photons}}$) from the defect signal and the background pattern intensity. The improvement of defect SNR by increasing photon density at a fixed pixel size also saturates for the same reason. The asymmetric impact of defocus reduces the defect SNR_{min} when operating at a defocus position > 0. In the critical defect case study, the simulation results showed that the smallest critical defect has a narrow defocus range to operate at high defect SNR ($\text{SNR} \geq 10$), and a focus offset is required to achieve this. A 50% improvement in SNR_{min} can be achieved by introducing a -50 nm nominal defocus into the inspection system. Comparison between the bright field method and the optimum phase shift method showed that even though the optimum phase shift method can improve the defect signal, the defect SNR improvement is not significant when all of the noise sources are included.

Chapter 4

Impact of Extreme Ultraviolet Sub-resolution Assist Feature (SRAF) on Bossung Tilt and Process Window Enhancement

4.1 Background

As lithography technology improves to print smaller features, the finite height of the mask pattern becomes significant compared to the wavelength of the light. For DUV lithography, the absorber thickness on the mask is ≈ 80 nm while the wavelength of the light is 193 nm, and the illumination angle expands to $\pm 16.5°$ due to the increase of NA to 1.35 by immersion lithography. The comparable size between light, the mask feature, and off-axis illumination renders the thin mask approximation invalid for the calculation of the aerial image from the mask. Mask 3D (M3D) effects can result in asymmetric process window, H-V bias, and polarization induced astigmatism in DUV lithography [10, 50, 51].

EUV M3D effects have an even more profound impact on imaging performance compare to the case for DUV lithography. The absorber thickness is still around 80 nm while the wavelength of the light is reduced to 13.5 nm. The impact of off-axis illumination is deteriorated due to the 6° chief ray angle (CRA) for the EUV lithography, as shown in Fig. 4.1. Moreover, the material-induced phase shift due to the Ta-based absorber material system also introduces an intrinsic aberration to the imaging process.

To address these issues, extensive studies have been focused on identifying the origin of the M3D effects [10, 41, 51, 52]. Moreover, various solutions have been proposed: absorber thickness or material optimization to reduce the shadowing effect [13, 43], source mask optimization to balance the intensity contribution from each illumination pole [11], etched multilayer mask to reduce the double diffraction between the absorber and the multilayer mirror [53], and sub-resolution assist features (SRAFs) to mitigate the Bossung tilt [12]. The

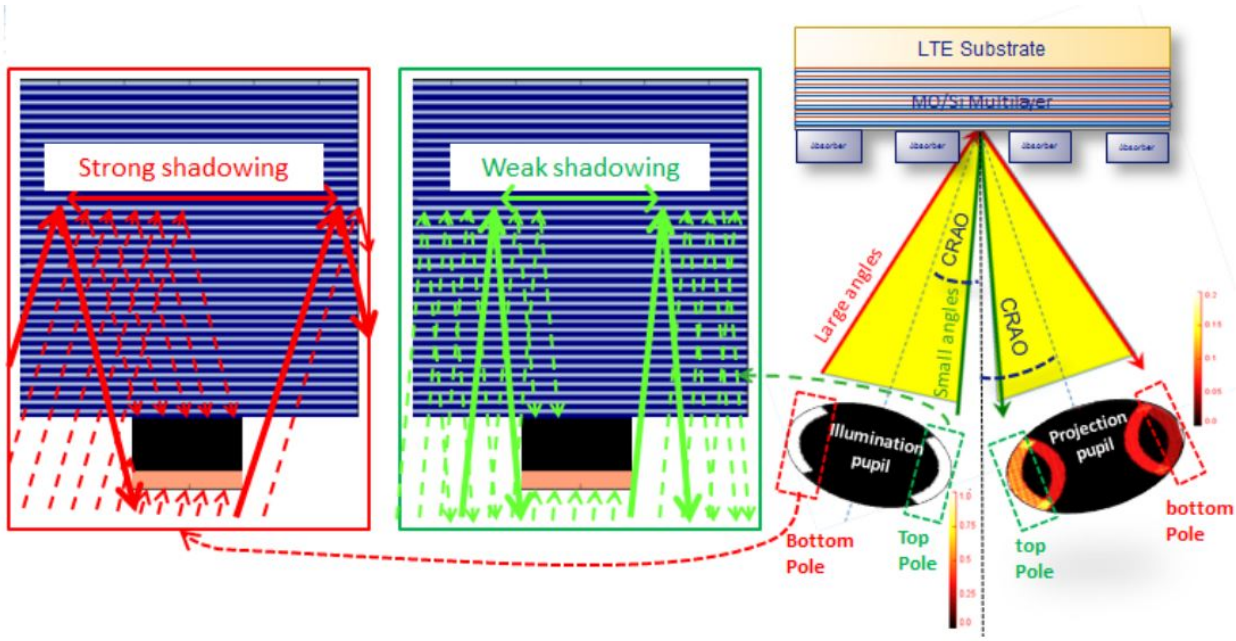

Figure 4.1: Schematic diagram of the origin of the EUV mask 3D effects [12].

semiconductor industry has used SRAF as a resolution enhancement technique for isolated features in DUV lithography. With symmetric SRAFs placement, the isolated pattern has a similar Bossung curve behavior as the dense pattern thereby increasing the overlapped process window. The interaction between the main feature and the SRAFs can compensate the scattering light-induced aberration to reduce the M3D effects. However, the EUV SRAFs studied in Ref. [12] show that along the shadowing direction (horizontal), asymmetric SRAFs pattern placement can be used to compensate the M3D effects and improve the process window. This counter-intuitive result from EUV SRAFs needs to be studied.

In this chapter, physical insight into the optical mechanisms at play enabling the M3D effect-mitigation by asymmetric SRAF distribution is presented. Rigorous 3D modeling is used to study in detail the printing of a semi-isolated 2-bar pattern with a pitch of 160 nm and ideal 2 point-source dipole illumination. By analyzing the scattered order distribution in the pupil plane from each pole, the impact of scattered electric field at various ray angles with or without SRAFs is studied. The simplified illumination condition also makes it easier to identify the contribution from each pole to the overall aerial image and its corresponding impact on Bossung curve.

4.2 Simulation settings and parameters

In this study, rigorous 3D mask modeling with the Fourier boundary condition is used to model the lithography aerial image [42]. For the mask, 40 pairs of Mo/Si multilayer and a

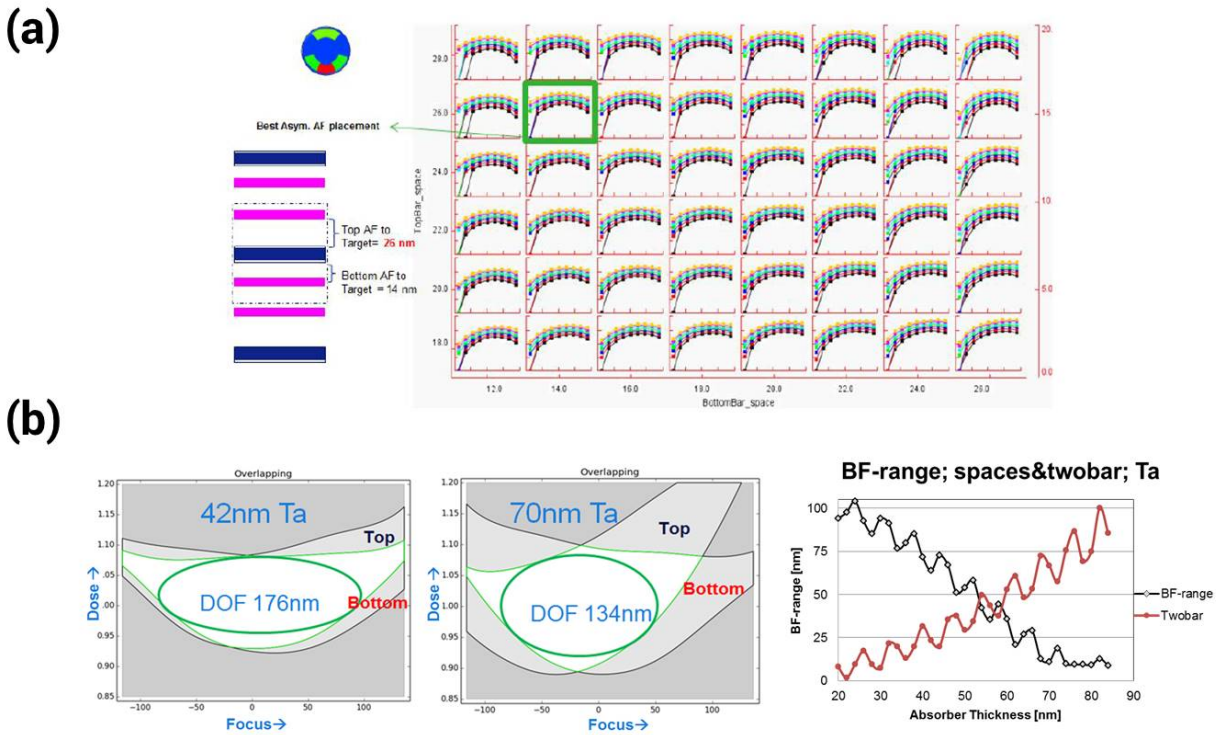

Figure 4.2: Proposed solutions for EUV mask 3D effects: (a) Use SRAFs [12]. (b) Reduce absorber height [13].

70 nm standard Ta-based absorber material are used for simulation. The mask pattern is an isolated dark field 2-bar 16 nm feature along the shadowing direction (horizontal) with an 8 nm SRAF. Figure 4.3a shows the mask design with and without SRAF. Main feature bias and SRAF displacement are optimized to make the aerial image print at the target CD of 16 nm. As shown in Fig. 4.3b, a delta function dipole illumination with offset values of ± 0.9 sigma and a NA of 0.33 is used for imaging settings. Dipole illumination is not the conventional illumination setting to print isolated features, but its simplicity is useful in providing valuable insight into the impact of SRAF on Bossung tilt.

The purpose of the SRAFs studied here is to remove the Bossung tilt. A hypothetical Bossung plot with and without tilt is shown in Fig. 4.4. The metric used in this study is the net CD offset between the -60 to $+60$ nm defocus positions at nominal threshold (dose). For our illumination settings, the depth of focus is ≈ 60 nm. The tilt is of interest because it is a good indicator of the overall process window performance.

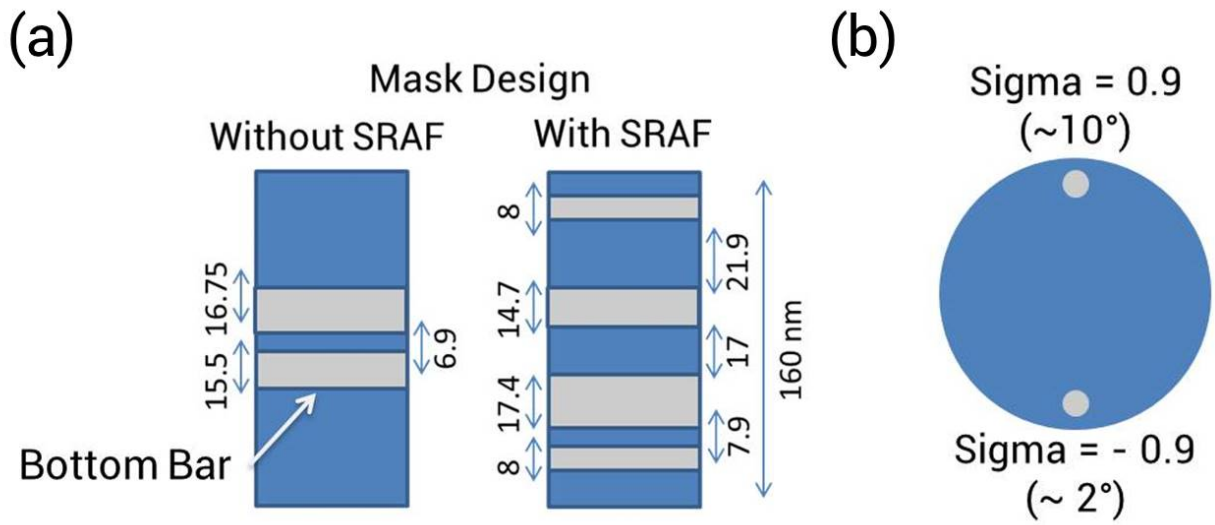

Figure 4.3: Schematic diagram: (a) Semi-isolated 2-bar mask design for without or with SRAF situation. All dimensions are in wafer scale. (b) Illumination setting used in the study. Angle indicated in the parenthesis is its corresponding CRA for each pole.

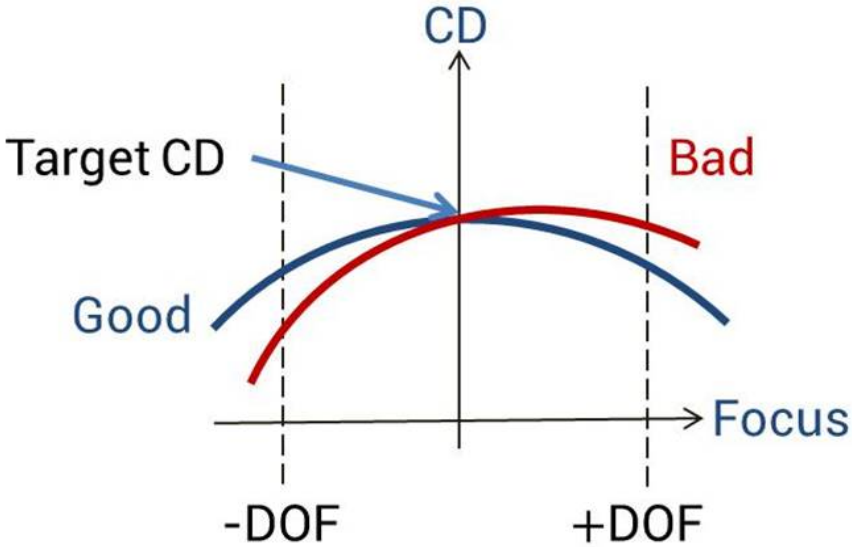

Figure 4.4: Bossung tilt definition. Blue curve indicates a balanced Bossung curve which results in larger process window while red curve indicates an imbalanced Bossung curve which results in smaller process window.

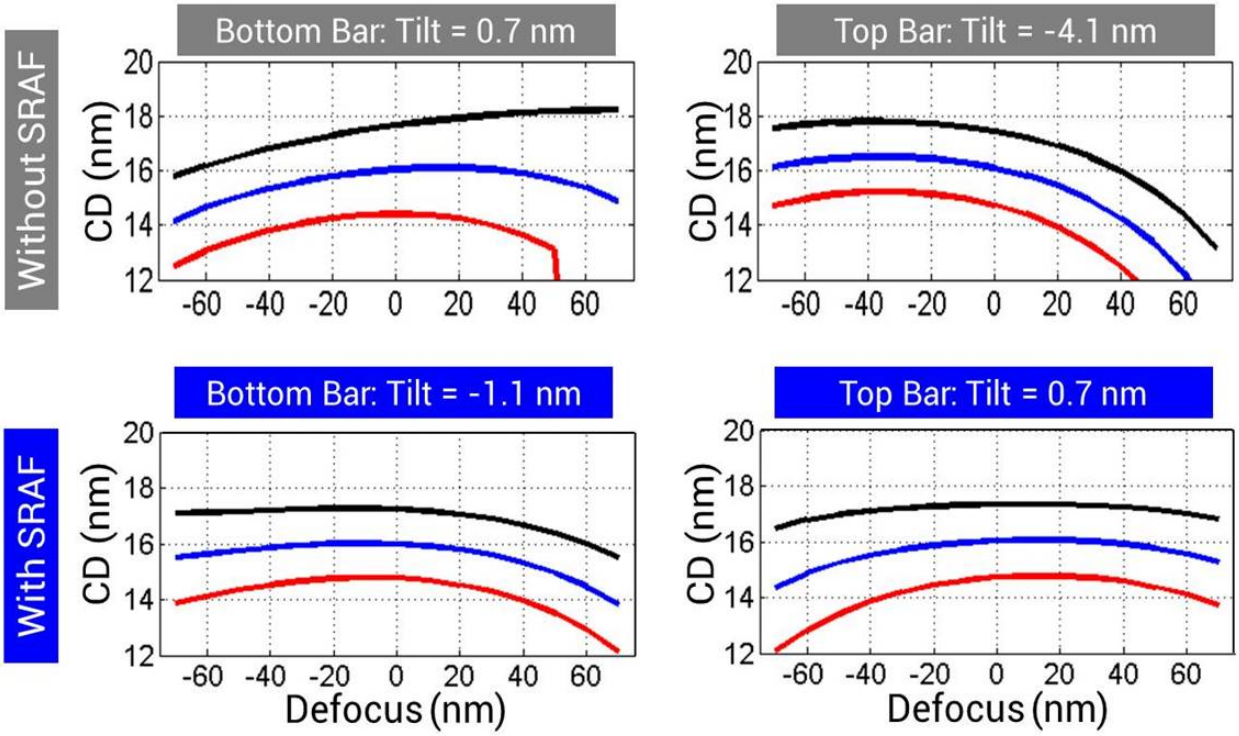

Figure 4.5: Bossung curves for without or with SRAF situations. Left: Bottom bar. Right: Top bar. Each curves represent different doses: Black (0.9×Threshold), blue (1.0×Threshold), and red (1.1×Threshold).

4.3 Bossung curves, scattered orders, and aerial images analysis

Figure 4.5 shows the Bossung curve results for both bars from each mask design. Without SRAFs, the bottom bar has +0.7 nm tilt and the top bar has −4.1 nm tilt. With SRAFs, the bottom bar has −1.1 nm tilt and the top bar has +0.7 nm tilt. More balanced Bossung curves show the benefit of including the asymmetric SRAFs into the design as expected.

To further understand the impact of asymmetric SRAFs in the imaging process, Figure 4.6 shows the scattered order distribution from each pole for both cases. Based on the NA and pitch of the pattern, only the scattered orders that pass through the pupil are included. The pole offset sigma = 0.9 case has smaller amplitude scattered orders compared with the pole offset sigma = −0.9. This discrepancy is due to the larger illumination angle ($\approx 10°$) for the positive pole leading to a stronger shadowing effect. Figure 4.6 also shows the phase of the scattered orders relative to the 0th order. Larger phase fluctuation is seen for both poles when the asymmetric SRAFs are included into the mask design. Sigma = −0.9 is dominated by coma (Z_7) and the sigma = 0.9 is dominated by spherical aberration (Z_9).

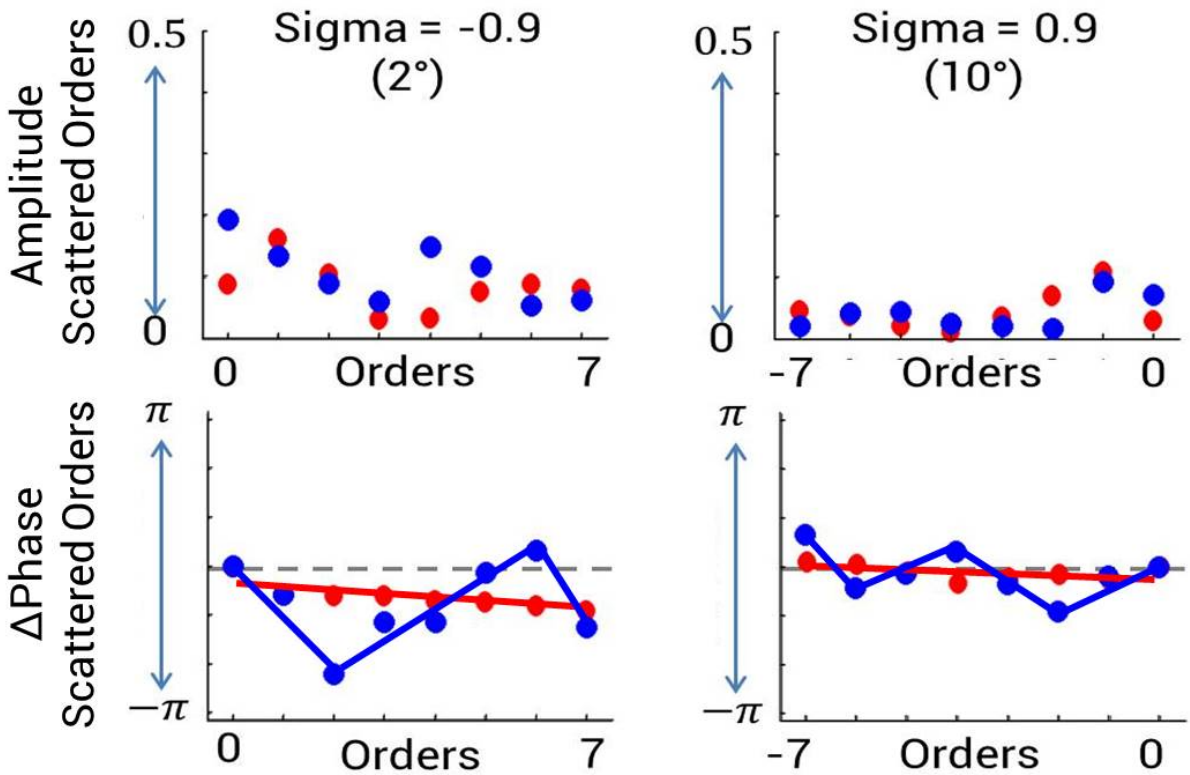

Figure 4.6: Scattered order distribution for each pole: Sigma = −0.9 (Left) and Sigma = 0.9 (Right) and different mask designs: Without SRAF (Red) and With SRAF (Blue). Phase of the scattered orders is relative to that of the 0th order for both cases.

The results counter-intuitively indicate that a larger effective aberration is introduced into the imaging system with the asymmetric SRAFs. From this perspective, the SRAF solution is quite different from the other proposed solutions for Bossung tilt mitigation. For example, reduced absorber height or alternative absorber material system mitigates the M3D effects by reducing the aberration induced by the phase-shifting absorber materials. With asymmetric SRAFs, stronger aberrations are introduced into the imaging system to mitigate the Bossung tilt.

Figure 4.7 shows the intensity distribution produced by each pole for the 2-bar pattern. The bottom bar on the left of the 2-bar image in Fig. 4.7 shows the contribution from the dipole illumination while top bar on the right of the 2-bar image in Fig. 4.7 is mainly dominated by the negative pole. This is due to the positive pole suffering from strong shadowing effect, as shown in Fig. 4.6. Therefore, the bottom bar Bossung curve behavior is determined by both illumination poles while the illumination pole with less shadowing effect (offset sigma = −0.9) determines the top bar Bossung curve behavior.

To understand the impact of each pole on the Bossung curve, Figure 4.8 shows the effec-

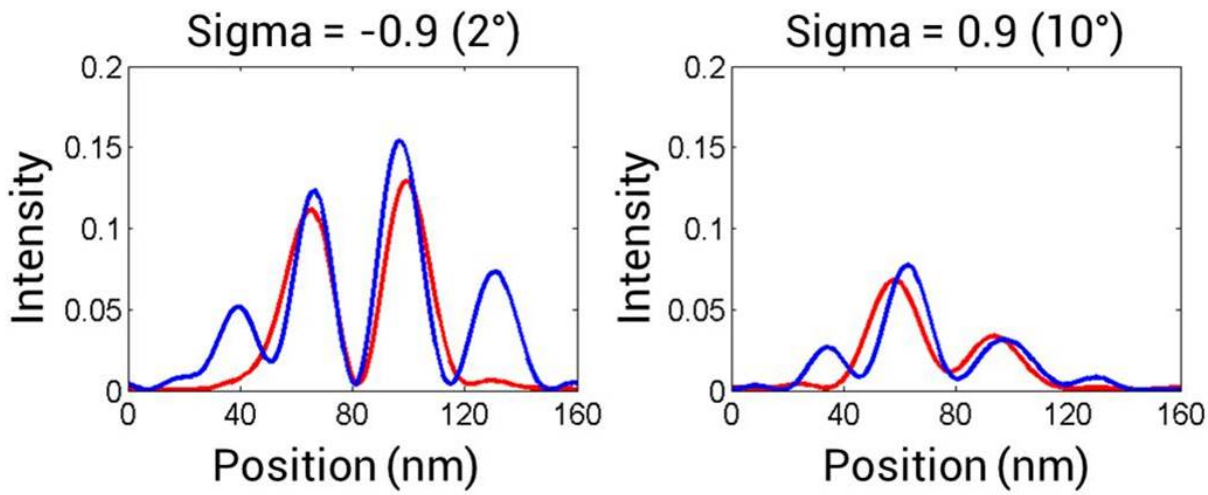

Figure 4.7: Aerial image contributed by each pole: Sigma = −0.9 (Left) and Sigma = 0.9 (Right), and with different mask designs: Without SRAF (Red) and With SRAF (Blue).

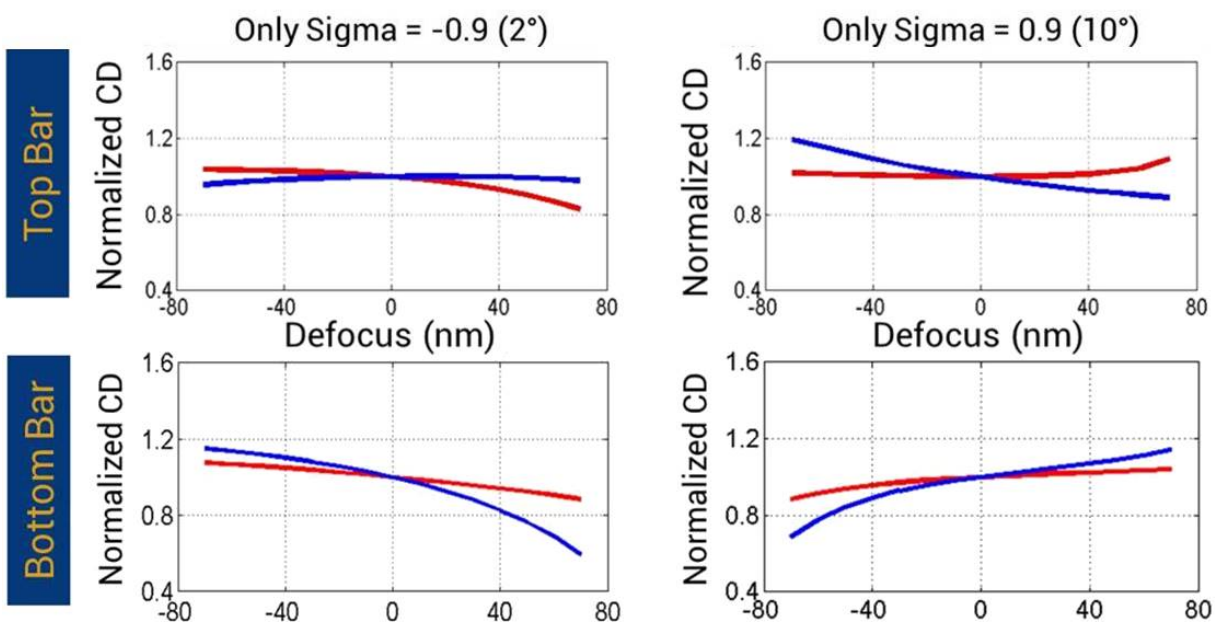

Figure 4.8: Effective CD variation for each bar by single pole: Bottom bar (bottom row) and top bar (top row) by single pole: Sigma = −0.9 (Left) and Sigma = 0.9 (Right), and with different mask designs: Without SRAF (Red) and With SRAF (Blue).

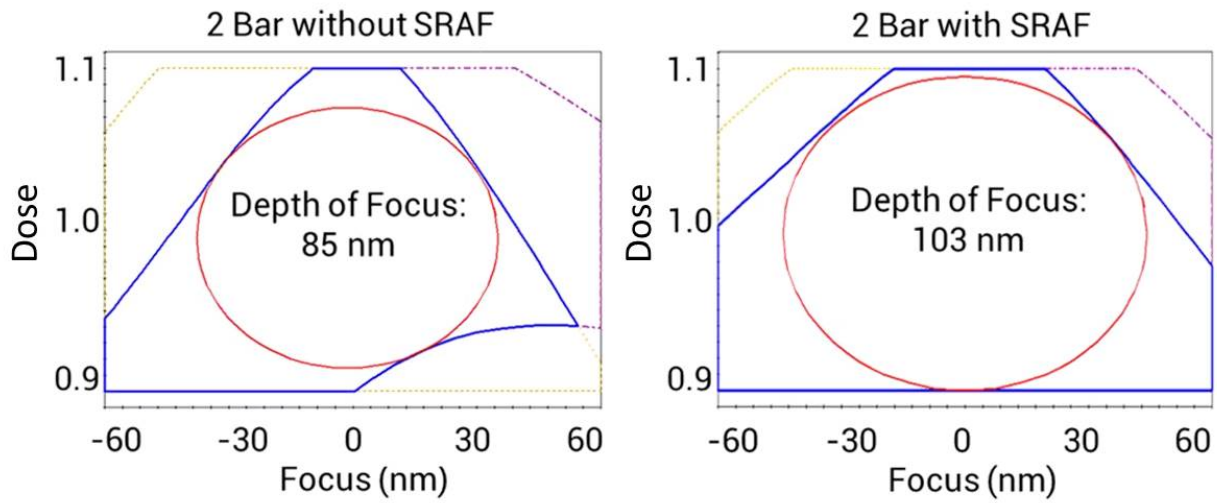

Condition	Bottom/Top Tilt (nm)	Overlap Process Window (nm)
No_SRAF	0.7 / -4.1	85 (Ref.)
With_SRAF	-1.1 / 0.7	103 (**+21%**)

Figure 4.9: Overlapping process window for 2-bar without and with asymmetric SRAFs. Table listed here shows the Bossung tilt result for each pattern design and its corresponding depth of focus of their process window.

tive through-focus CD variation for the 2-bar pattern from each pole. The same threshold condition for each pole has been applied to the CD variation calculation for each bar. For the bottom bar, each pole has a stronger but opposite tilt with the introduction of the SRAFs. This shows that even though stronger effective aberrations are introduced into the system, they are compensated by the dipole illumination which has opposite effect on the overall Bossung curve behavior. Thus a tilt variation from 0.7 nm to -1.1 nm is shown in Fig. 4.5. For the top bar, even though stronger tilt is observed from the positive pole, it has negligible influence to the Bossung curve due to its low-intensity contribution to the overall top bar image formation. The negative pole has a dominant impact on the top bar image and has a more balanced Bossung curve with the asymmetric SRAFs. As shown in Fig. 4.9, the overall process window is improved by 21% by adding asymmetric SRAFs.

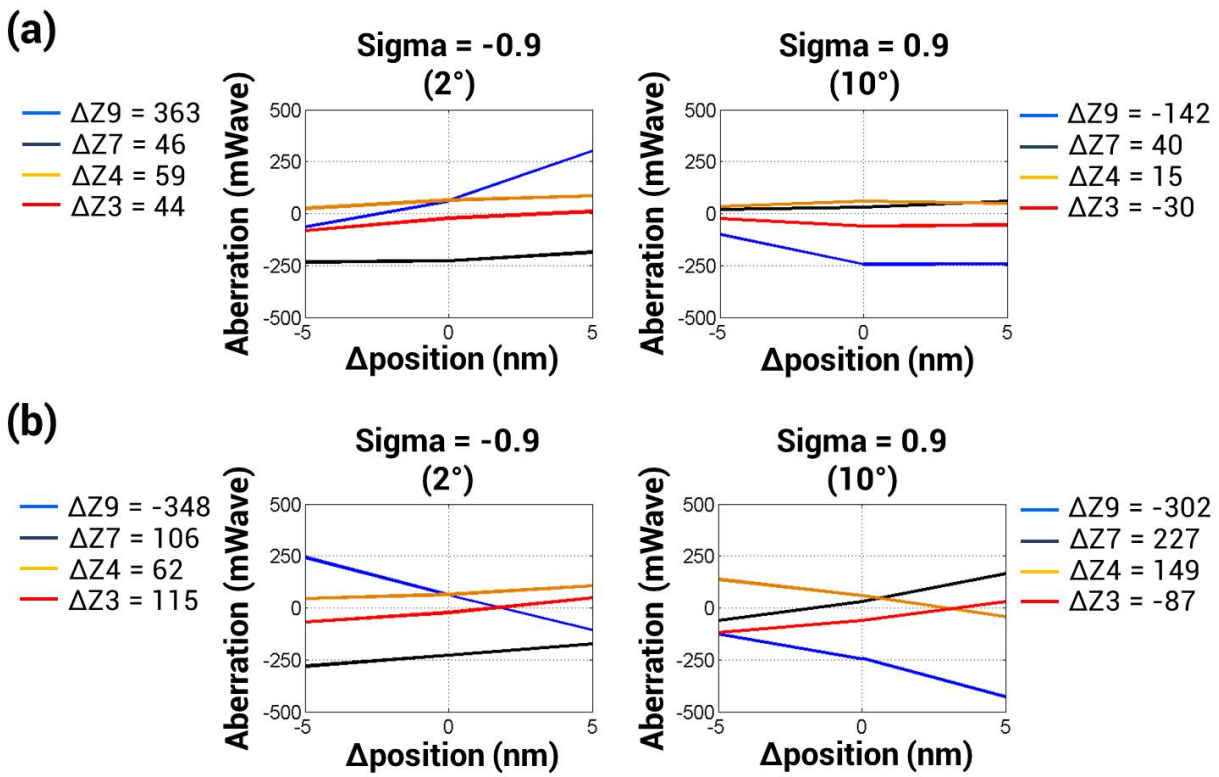

Figure 4.10: The aberration variation of each pole for different SRAFs: (a) Top SRAF, position < 0 means closer to the 2-bar feature. (b) Bottom SRAF, position > 0 means closer to the 2-bar feature. The number shows along side with the figure is the aberration variation represented by various aberration sources. Blue: Z_9 (Spherical), Black: Z_7 (Coma), Orange: Z_4 (Defocus), Red: Z_3 (Tilt).

4.4 Sensitivity of SRAF position on Bossung tilt

It is also interesting to note that the main feature has different sensitivities with respect to the position of each SRAF. Figure 4.10 shows the aberration variation from each pole as the bottom or top SRAF position is varied. The aberration is used to describe phase variation by fitting a set of Zernike polynomials to the phase of the scattered orders. As expected, the bottom SRAF has a stronger impact on the overall phase variation in the pupil plane than the top SRAF. A 10 nm difference in bottom SRAF position can cause a maximum 300 mWave aberration variation. The difference between two SRAFs can be attributed to the oblique illumination of EUV lithography, leading one of them to have a smaller contribution to the formation of the aerial image.

Figure 4.11 shows the impact of SRAF position on Bossung tilt. The bottom bar Bossung curve is only sensitive to the variation of its neighboring bottom SRAF position, while the

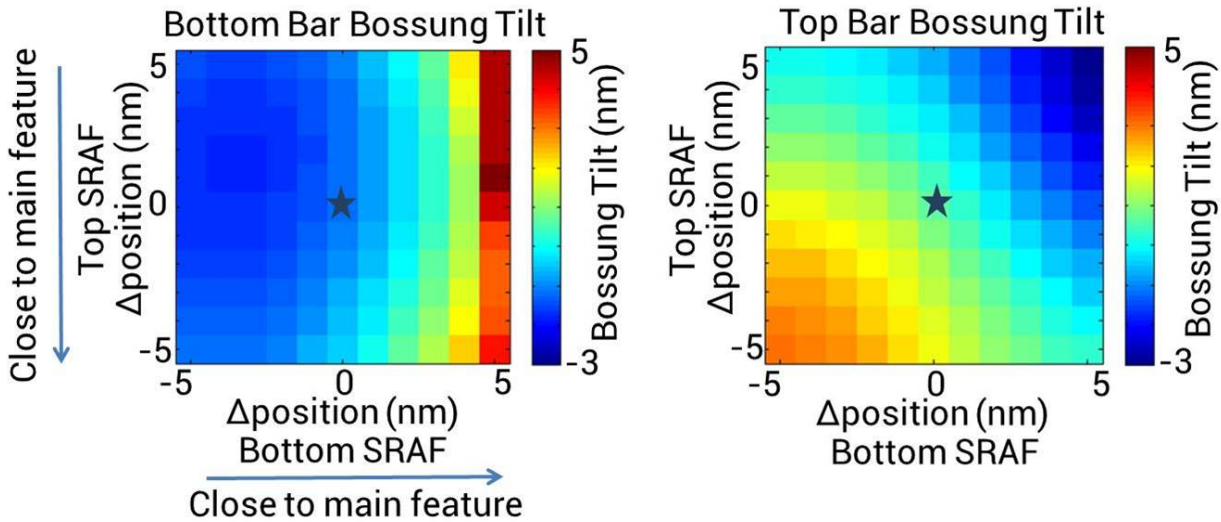

Figure 4.11: Bossung tilt variation for each bar under various bottom and top SRAF relative position. $(0, 0)$ indicates the default mask design shown in Fig. 4.3a.

top bar is sensitive to the position of both SRAFs. The results show the complex interaction between the 2-bar main feature and its corresponding SRAFs, and also the necessity to precisely control the SRAF position to achieve expected process window improvement.

4.5 Conclusion

In this chapter, a 2-bar pattern with and without SRAFs was used to gain physical insight into the optical imaging mechanism, which enables M3D effects mitigation by asymmetric SRAFs pattern placement. The delta function dipole illumination shows different shadowing effects on each pole due to the different illumination angles. This can result in different contributions to the overall image formation. The amplitude scattered orders from the high off-axis angle are shown to have a reduced magnitude, thus resulting in very poor single pole imaging of the top bar. Hence the image of the top bar is primarily contributed by the near-axis illumination pole. Moreover, the simulation results showed that unlike other proposed solutions for M3D effects, the asymmetric SRAF mask design introduces even stronger effective aberrations into the imaging system to balance the Bossung tilt. As a result, a 21% improvement on the depth of focus for the overall process window is achieved. Also, a systematic position sensitivity study showed the complex interaction between the main feature and the SRAFs. Different Bossung tilt sensitivities with respect to the relative positions between main feature and SRAFs are shown, thus indicating that different restrictions on SRAF position are necessary for the mask-making process.

Chapter 5

Efficient Fresnel Zoneplate Pattern Data Preparation for High-Resolution Nanofabrication

5.1 Motivation

The Fresnel zoneplate is an imaging element widely used by the x-ray and EUV community. In soft x-ray regime, the Fresnel zoneplate with a spatial resolution better than 15 nm enables the possibilities for biological imaging and material science studies into the sub-10 nm regime [54]. For EUV lithography mask inspection microscopy, Fresnel zoneplates provide the opportunity to have superior image resolution while at the same time a flexible optical design [31].

In the past, papers regarding high-resolution zoneplates have mostly focused on optimizing the fabrication process conditions, rarely mentioned the detail of their pattern data preparation algorithm [55, 56, 57]. This chapter is focused on the zoneplate pattern generation algorithm which can generate the desired zoneplate pattern and properly fracture it to a pattern file based on designed optical properties [58]. Figure 5.1 shows the general process flow of our algorithm.

In the first section, the generation of the target zoneplate pattern under various settings is described. Next, the rendering algorithm for the zoneplate pattern to meet fabrication requirement and optimize its file size and computation time is presented. The rendering discussion also includes a description of the method used to define the local dose and bias in the pattern facilitating fabrication control. Finally, a few fabrication examples using the new algorithm are presented.

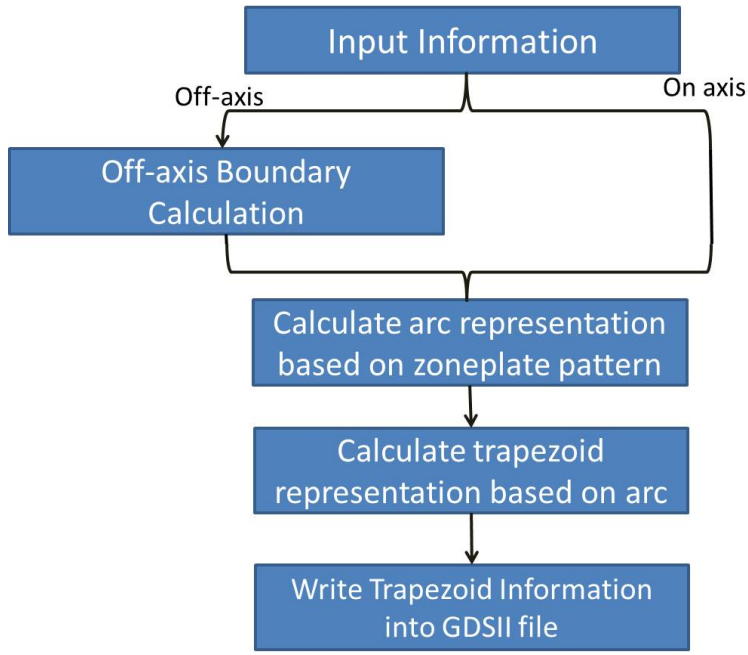

Figure 5.1: The process flow of the zoneplate pattern generation algorithm.

5.2 Background

Fresnel zoneplates are diffractive optics which consist of concentric rings (zones) to constructively interfere light at a specific focus position. The optical path difference (OPD) between any off-axis source point and the on-axis source point in the first zone is no more than half the wavelength ($\frac{\lambda}{2}$) to form constructive interference. For n^{th} zone, the generalized OPD must satisfy:

$$\frac{(n-1)\lambda}{2} < l_n - l_0 < \frac{n\lambda}{2} \tag{5.1}$$

If Eq. 5.1 is written in terms of source point radius (r_n), Equation 5.2 shows the desired radius (r_n) for n^{th} zone based on wavelength (λ), zone number (n), and focal length (f):

$$(n-1) \times \lambda \times (f + \frac{(n-1)\lambda}{4}) < (r_n)^2 < n \times \lambda \times (f + \frac{n\lambda}{4}) \tag{5.2}$$

The optical resolution (R) of a diffraction-limited optical system with a given wavelength (λ) and NA can be described as:

$$R = \frac{\lambda}{2NA} \tag{5.3}$$

For a Fresnel zoneplate, the outermost zone width (Δw) can be related to NA by considering its first order diffracted light angle (θ):

$$\sin(\theta) = \frac{\lambda}{p} = \frac{\lambda}{2\Delta w} \tag{5.4}$$

p is the pitch of the Fresnel zoneplate and for the binary zoneplate $p = 2 \times \Delta w$. Equation 5.5 shows that the outermost zone width determines the optical resolution of the zoneplate.

$$R = \frac{\lambda}{2NA} = \frac{\lambda}{2\sin(\theta)} = \frac{\lambda}{2} \times \frac{2\Delta w}{\lambda} = \Delta w \tag{5.5}$$

Moreover, the zone width is inversely proportional to the zone radius [58]. Thus the primary challenges in making a Fresnel zoneplate with prescribed focal length and optical resolution are placing the concentric ring structures in the designated locations and precisely controlling the width of the outermost zones.

For more exotic imaging modes, the zone position can be varied to get an OPD other than half a wavelength which is shown in Eq. 5.1 for wavefront control. The results can lead to a phase difference between the light passing through different region of the zoneplate. For apodization control, one can either vary the zone width or block part of the zone to control the diffraction efficiency of the zoneplate. The methods to achieve these features in our algorithm are detailed in the following section.

The next challenge is to translate the ideal arc-shaped zones into a format compatible with lithography machines which require polygon or trapezoid shapes. The trade-off between pattern file size, computation time, and prescribed optical tolerances needs to be considered in the generation of this machine-compatible format. Also, lithography-specific design features like the pattern and dose bias are needed along with the zoneplate pattern to improve pattern yield by optimizing the fabrication conditions. Conversion of the ideal zoneplate arcs to a machine compatible format is known as pattern data preparation.

5.3 Fresnel zone plate pattern generation

5.3.1 Zoneplate radii calculation algorithm

To calculate the zoneplate pattern, the zone radius at every point needs to be defined in order to determine its contour. Figure 5.2 shows the process flow to determine the zone radius based on zone number (n), object distance (p), image distance (q), wavelength (λ), and also the aberration/phase contrast condition using the Secant method. In numerical analysis, the secant method is the finite difference approximation of Newton's method for finding the zero crossing of a function.

Since the function used in the zoneplate is the OPD for the complete optical system, an initial guess is needed for the Secant method to determine the correct zone radius. Our algorithm starts with the assumption in the simple ideal circular zoneplate lens of Eq. 5.2.

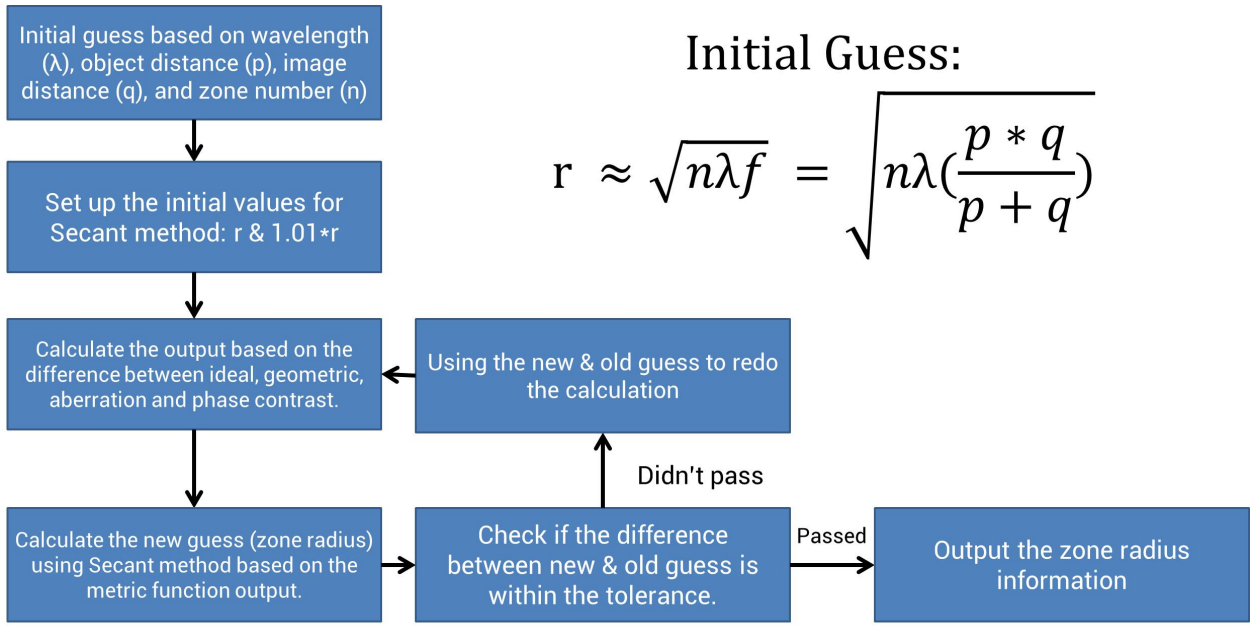

Figure 5.2: The process flow on how to decide the zone radius using Secant method based on the OPD from geometric, phase contrast, and aberration.

With this initial guess, the non-ideal OPD for the combination of geometry, aberration, and phase contrast are used to define a difference metric. The secant sequential iteration method is then used to sequentially find new roots (zero estimates) for this metric that converge to the spatial location on the zoneplate where the metric is zero.

$$\text{Metric} = (OPD_{geometric} + OPD_{aberration} + OPD_{phasecontrast}) - OPD_{zoneplate} \tag{5.6}$$

This algorithm enables the possibility of (1) Including arbitrary aberrations in the pattern calculation, and to (2) Determining the balance between precision in locating the zone and computation time.

5.3.2 Conventional on-axis zoneplate

The process flow to determine a conventional on-axis zoneplate pattern is shown in Fig. 5.3a. With design information like object distance, image distance, the NA and the wavelength, one can calculate the location, the width and the total number of zones based on the equations shown in the previous section. In order to describe the zoneplate pattern, an arc is used to represent each zone. Figure 5.3b shows the definition of the arc parameters for the zoneplate pattern representation. For a standard zoneplate, each zone can be represented by one arc with an opening angle ($d\theta$) equal to 360°. To enable exotic zoneplate patterns, the opening

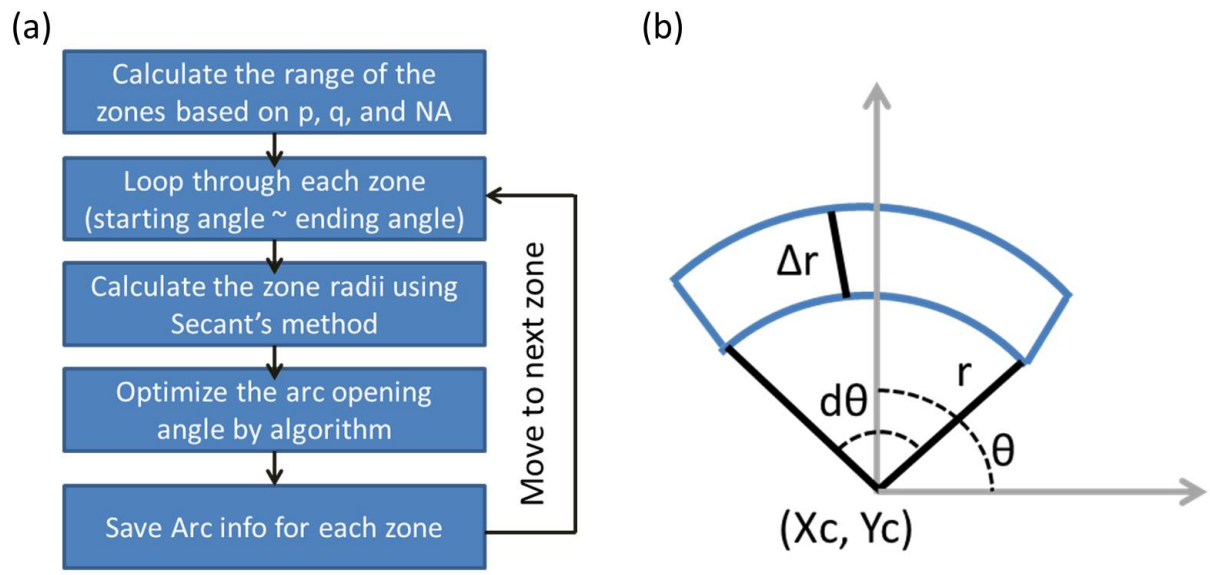

Figure 5.3: (a) The process flow to generate conventional on-axis zoneplate pattern. (b) Definition of arc parameters for zoneplate pattern representation. (X_c, Y_c, r, Δr, θ, $d\theta$) represents the center coordinates of the arc, arc radius, arc width, the starting angle of the arc, and the opening angle of the arc.

angle of each arc can be varied. The optimization algorithm is detailed in the following section.

5.3.3 Off-axis zoneplate

Off-axis zoneplates are needed for some specific applications like the SHARP EUV microscope at LBNL [58]. With off-axis zoneplates, the 1st order light can be separated from the 0th order light in angle space, facilitating the order sorting process. In our algorithm, there is an extra step for the off-axis zoneplate compared with the on-axis zoneplate. The opening angle for each zone has to be calculated first based on the user-defined boundary condition. Then, the zoneplate pattern can be generated in a manner similar to that used for generating a conventional on-axis zoneplate. Figure 5.4 shows the process flow for off-axis zoneplates and the GDSII (Graphic Database System) pattern image of an off-axis zoneplate on top of its parent on-axis zoneplate.

5.3.4 Tilted zoneplate

For tilted zoneplates, the zoneplate orientation is no longer normal to the optical axis, but each zone on the zoneplate still has to image the object to the same image plane position. Equation 5.7 shows the OPD calculation for a standard zoneplate:

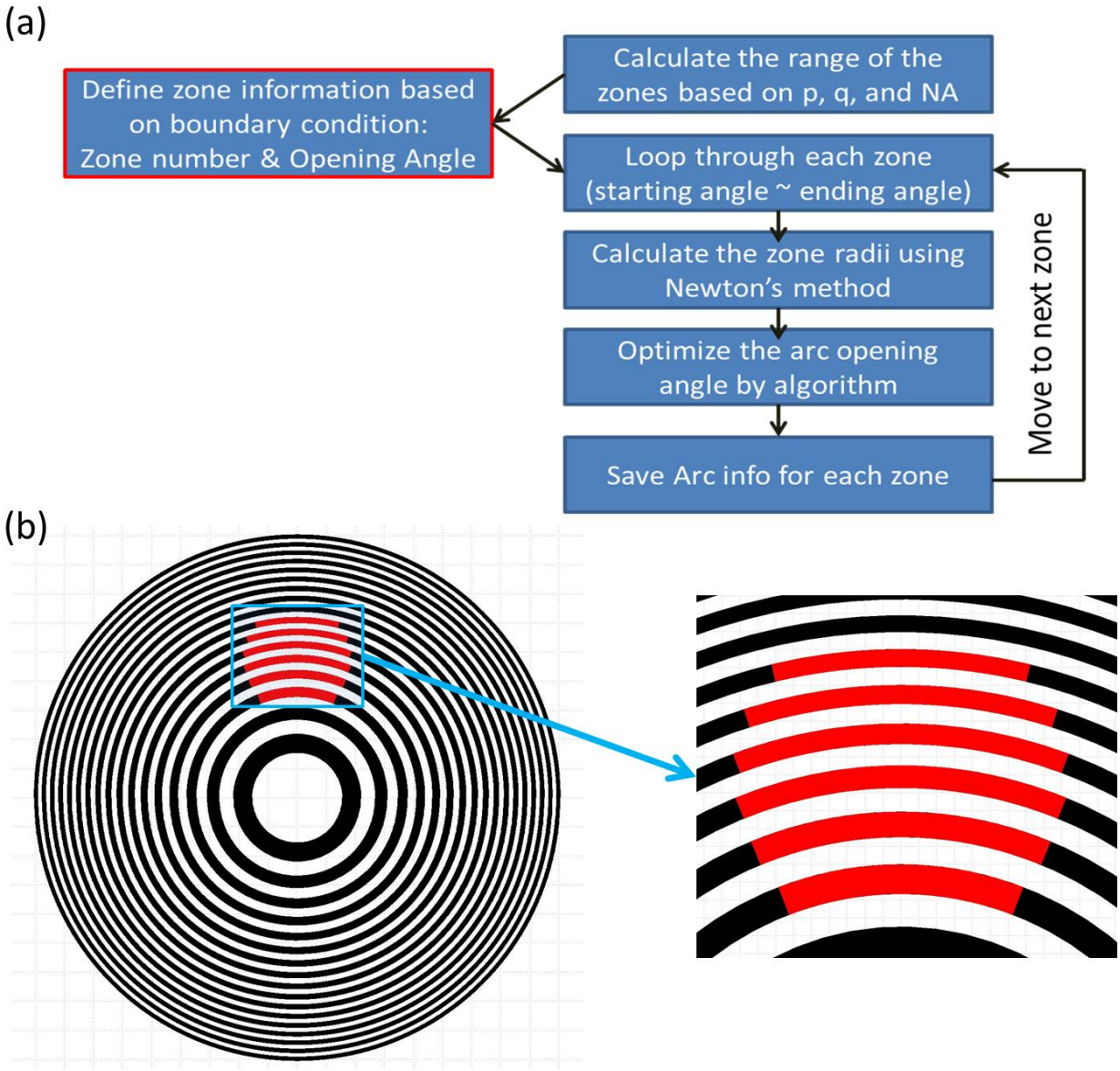

Figure 5.4: (a) The process flow to generate off-axis zoneplate pattern. (b) GDSII file pattern images of an off-axis zoneplate (red) on top of its parent on-axis zoneplate (black). The zoom-in view is shown on the right-hand side..

$$\text{OPD} = (\sqrt{p^2 + r^2} - p) + (\sqrt{q^2 + r^2} - q) \tag{5.7}$$

Here p, q, r represent the object distance, the image distance and the zone radius before tilt. For tilted zoneplates, these parameters have to be adjusted accordingly. Figure 5.5a shows a schematic diagram of a tilted zoneplate and the adjustment required to Eq. 5.7. A titled zoneplate will be stretched on each side of the zoneplate, as shown in Fig. 5.5b. In order to incorporate the tilted zoneplate situation into the pattern generation code, our algorithm adjusts the OPD definition which is shown in Fig. 5.5a in the same process flow as for conventional on-axis zoneplate.

5.3.5 Phase contrast / aberration zoneplate

In general, the zone position is determined by the OPD including the geometric terms, aberration and phase contrast, as shown in Eq. 5.8:

$$\text{OPD} = \text{Geometric} + \text{Aberration} + \text{Phase Contrast} \tag{5.8}$$

For a Fresnel zoneplate, in order to utilize the Zernike phase contrast method with a $\frac{\pi}{2}$ phase shift in the pupil plane, one can simply adjust the zone locations to the desired relative phase shift. As shown in Eq. 5.1, the OPD for a standard zoneplate is in the range of half a wavelength which can be transferred to a π phase shift. For a phase contrast zoneplate with a $\frac{\pi}{2}$ phase shift, our algorithm has to include quarter wavelength into the OPD calculation to account for the phase difference. As shown in Fig. 5.6a, the shift of the zones from their original positions creates the relative phase shift between these 2 areas.

A similar approach can be applied to aberrations. Each point on the zoneplate has its own relative phase shift based on the input aberration condition. Thus the algorithm adjusts the OPD calculation accordingly to satisfy the condition at each location. For the pattern generation algorithm, the input aberration/phase shift map consists of a Zernike polynomial representation [59]. Thus it can be used to prescribe not only a single aberration term onto the Fresnel zoneplate, but also a more realistic situation which consists of multiple aberrations. As a simple example, Figure 5.6b shows the result of adding a defocus aberration with a weight of half a wavelength to an on-axis Fresnel zoneplate.

5.3.6 Apodization zoneplate

Apodization is used to filter or modify the transmission function of the optical elements [60, 61]. In order to achieve this in the algorithm, blocks can be added to the ring-shaped zoneplate to prevent light from passing through the zoneplate, instead of varying the zone width which might be limited by the fabrication capability. Based on the designed transmission condition in each zone, the percentage of the zone area that needs to be blocked is calculated. For the situation with n blocks in one zone, the blocks are uniformly distributed by an $\frac{2\pi}{n}$ separation, and the initial angle in the zone is chosen randomly, as shown in Fig.

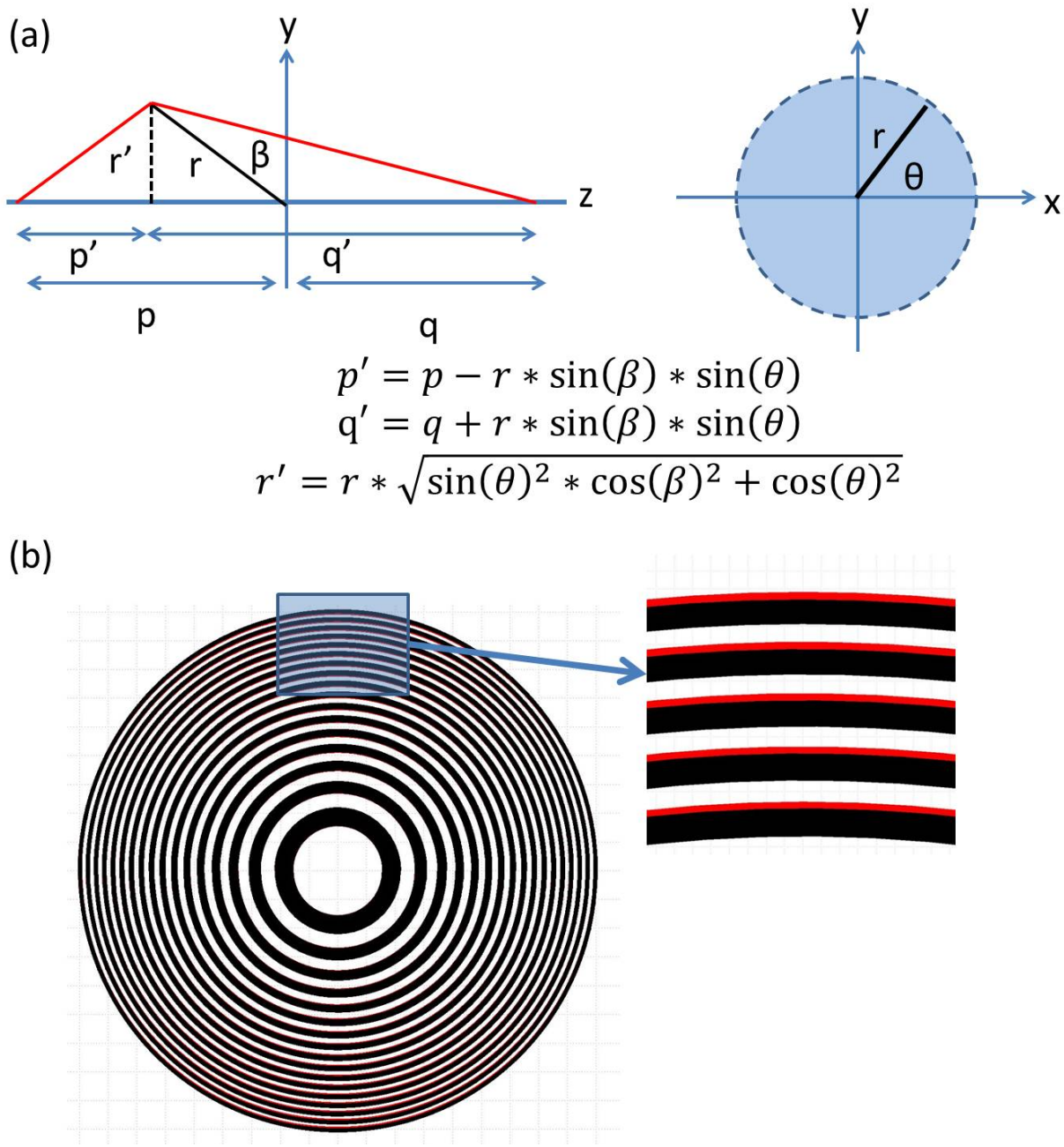

$$p' = p - r * \sin(\beta) * \sin(\theta)$$
$$q' = q + r * \sin(\beta) * \sin(\theta)$$
$$r' = r * \sqrt{\sin(\theta)^2 * \cos(\beta)^2 + \cos(\theta)^2}$$

Figure 5.5: (a) Schematic diagram of the definition of p', q', and r' based on the original p, q, and r, and also the tilt angle (β) and its relative angle (θ) towards x-axis. (b) GDSII file pattern images of a tilted on-axis zoneplate (red) on top of its parent standard zoneplate (black). The zoom-in view is shown on the right-hand side to show the shift of the zone when you tilt the zoneplate.

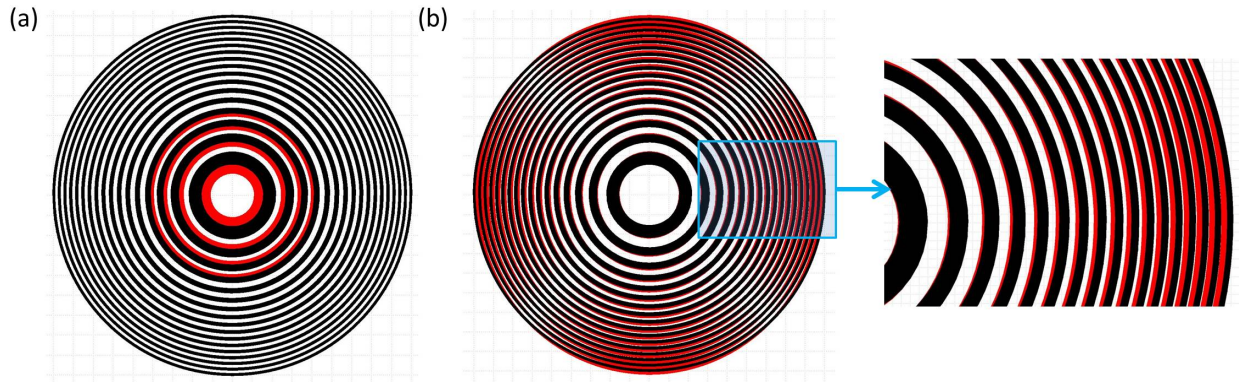

Figure 5.6: (a) GDSII file pattern images of a phase contrast zoneplate with a 90° (quarter wavelength) phase shift in the central area of an on-axis zoneplate (red) on top of a standard zoneplate (black). (b) GDSII file pattern images of an on-axis zoneplate with defocus aberration (red) on top of a standard zoneplate (black). Weight: 0.5 wavelength. The zoom-in view is shown on the right-hand side to show the shift of the zone when you prescribe the aberration onto the zoneplate.

5.7a. Stronger apodization means lower transmission which leads to more blocks in each zone. For a constant apodization to be applied to a specific area of the zoneplate, blocks are randomly and evenly distributed in each zone. Figure 5.7a shows the comparison between a standard zoneplate and a zoneplate with constant apodization.

For a more complicated situation like applying a Gaussian window to the zoneplate, the same approach used in aberration control can be applied here as well. In the algorithm, the intensity transmission can be adjusted by adding blocks at every point in the zoneplate according to the target apodization function. Figure 5.7b shows an example of off-axis zoneplate with Gaussian window.

5.3.7 Free-standing zoneplate

To improve zoneplate efficiency, the zoneplates can be fabricated as free-standing structures instead of onto a membrane. In order to have enough physical strength to support the arc-shaped zoneplate structure, bridges are required, as shown in Fig. 5.8 to hold the structure together. In the algorithm, the addition of these bridges is similar to the apodization process. Moreover, the algorithm randomly distributes the bridges, preventing unexpected frequency filtering by the Fresnel zoneplate.

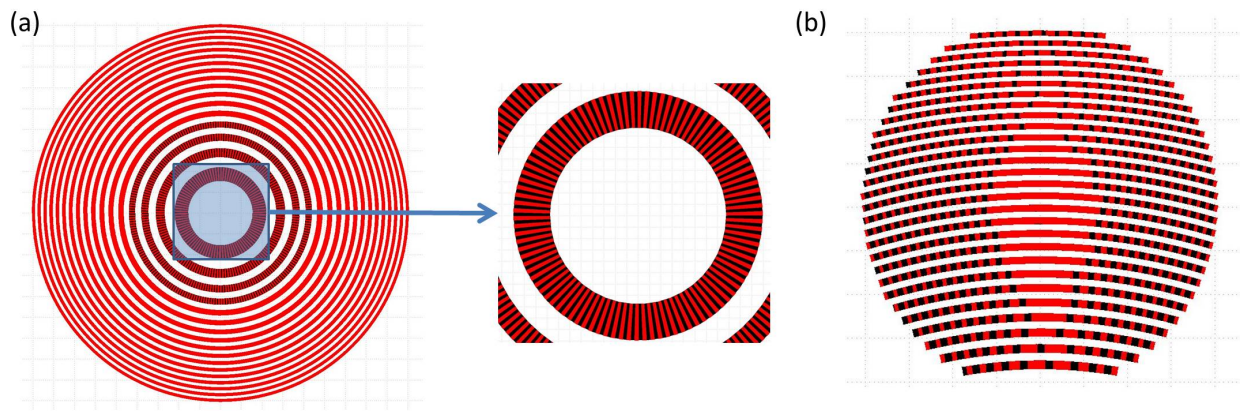

Figure 5.7: (a) GDSII file pattern images of an on-axis zoneplate with constant apodization aberration (red) in the central region on top of a standard zoneplate (black). The zoom-in view is shown at the right-hand side of the figure. (b) GDSII file pattern images of an off-axis zoneplate with a Gaussian window (red) on top of a standard off-axis zoneplate (black).

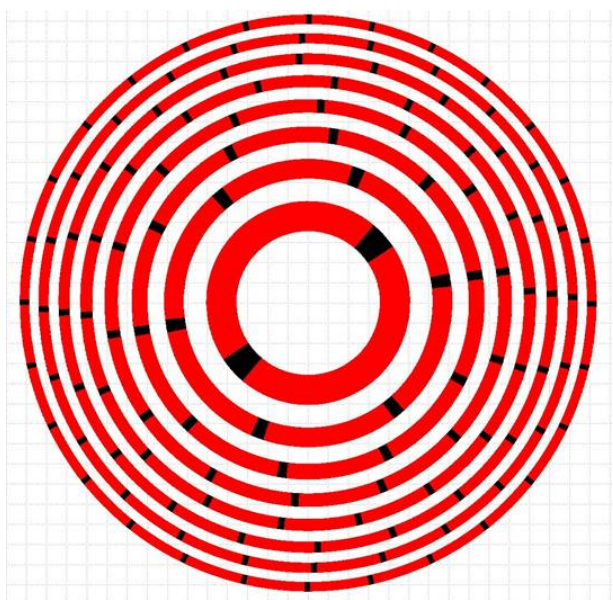

Figure 5.8: GDSII file pattern images of a free-standing zoneplate (red) on top of a standard on-axis zoneplate (black). The random distribution of the bridges of the free-standing zoneplate can avoid unnecessary frequency filtering.

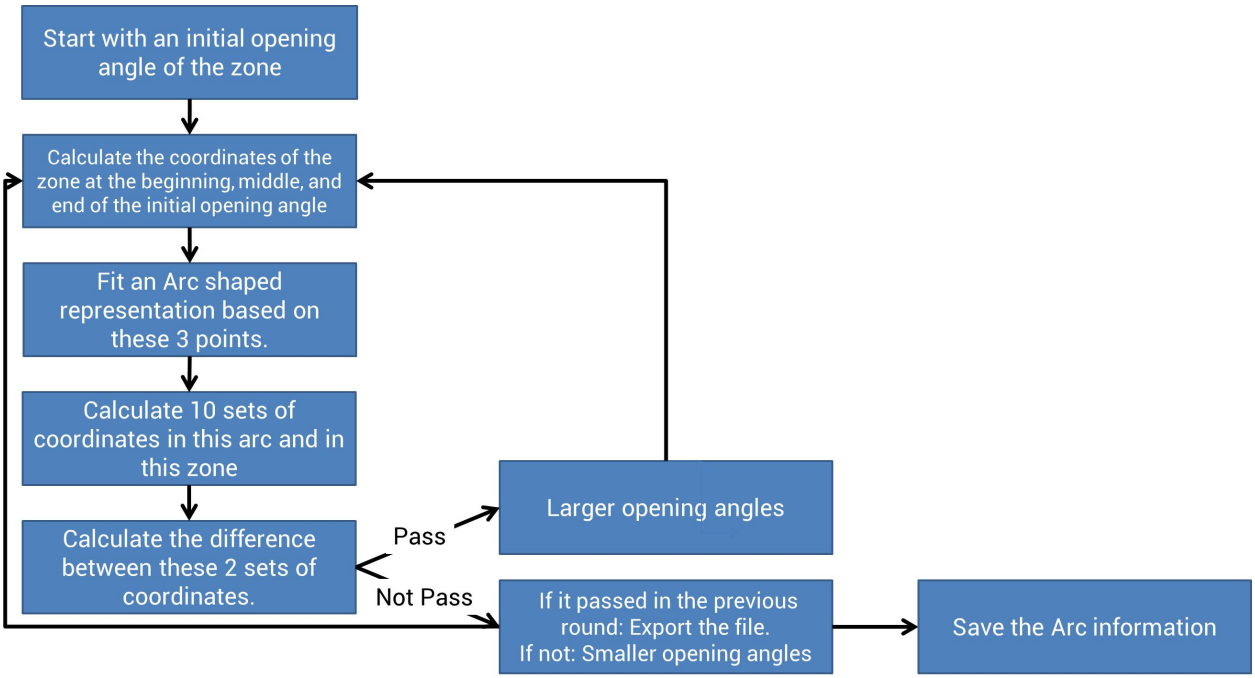

Figure 5.9: The process flow of the algorithm on how to decide the arc representation of the zoneplate pattern.

5.4 Fresnel zone plate pattern rendering and bias control algorithm

5.4.1 Arc-shaped representation of the zoneplate pattern

Once one obtained the desired Fresnel zoneplate pattern, the design must be transferred into a file that can be read by lithography tools to fabricate the zoneplate. In order to achieve this, a proper representation of the zoneplate design is needed using arcs or polygons. Therefore, an algorithm to fracture the zoneplate pattern is needed to balance the trade-off between file size (computation time) and precision of the polygons/arcs representation.

Figure 5.9 shows the process flow of rendering the zoneplate pattern with arcs. An initial opening angle for the pattern is used as the initial condition. Then 3 sets of coordinates are calculated from this zone pattern to define the arc. Along the contour of the zone pattern and the arc, a coordinate difference is calculated and checked against the user-defined tolerance. If it is within the range, the algorithm extends the opening angle to use this arc to represent a larger zoneplate pattern. If not, then a smaller opening angle is used until the condition is met. This helps us minimize the number of arcs to represent the zoneplate pattern. With this algorithm, conventional zoneplate with a perfect circular shape can be represented by 1

arc (opening angle = 360°) as expected. Other zoneplates with exotic design will each have theirs optimal number of arcs.

5.4.2 Trapezoid representation of the zoneplate

Even though the arc representation is natural for a curved Fresnel zoneplate pattern, trapezoid representation is needed since it is commonly required by most lithography tools. Figure 5.10 shows the process flow on how to transfer the zoneplate pattern representation using arcs to trapezoids.

The most critical factor for this process is the determination of how many trapezoids are needed to represent the arc properly. As shown on the right-hand side of Fig. 5.10, the difference between the edge of the arc and the trapezoid can be used as the metric, normalized to the arc (zone) width. This tolerance definition keeps the error at every zone about the same in units of wavelength. The constant phase shift between zones can reduce the potential to introduce unexpected aberration into the Fresnel zoneplate. Moreover, this variable allows the user to determine the trade-off between file size (number of trapezoids) and the error tolerance on their zoneplate pattern design.

Figure 5.11 shows the impact of selected precision on file size for three different zoneplate sizes (number of zones). For a zoneplate with 1000 zones in it, the file size is within the range of 302 Mb to 3 Mb for a precision from 0.005% to 50%. For a zoneplate with 3000 zones in it, the file size range increases to 1558 Mb to 15 Mb for a precision from 0.005% to 50%. Generally, the file size increases linearly with the zone number, and it is inversely proportional to the precision.

5.4.3 Pattern and dose bias of the zoneplate

To fabricate the zoneplate pattern with desired dimensions, pattern bias and local dose control can be very useful to account for all the non-idealities in the fabrication process. In the algorithm, the capability to control the exact dose and bias at each zone width enables the precise fabrication of the desired pattern, by compensating for photoresist and other lithography effects. The default setting in the algorithm for pattern bias is a constant bias for all arcs or polygons, and the default dose compensation in the algorithm is linearly adjusting the dose as a function of feature width and pattern bias.

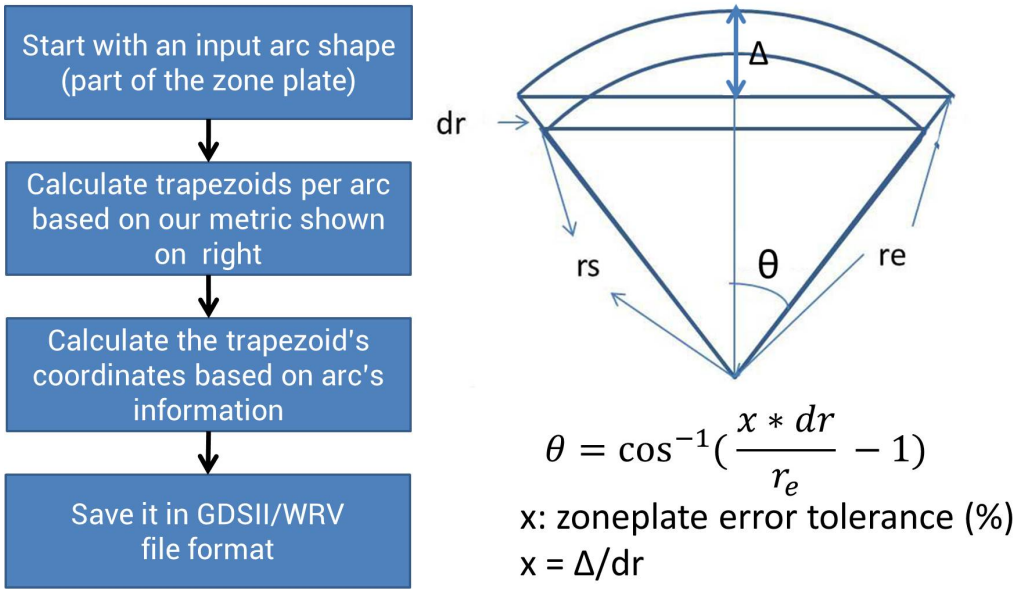

Figure 5.10: The process flow of the algorithm on how to fracture the arc into trapezoids for zoneplate pattern. The plot on the right shows the metric used to determine the size of the trapezoid based on user-defined tolerance.

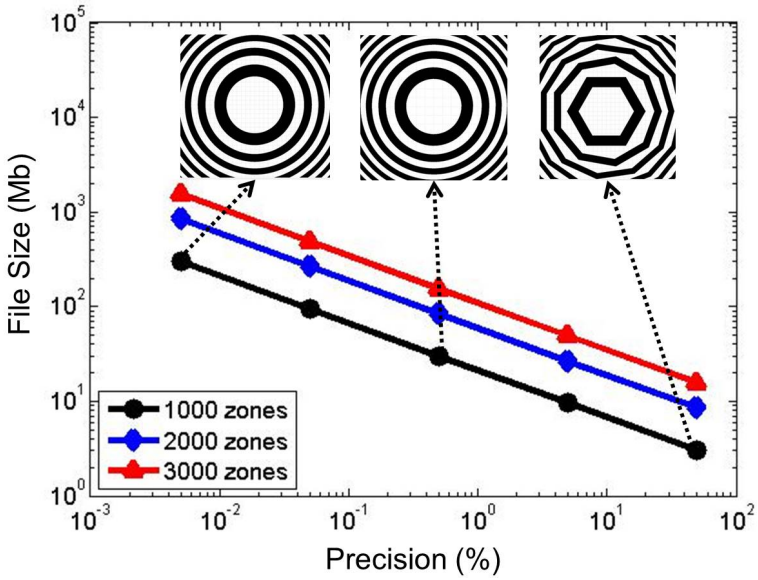

Figure 5.11: The trade-off between GDSII file size and zoneplate pattern precision under different number of zoneplates: 1000 zones (Black), 2000 zones (Blue), 3000 zones (Red). The figure is in log-log scale. The insert figures show the center of the zoneplate pattern under different precision settings.

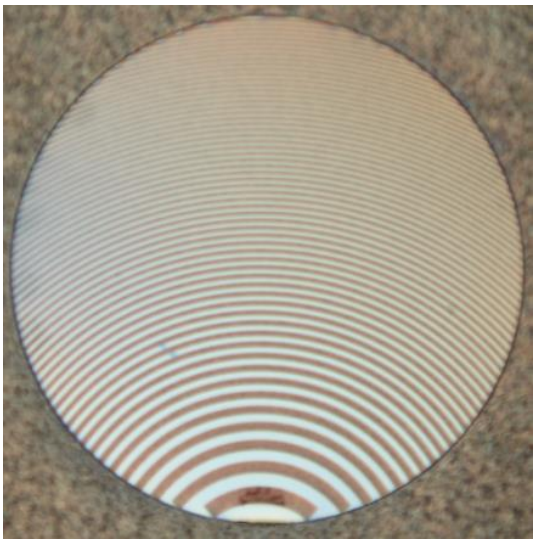

Figure 5.12: SEM image of a standard off-axis zoneplate used by the SHARP EUV microscope. The diameter of the zoneplate is around 100 um.

5.5 Fresnel zone plate pattern fabrication demonstration

5.5.1 Off-axis, tilted Fresnel zoneplate for the SHARP EUV microscope and EUV scanning microscope

Figure 5.12 shows an example of a standard zoneplate used by the SHARP EUV microscope. To avoid imaging unwanted orders scattered from the mask onto the CCD camera, the SHARP EUV microscope uses an off-axis zoneplate as its imaging optics. By using the algorithm described in the previous sections, an off-axis zoneplate pattern can be generated based on specific boundary condition for the SHARP EUV microscope. Imaging performance of the microscope using the conventional zoneplate is described in Ref. [30]. Comparing the measured contrast transfer function results presented in Ref. [30] to predict simulation results for an ideal diffraction limited system (Fig. 5.13), the patterned zoneplate is operating at the diffraction limit.

Moreover, our algorithm also supports the tilted zoneplate to deal with the nature of EUV lithography with 6° tilted illumination. With the optimization and rendering algorithm, the Fresnel zoneplate pattern ($\approx$ 100 um diameter) with various optical designs (NA, magnification, tilt, etc) can be generated easily in a few minutes, and reasonable file size for the subsequent lithography process to realize these zoneplate patterns, as shown in Fig. 5.14 [62].

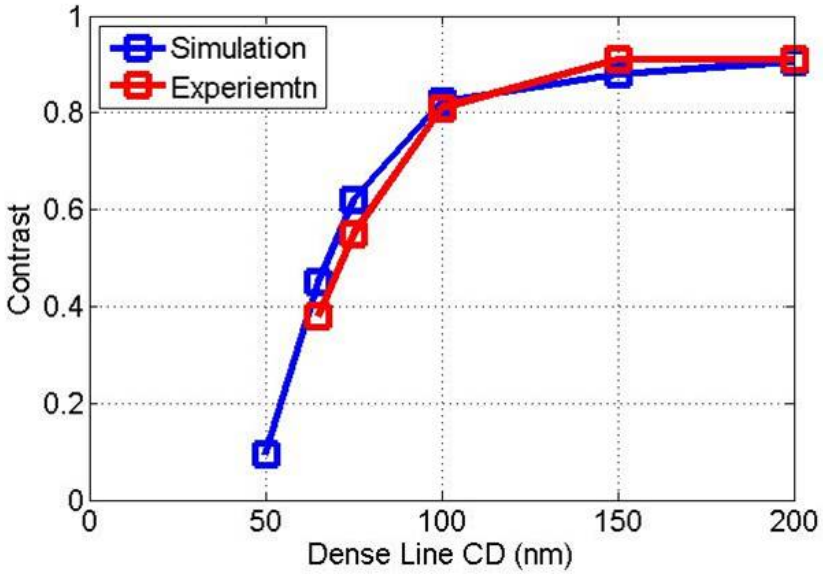

Figure 5.13: Contrast vs. CD for dense lines. Simulation results (Blue), and Experiment data (Red) from Ref. [30]. 4xNA = 0.33, partial-coherence = 0.8. 3.75% of flare is added into the simulation images.

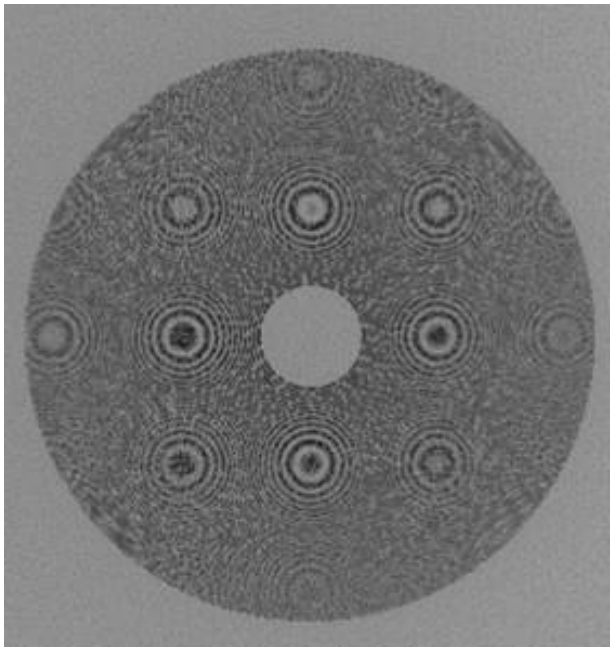

Figure 5.14: SEM image of a tilted zoneplate used by the scanning EUV microscope described in [62].

5.5.2 Off-axis, phase contrast and apodization Fresnel zoneplate for the SHARP EUV microscope

To explore the possibility of increasing multilayer defect sensitivity for EUV mask blank inspection, the Zernike phase contrast method was studied by simulation and showed promising results [44]. In order to demonstrate the idea, the SHARP EUV microscope is used to study the impact of pupil phase contrast on programmed multilayer defect sensitivity. To introduce a 90° phase shift to the unscattered light on Fresnel zoneplate, the zone has to be moved by a quarter wavelength from its original location.

By utilizing our algorithm, specific phase shifts can be introduced onto a designated area of the zoneplate. Figure 5.15(a) shows the scanning electron microscope (SEM) image of an off-axis, phase contrast zoneplate. The central circle area has been phase shifted. A zoomed-in view in Fig. 5.15(b) shows the displacement between the patterns to introduce the constant phase shifts. In addition to the phase modulation, the intensity transmission of the zoneplate can be controlled as well. Instead of changing the zone width, which might introduce unwanted aberration and increase the difficulty of the fabrication process, part of each zone in the zoneplate is blocked to control the transmission efficiency. As shown in Fig. 5.15(b), blocks can be added to the desired area on the zoneplate by our algorithm to control the amount of light passing through each zone. The phase shifts and the intensity transmission are indicated by the number shown in the figure for each zoneplate. With these zoneplates, the idea has been demonstrated and similar results were also observed in the simulation [46].

5.6 Conclusion

In this chapter, a new algorithm to generate fabrication-ready zoneplate patterns was presented. The algorithm can generate both on and off-axis zoneplate patterns, as well as arbitrary phase/intensity modulation on the Fresnel zoneplate. Moreover, a user-defined tolerance setting in the rendering algorithm keeps the flexibility between the computation time and the precision of the zoneplate pattern. The algorithm also supports features like pattern bias and dosage control to help optimize fabrication yield. The algorithm were used to generate Fresnel zoneplates used by the SHARP EUV microscope for standard imaging and other exotic imaging modes as well as tilted zoneplates for use in a scanning EUV microscopy tool [62].

(a)

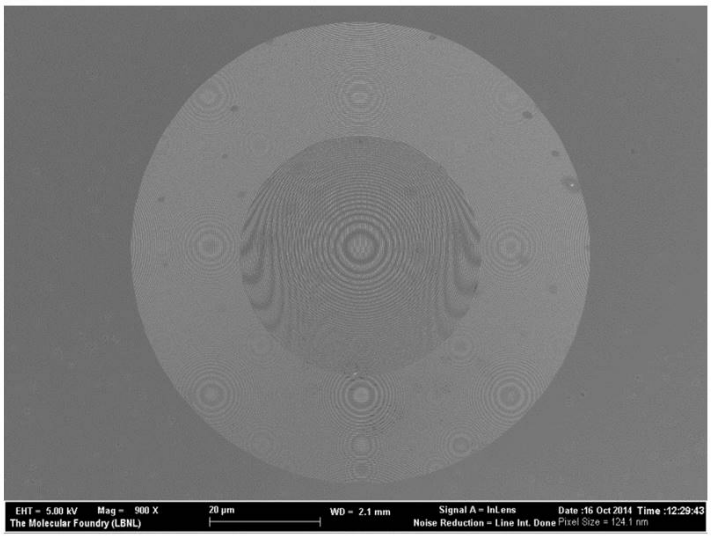

(b)

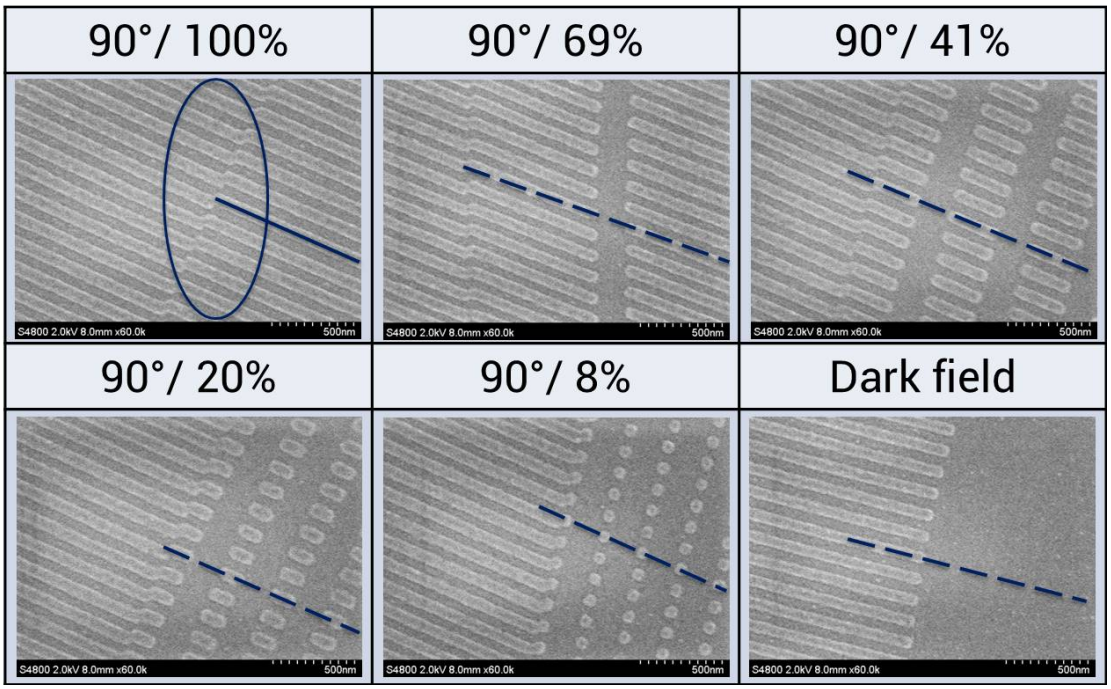

Figure 5.15: (a) SEM image of an off-axis zoneplate with phase contrast and apodization in the central area. (b) The table shows zoom-in SEM images of the SHARP zoneplates with different apodization conditions to control the transmission as indicated in the table. Circle area shows the quarter wavelength displacement which creates the 90° phase shifts and the line indicated the variation on zones intensity transmission by adding blocks.

Chapter 6

Conclusion

As a next generation lithography technology, with a much shorter wavelength (13.5 nm vs. 193 nm) and a different optical system (mirror vs. lens), it is important for EUV lithography to ensure the mask quality and understand the imaging process due to mask 3D effects. Therefore, in this dissertation, a few critical issues regarding EUV mask technology have been addressed: EUV mask blank and patterned mask inspection, and also the impact of EUV SRAF on mitigating mask 3D effects.

For EUV actinic mask blank inspection, a systematic study on the optimum optical configuration was conducted in this dissertation. First, the results showed that the Zernike phase contrast method has advantages over the bright field method on multilayer defect detection sensitivity through simulation and experiment. The simulation study showed that in-focus inspection capability and an 18% enhancement on the SNR_{max} can be achieved by the Zernike phase contrast method, while the conventional bright field method needs through-focus scanning and results in lower defect detection sensitivity. Experimental results from the SHARP EUV microscope showed that a programmed defect as small as 0.35 nm in height was detected at best focus with SNR ≈ 8 by the Zernike phase contrast method. Experimental results also showed that multilayer defects are not simply pure phase defects, but have mixed behavior (phase + absorber) depending on their size. After comparing the strengths and weaknesses of the conventional bright field and the Zernike phase contrast methods, a comparison between the Zernike phase contrast method and the dark field method was presented. After taking various noise sources and system design parameters into consideration, the simulation results showed that the Zernike phase contrast method has higher detection sensitivity under review mode (small pixel size) and lower photon density, while the dark field method is more efficient for inspection mode (large pixel size). For the dark field based actinic blank inspection tool design study, the simulation results showed that 10-watt EUV source power and 100 nm pixel size are needed to capture a phase defect of height 0.5 nm for the future advanced node. Future work in this area should consider the impact that a broader and more complex range of defects including typical native defects might have on the determination of an optimal detection configuration.

For EUV actinic patterned mask inspection, the nature of the pattern defect was dis-

cussed, and it was shown that the defect cannot be treated as a pure absorber defect due to the phase-shifting nature of the absorber material. The mixed defect (phase + absorber) behavior results in the asymmetric through-focus behavior on defect signal strength, which can impact the inspection tool design. The possibility of improving the defect signal strength by utilizing the phase component of the defect was discussed. A phase shift $\approx -50°$ instead of $\pm 90°$ is needed in the pupil plane in order to improve pattern defect signal strength. A complete tool design study for a bright field based EUV actinic pattern inspection tool was conducted. With consideration of the phase effects in pattern defects, the various noise sources, and the optical design of the system, the role of each noise source and the impact of tool parameters on inspection efficiency were discussed. The study showed that a 50% improvement on defect SNR was achieved by introducing a -50 nm defocus into the inspection system. In the future, a pattern with a realistic optical proximity correction (OPC) design or sub- resolution assist feature (SRAF) should be included in the modeling to further refine the study.

This dissertation also discussed the impact of EUV SRAFs on the Bossung curve and process window enhancement. By rigorous 3D modeling, the analysis of aerial images and scattered order distributions showed that unlike other proposed solutions which are focused on reducing aberrations in the imaging process, the introduction of the EUV SRAF actually increases the aberrations in the pupil plane, but the impact of aberration is canceled out by the complementary illumination setting. Therefore, a balanced Bossung curve and a process window improvement of 21% is achieved by EUV SRAFs. The study also showed that each SRAF has a different role on the overall imaging performance due to the shadowing effect. The results indicate that different restrictions on SRAF position are necessary for the mask-making process. To further extend the study, the impact of EUV SRAFs on 2D patterns should be considered, given that 2D patterning capability is a primary driver for the adoption of EUV lithography. Moreover, the impact of EUV photoresist line edge roughness (LER) on SRAF design and imaging performance should also be included in the analysis.

Bibliography

[1] Rudy Peeters. "EUVL Lithography Industrialization Progress". In: *Proceedings of International Symposium on Extreme Ultraviolet Lithography* (2014).

[2] Igor Fomenkov. "EUV Exposure Tools for HVM: Status and Outlook". In: *Proceedings of International Workshop on EUV Lithography* (2016).

[3] Christophe Smeets. "EUV Lithography Indutrializatoin Progress". In: *Proceedings of International Symposium on Extreme Ultraviolet Lithography* (2016).

[4] Britt Turkot. "EUV Readiness for High Volume Manufacturing". In: *Proceedings of International Symposium on Extreme Ultraviolet Lithography* (2016).

[5] Mark Neisser and Stefan Wurm. "Overview of Next Generation Lithography, Advanced Patterning, EUV and Self Assembly". In: *Proceedings of Internationl Conference on Frontiers of Characterization and Metrology* (2013).

[6] Andrew Grenville et al. "Integrated Fab Process for Metal Oxide EUV Photoresist". In: *Proceedings of SPIE* 9425.94250S (2015).

[7] Takeshi Yamane et al. "Advances in the Detection Capability on Actinic Blank Inspectoin". In: *Proceedings of SPIE* 9776.97761G (2016).

[8] Markus Weiss et al. "Actinic Review of EUV Masks: Status and Recent Results of the AIMS EUV System". In: *Proceedings of SPIE* 9422.942219 (2015).

[9] Ted Liang et al. "EUV Mask Infrastructure Readiness and Gaps for TD and HVM". In: *Proceedings of SPIE* 9635.963509 (2015).

[10] Jo Finders, Laurens de Winter, and Thorsten Last. "Mitigation of Mask Three-dimensional Induced Phase Effects by Absorber Optimization in ArFi and Extreme ultraviolet Lithography". In: *Journal of Micro/Nanolithography, MEMS, and MOEMS* 5.2 (2016), p. 021408.

[11] Thorsten Last et al. "Experimental Verification of AI Decomposition-based Source Optimization for M1 Two-bar Building Blocks in 0.33NA EUVL". In: *Proceedings of SPIE* 9985.99850W (2016).

[12] Stephen Hsu et al. "EUV Resolution Enhancement Techniques (RETs) for k1 and Below". In: *Proceedings of SPIE* 9422.94221I (2015).

[13] Laurens de Winter et al. "Understanding the Litho-impact of Phase due to 3D Mask-effects When Using Off-axis Illumination". In: *Proceedings of SPIE* 9661.99850W (2015).

[14] Nai-Ching Chen et al. "Mask Defect Management in Extreme-ultraviolet Lithography". In: *Journal of Micro/Nanolithography, MEMS, and MOEMS* 13.2 (2014), p. 023010.

[15] Sungmin Huh et al. "A Study of Defects on EUV Masks Using Blank Inspection, Patterned Mask Inspection, and Wafer Inspection". In: *Proceedings of SPIE* 7636.76360K (2010).

[16] Han-Ku Cho and Jinho Ahn. *EUV Lithography*. Ed. by Vivek Bakshi. 2008. Chap. 7, p. 333.

[17] Sasa Bajt et al. "Improved Reflectance and Stability of Mo-Si Multilayers". In: *Optical Engineering* 41.8 (2002), p. 1797.

[18] Yohei Ikebe, Tsutomu Shoki, and Takahiro Onoue. "Development of Thin Absorber for EUV Blanks". In: *Proceedings of International Symposium on Extreme Ultraviolet Lithography* (2016).

[19] Takahiro Onoue et al. "Recent Progress of EUV Blanks Development". In: *Proceedings of International Symposium on Extreme Ultraviolet Lithography* (2016).

[20] Kiwamu Takehisa et al. "Defect Review of Capability Enhancement for Actinic Blank Inspection Tool". In: *Proceedings of International Symposium on Extreme Ultraviolet Lithography* (2016).

[21] Frits Zernike. "How I Discover Phase Contrast". In: *Science* 121.3141 (1955), p. 345.

[22] E. Gullikson et al. "Practical Approach for Modeling Extreme Ultraviolet Lithography Mask Defects". In: *Journal of Vacuum Science and Technology B* 20.1 (2002), p. 81.

[23] Brittany McClinton. "Mask Roughness Induced LER in EUV Lithography". PhD thesis. University of California, Berkeley, 2011.

[24] Pei-Yang Yan et. al. "Understanding EUV mask blank surface roughness induced LWR and associated roughness requirement". In: *Proceedings of SPIE* 9422.94220J (2015).

[25] Patrick Naulleau et. al. "Extreme ultraviolet mask roughness: requirements, characterization, and modeling". In: *Proceedings of SPIE* 9256.92560J (2014).

[26] Tsuneo Terasawa et al. "Development of Actinic Full Field EUV Mask Blank Inspection Tool at MIRAI-Selete". In: *Proceedings of SPIE* 7271.727122 (2009).

[27] Rene Claus et al. "Quantitative Phase Retrieval with Arbitrary Pupil and Illumination". In: *Optics Express* 23.26672 (2015).

[28] Rene Claus et al. "Phase Measurements of EUV Mask Defects". In: *Proceedings of SPIE* 9422.942242 (2015).

[29] Ted Liang et al. "Growth and Printability of Multilayer Phase Defects on Extreme Ultraviolet Mask Blanks". In: *Journal of Vacuum Science and Technology B* 25 (2007), p. 2098.

[30] Kenneth Goldberg et al. "New Ways of Looking at Masks with the SHARP EUV Microscope". In: *Proceedings of SPIE* 9422.94221A (2015).

[31] Kenneth Goldberg et al. "Commissioning an EUV Mask Microscope for Lithography Generations Reaching 8 nm". In: *Proceedings of SPIE* 8679.867919 (2013).

[32] Yow-Gwo Wang, Andrew Neureuther, and Patrick Naulleau. "Impact of noise sources and optical design on defect detection sensitivity in extreme ultraviolet actinic pattern inspection tool". In: *Journal of Micro/Nanolithography, MEMS, and MOEMS* 16.1 (2017), p. 013504.

[33] Guido Schriever et al. "Laser-produced Plasma versus Laser-assisted Discharge Plasma: Physics and Technology of Extreme Ultraviolet Lithography Light Sources". In: *Journal of Micro/Nanolithography, MEMS, and MOEMS* 11.2 (2012), p. 021104.

[34] Advanced Accelerator Technologies. *Compact Synchrotron*. 2017. URL: `http://www.aa-t.ch.`.

[35] E. Syresin et al. "Proposal for an Accelerator Complex for Extreme Ultraviolet Nanolithography using KW-scale FEL Light source". In: *Proceedings of RuPac* (2010).

[36] Vicky Philipsen et al. "Mitigating EUV Mask 3D Effects by Alternative Metal Absorber". In: *Proceedings of International Symposium on Extreme Ultraviolet Lithography* (2016).

[37] Takashi Kamo et al. "Evaluation of Etched Multilayer Mask for 0.33NA EUVL Extension". In: *Proceedings of International Symposium on Extreme Ultraviolet Lithography* (2016).

[38] Vu Luong et al. "Optimized EUV Mask Absorber Stack for Improved Imaging by Reducing Crystallinity of Alternative Absorber Materials". In: *Proceedings of International Symposium on Extreme Ultraviolet Lithography* (2016).

[39] Obert Wood et al. "Alternative Materials for High Numerical Aperture Extreme Ultraviolet Lithography Mask Stacks". In: *Proceedings of SPIE* 9422.94220I (2015).

[40] Lior Shoval et al. "Applicability of E-bam Mask Inspection to EUV Mask Production". In: *Proceedings of SPIE* 8322.832227 (2012).

[41] Martin Burkhardt and Ananthan Raghunathan. "Best Focus Shift Mechanism for Thick Masks". In: *Proceedings of SPIE* 9422.94220X (2015).

[42] HyperLith is a registered trademark of Panoramic Technologies. In: *www.panoramictech.com* (2017).

[43] Thorsten Last, Laurens de Winter, and Jo Finders. "Imaging Enhancement by Reduction of Mask Topography Induced Phase Aberrations for Horizontal 1D Spaces under D90Y Illumination". In: *Proceedings of SPIE* 9635.96350K (2015).

[44] Yow-Gwo Wang et al. "Zernike Phase Contrast Microscope for EUV Mask Inspection". In: *Proceedings of SPIE* 9048.904810 (2014).

[45] Yow-Gwo Wang et al. "Phase-enhanced Defect Sensitivity for EUV Mask Inspection". In: *Proceedings of SPIE* 9235.92350L (2014).

[46] Yow-Gwo Wang et al. "Enhancing Defect Detection with Zernike Phase Contrast in EUV Multilayer Blank Inspection". In: *Proceedings of SPIE* 9422.94221C (2015).

[47] Yow-Gwo Wang, Andrew Neureuther, and Patrick Naulleau. "Enhancing Native Defect Sensitivity for EUV Actinic Blank Inspection: Optimized Pupil Engineering and Photon Noise Study". In: *Proceedings of SPIE* 9776.97761D (2016).

[48] Patrick Naulleau and Simi George. "Validity of the Thin Mask Approximation in Extreme Ultraviolet Mask Roughness Simulations". In: *Applied Optics* 50.19 (2011), p. 3346.

[49] Yow-Gwo Wang, Andrew Neureuther, and Patrick Naulleau. "The Study of Phase Effects in EUV Mask Pattern Defects". In: *Proceedings of SPIE* 9635.96350D (2015).

[50] Andreas Erdmann and Nishrin Kachwala. "Enhancements in Rigorous Simulation of Light Diffraction from Phase Shift Masks". In: *Proceedings of SPIE* 4691.1156 (2002).

[51] Johannes Ruoff et al. "Polarization-induced Astigmatism Caused by Topographic Masks". In: *Proceedings of SPIE* 6730.67301T (2007).

[52] Andreas Erdmann et al. "Mask-induced Best-focus-shifts in DUV and EUV Lithography". In: *Proceedings of SPIE* 9426.942605 (2015).

[53] Lieve Van Look et al. "Alternative EUV Mask Technology to Compensate for Mask 3D Effects". In: *Proceedings of SPIE* 9658.96580I (2015).

[54] Weilun Chao et al. "Soft X-ray Microscopy at a Spatial Resolution Better Than 15 nm". In: *Nature* 436 (2005), p. 1210.

[55] A. Ozawa et al. "Application of X-ray Mask Fabrication Technologies to High Resolution, Larger Diameter Ta Fresnel Zoneplates". In: *Microelectronic Engineering* 35.525 (1997).

[56] Steven Spector et al. "Process Optimization for Production of Sub-20 nm Soft X-ray Zoneplates". In: *Journal of Vacuum Science and Technology B* 15.6 (1997), p. 2872.

[57] Yan Feng et al. "Nanofabrication of High Aspect Ratio 24 nm X-ray Zoneplates for X-ray Imaging Applications". In: *Journal of Vacuum Science and Technology B* 25.6 (2007), p. 2004.

[58] Center for X-ray Optics. *Zoneplate*. 2017. URL: `http://zoneplate.lbl.gov`.

[59] Sergey Bezdidko. "The Use of Zernike Polynomials in Optics". In: *Soviet Journal of Optical Technology* 41 (1974), p. 425.

[60] Gunter Schmahl et al. "Zoneplate X-ray Microscopy". In: *Quarterly Reviews of Biophysics* 13.3 (1980), p. 297.

[61] William Southwell. "Using Apodization Functions to Reduce Sidelobes in Rugate Filters". In: *Applied Optics* 28.23 (1989), p. 5091.

[62] Patrick Naulleau et al. "Electro-optical System for Scanning Microscopy of Extreme Ultraviolet Masks with a High Harmonic Generation Source". In: *Optics Express* 22.17 (2014), p. 20144.